NUMERICAL STUDY ON THE LIGHT SCATTERING PROPERTIES OF SOME ENVIRONMENTAL COMPONENTS

A Dissertation

by

GUANGLANG XU

Submitted to the Office of Graduate and Professional Studies of
Texas A&M University
in partial fulfillment of the requirements for the degree of

DOCTOR OF PHILOSOPHY

Co-Chairs of Committee,	Ping Yang
	Sarah, D. Brooks
Committee Members,	Gerald R. North
	Richard L. Panetta
	Roland E. Allen
Head of Department,	Ping Yang

December 2017

Major Subject: Atmospheric Sciences

ABSTRACT

The light scattering properties of some components in the atmosphere and ocean are of particular interests for their relevant applications in remote sensing and climate studies. In this dissertation, numerical studies are presented on the light scattering properties of several components, including small organic and inorganic particles suspended in the water, soot-laden mineral dust aerosols, and the air-sea interface. For the aquatic particles, a non-spherical ensemble model is proposed to simulate their inherent optical properties. The comparisons between the conventional spherical and the non-spherical models on the backscattering scattering properties are discussed. For soot-laden mineral dust aerosol, soot's mixing effects on the single and multiple scattering properties of mineral dust aerosol are numerically investigated. The uncertainties on the forward and inverse modeling of radiative transfer are quantified via proposed parameterization and analysis schemes. Last, the dynamic reflection and transmission properties of an air-sea interface layer are numerically simulated via a developed Monte-Carlo radiative transfer model, the dependency on the wind speed and time are discussed.The numerical studies in this dissertation demonstrate broad applications of the light scattering simulation techniques, which have been improved dramatically over the last few decades.

DEDICATION

To my family

ACKNOWLEDGMENTS

First, I would like to express my sincere gratitude for my advisor and co-advisor Dr. Ping Yang and Dr. Sarah D. Brooks, for their continuous support and guidance on my research here at TAMU. In addition, I want to thank all of my committee members, including Dr. Gerald R. North, Dr. Richard Lee Panetta, Dr. Roland E. Allen for their helpful comments and thoughts on writing this thesis.

Then I would like to thank my friends and colleagues at this department, Chai-pang Kuo, Soichiro Hioki, Jiachen Ding, Yi Wang, Siyao Zhai, Dr. Bingqiang Sun, Dr. Guanlin Tang, Dr. Bingqi Yi, Dr. Chao Liu, Dr. Lei Bi, Dr. Jianping Liu, Dr. Patrick G. Stegmann and many others, for the kindness and help on my research and my life.

Last, but not the least, special thanks are given to my mother Anzhen Lin, my father Weiheng Xu, my brother Guangfu Xu, for their unconditional support and love.

CONTRIBUTORS AND FUNDING SOURCES

Contributors

This work was supported by a dissertation committee consisting of Professor Ping Yang (advisor), Professor Sarah D. Brooks (co-advisor) and Professor Gerald R. North, Professor Richard Lee Panetta of the Department of Atmospheric Sciences and Professor Roland E. Allen of the Department of Physics.

All work conducted for the dissertation was completed by the student independently.

Funding Sources

Graduate study was supported by National Science Foundation grants (OCE-1459180 and AGS-1338440) and partly by the endowment funds related to the David Bullock Harris Chair in Geosciences at the College of Geosciences, Texas A&M University. A major portion of the simulations was carried out at the Texas A&M University Supercomputing Facilities.

TABLE OF CONTENTS

Page

LIST OF FIGURES

FIGURE Page

LIST OF TABLES

TABLE Page

1. INTRODUCTION*

This dissertation is mainly dedicated to the numerical simulations on the single and multiple light scattering of some atmospheric and oceanic components, specifically including the aquatic particles, soot-laden mineral dust aerosols, and the air-sea interface. The light scattering properties of these environmental components could potentially serve as the prior knowledge for areas such as remote sensing applications, radiative forcing estimation, and ocean ecosystems study. In this chapter, we present the background and motivations for these studies.

1.1 Aquatic Particles

Modeling the Inherent Optical Properties (IOPs) of aquatic particles is motivated by several purposes. The underwater light field affects the productivity of marine ecosystems by regulating the rate of photosynthesis of phytoplankton. To accurately simulate the radiative transfer of light underwater, the IOPs of marine particles must be accurately known. Accurately modeling the IOPs facilitates the interpretation of remotely sensed data of the aquatic environment (e.g., ocean color), since the signals are correlated with the absorption and backscattering properties of aquatic particles [1] . Moreover, robust knowledge about aquatic particle IOPs, gained through modeling effort, also benefits the analysis of in- situ measured data, e.g. the extinction coefficient, volume scattering function (VSF), and size distribution of aquatic particles.

To calculate the IOPs of aquatic particles through various light- scattering computa-

*Part of this chapter is reprinted from (a) Journal of Quantitative Spectroscopy & Radiative Transfer, 191, 30-39, 2017, Xu, G., Sun, B., Brooks, S.D., Yang, P., Kattawar, G.W. and Zhang, X, "Modeling the inherent optical properties of aquatic particles using an irregular hexahedral ensemble", Copyright 2017, with permission from Elsevier. (b) Optics Express, 25(24), pp.A990-A1008, 2017, Xu, G., Stegmann, P.G., Brooks, S.D. and Yang, P., "Modeling the single and multiple scattering properties of soot-laden mineral dust aerosols", Copyright 2017, with permission from OSA.

tional techniques, particle shape, size, and composition must be known or assumed. The interrelations among these factors in determining various optical properties of aquatic particles remain ambiguous and challenging to resolve. As a first order approximation to randomly oriented polydisperse irregular particles, the Lorenz-Mie theory has been extensively applied to simulate hydrosol scattering properties [2, 3, 4, 5, 6, 7] . This is mainly because such calculations require very few inputs (radius, refractive index, and wavelength) and can be efficiently performed up to a very large particle size, making a homogeneous spherical model practical for various applications. However, the idealized spherical model has been called an oversimplification from both theoretical and experimental perspectives [8, 9, 10, 11] . For instance, the measured single-scattering properties of various phytoplankton species from Volten et al. [10] reveal that the internal structures (e.g., gas vacuoles) of the organisms play an important role in determining the single-scattering behavior of phytoplanktons. The measurements of Whitmire et al. [9] show that phytoplankton cells can produce a much higher backscattering signal than predicted by the Lorenz-Mie theory. This is in contrast with established suppositions that these marine organisms scatter light weakly in the backward directions. Such studies demonstrate a need to evaluate the morphological factors in the IOP modeling of aquatic particles.

Previously, inspired by the living cell nature of various organ- isms, layered spherical models had been employed in modeling the IOPs of phytoplankton [12, 13, 14, 15] , providing valuable insight on the optical impacts of internal structures. In addition, spheroids have been analyzed to quantify the biases of assuming spherical particles in modeling the IOPs of aquatic particles [16]. In this study, an ensemble of distorted hexahedra is employed to simulate the single-scattering characteristics of aquatic particles. The model was originally introduced to compute the single-scattering properties of mineral dust particles [17]. Instead of using a deterministic particle shape, a statistical approach is adopted here to define particle morphology by using an ensemble of randomly generated shapes.

These shapes are generated from the regular hexahedron with a well-defined aspect ratio, and hence the ensemble is statistically associated with a specific aspect ratio. Considering the fact that the Lorentz-Mie theory is relied on in many applications, we draw special attention to the nonspherical effect of the hexahedral ensemble model.

To explore the impact of nonsphericity on the scattering of light by particles, sophisticated computational techniques are required. Numerically accurate methods, such as the T-matrix method [18, 19, 20], the Finite-Difference Time Domain (FDTD) method [21, 22], the Discrete Dipole Approximation (DDA) [23, 24, 25, 26] , and the Pseudo Spectral Time Domain method (PSTD) [27, 28, 29], have been applied to simulate the single-scattering properties of general dielectric particles with nonspherical shapes. These methods are feasible only for relatively small particle sizes, whereas geometric optics method is applicable to large particle sizes. This study combines the Invariant Imbedding T-matrix (II-TM) method [19, 20], and the Physical-Geometric Optics Hybrid Method (PGOH) [30] to cover aquatic particle sizes from the Rayleigh to the geometric optics regime.

1.2 Soot-Laden Mineral Dust Aerosols

Mineral dust aerosols play an important role in atmospheric radiation budget due to their significant contribution to the overall atmospheric aerosol loading [31, 32, 33, 34, 35] and its global distribution via long-range convective transport [36, 37, 38]. Specifically, the global emission of mineral dust is estimated to lie anywhere between 1000 and 3000 Tg yr-1 [34]. Mineral dust aerosol particles influence the atmospheric radiative forcing both by interacting with the radiation field in the atmosphere and by providing condensation nuclei for water clouds. The the physical and chemical properties of mineral dust aerosol, essential to the evaluation of its radiative forcing effects, spatially and temporally vary [39, 40]. On a global scale, dust properties and their tempo-spatial variations can only be

estimated effectively from satellite observations.

Inferring key dust microphysical and optical properties, such as optical thickness, and particle size distributions of airborne dust from satellite observations requires a priori knowledge of the bulk single-scattering properties (such as the scattering phase function, and single-scattering albedo) of the individual mineral dust aerosol particles [18]. Subsequently these cloud properties are normally inferred by comparing the measured satellite radiance with pre-computed radiances (i.e. through best fitting) based on standard models [41] . To improve the accuracy of satellite retrievals for long-term climate study, there is a pressing need to develop realistic single-scattering properties of mineral dust aerosols.

One important factor influencing the single-scattering properties of dust is the particle nonsphericity [8, 42, 43, 44]. In addition, the internal particle composition may also lead to substantial uncertainties in modeling the single-scattering properties of mineral dust aerosols. For instance, pronounced differences in single particle scattering by various compositions of dust were reported by Glen and Brooks [45] . Other studies show that small variations in the hematite content (Fe2O3) may largely alter the absorption of mineral dust particles [46, 47] . These identified particle properties have been the primary causes of significant uncertainties in determining the single-scattering properties of pure mineral dust aerosols considered in previous studies.

As mineral dust aerosols are convectively transported across long distances [36, 37, 38], their optical properties are subject to variation because of aging and the mixing with other types of aerosol. Particularly, interactions between mineral dust and carbonaceous particles are commonly observed [42, 43, 48, 49]. Among the various carbonaceous species, black carbon (BC) deserves special attention because of its increasing number of artificial sources, its long residence time in the atmosphere, and strong absorption in the visible band [50, 51]. Mixing with black carbon may significantly alter both the scattering and absorption properties of mineral dust particles at the same time [52, 53, 54, 55]. Thus,

the impact of the degree of mixing on single-scattering property calculations needs to be further investigated.

The overarching goal of this part of study is to understand the effect of black carbon mixing on both single and multiple scattering properties of mineral dust aerosols. As a first step in this study, the single-scattering properties of soot, mineral dust, and mineral dust with soot attachments are calculated. The accuracy of the computed single-scattering properties is evaluated by comparison with both measurements and other numerical studies. Furthermore, we introduce a method to parameterize the resulting effective bulk scattering properties of the soot-laden dust aerosols. This method allows us to map a specific mixing state of aerosols to a set of effective single-scattering properties. Given the parameterized single-scattering properties, we numerically investigate the polarized reflectivity of an aerosol layer at various mixing states by solving the plane-parallel radiative transfer equation. Finally, the uncertainties caused by the mixing effect, on both forward and inverse modeling, are quantified.

1.3 Air-Sea Interface

The reflection and transmission properties of the ocean surface are fundamental to the radiative transfer simulations for air-sea coupled environmental system, serving as the boundary conditions for light propagation in the atmosphere and the ocean [56, 57, 58, 59, 60, 61, 62]. These properties are mainly determined by the roughness of the ocean surfaces, which is related to the wind speed near the surface, and the inherent optical properties of water. Cox and Munk measured the statistical relation between the wind speed and surface roughness using the sun glint pictures in 1954 [63]. If one only consider a static ocean, the Cox-Munk wave slope model provides enough accuracy and efficiency on the computation of the statistical reflection and transmission properties of the ocean surface [64, 65]. But when a dynamic ocean surface is considered, the light field

of short-duration could fluctuate dramatically near the surface [66]. Such characteristics are relevant to some of the studies including underwater imaging [67], photosynthesis of phytoplankton[68, 69], and ocean surface remote sensing [70, 71]. In addition to the temporal and directional fluctuation patterns, the ocean wave characteristics may also impacts the mean value of the reflected and transmitted irradiance. For a dynamic ocean surface, the incident photons could be deflected to various directions such that they may have longer or shorter paths before reaching to the same depth in the ocean, which leads to stronger or weaker multiple scattering effects. Consequently, the water-leaving irradiance or the down welling irradiance could be changed.

The reflection and transmission properties of air-sea interface can be studied using analytical methods with predetermined ocean slope distribution [72]. But analytical approaches overlook some characteristics such as the dynamic perspective of ocean and multiple scattering effects. In analytical methods, the ocean surfaces are simply described by the wave facet slope distribution without considering the elevations of the wave. This simplification may cause some issues such as the energy conservation issue, i.e. the energy of the incident light may not equal to the total reflected and transmitted energy[56, 63, 73] . To study the light field pattern of a more realistic air-sea interface, Monte-Carlo method has been often applied thanks to its flexibility on the complex medium geometry [74, 75, 76, 77, 78]. With Monte Carlo method, on can deal with a dynamic ocean surface with multiple scattering processes resolved. In this part of study, we particularly focus on studying the polarized light field of an the air-sea interface layer without considering the entire atmosphere-ocean system. A Monte-Carlo method is applied for tracking the photon paths as well as their weights. The ocean surfaces are modeled as deterministic facet geometry for each computation. Accordingly, when a photon encounters a scattering event, its future traveling path is sampled randomly in accordance with the scattering properties of the medium, whereas when it encounters reflections and transmissions, the

interactive facets of the air-sea interface determine the paths of the reflected or transmitted photons.

As an application of this model, we discuss the reflected and transmitted properties of the air-sea interface layer relating to the dynamic aspect of the ocean surface. The temporal fluctuations of the reflected and transmitted radiance are simulated. In addition, the total upwelling and downwelling irradiance variations in accordance with the wind-speed will be discussed.

1.4 Organization of the Dissertation

The organization of the dissertation is as followed: Chapter 2 introduces some basic concepts about the mathematical description of light and light scattering. Chapter 3 introduces some of the numerical methods applied in this study. Chapter 4 discusses the model and results for simulating the inherent optical properties of aquatic particles. Chapter 5 focuses on the numerical study on the single and multiple light scattering properties of soot-laden mineral dust. Chapter 6 introduces the models and numerical methods for modeling the transmitted and reflected beam of an air-sea interface layer, and the reflection and transmission properties of a dynamic ocean surface are discussed. Chapter 7 is the conclusions.

2. THE SINGLE AND MULTIPLE SCATTERING OF LIGHT

In this chapter, we introduce some basic concepts and equations that are necessary for this study. First, we introduce the scalar and vector description of light. Next, some basic formula on single-scattering of light are introduced. Last, important multiple scattering properties and the radiative transfer equation are described.

2.1 Description of Light

One of the fundamental quantities in radiative transfer theory is the radiance $I(\overrightarrow{r}, \widehat{\Omega}, \nu, t)$, which describes the radiation strength at point $\overrightarrow{r}$, along $\widehat{\Omega}$ direction, with frequency ν, at time t. For a particular detector with surface S with normal direction $\widehat{n}$, the radiation energy measured by the detector during time interval $(t, t + \Delta t)$, with solid angle $\Delta\Omega$ along $\widehat{\Omega}$ direction, and frequency interval $(\nu, \nu + \Delta\nu)$ can be expressed as

$$\Delta E = I(\overrightarrow{r}, \widehat{\Omega}, \nu, t) cos(\theta) S \Delta\Omega \Delta\nu \Delta t, \tag{2.1}$$

where θ is the angle between $\widehat{n}$ and $\widehat{\Omega}$.

Another important quantity called irradiance, measures the energy amount flowing through a unit surface area at $\overrightarrow{r}$ with frequency interval $(\nu, \nu + \Delta\nu)$ and time interval $(t, t + \Delta t)$ from all directions, i.e.

$$F(\overrightarrow{r}, \nu, t) = \int d\Omega I(\overrightarrow{r}, \widehat{\Omega}, \nu, t) cos(\theta) \tag{2.2}$$

Accordingly, the radiance has a unit of $WHz^{-1}m^{-2}sr^{-1}$, while the irradiance has a unit of $WHz^{-1}m^{-2}$.

Radiance and irradiance are two fundamental quantities in radiometry, while in single-scattering simulation, one must deal with the vector nature of light. To describe the vector

nature of light, we introduce the plane wave solution to Maxwell equations, .i.e.,

$$\widetilde{E}(\overrightarrow{r},t) = \overrightarrow{E}_o e^{i\overrightarrow{k}\cdot\overrightarrow{r}-i\omega t}, \tag{2.3}$$

$$\widetilde{H}(\overrightarrow{r},t) = \overrightarrow{H}_o e^{i\overrightarrow{k}\cdot\overrightarrow{r}-i\omega t}, \tag{2.4}$$

where $\widetilde{E}$ and $\widetilde{H}$ are the complex electric and magnetic fields, $\overrightarrow{r}$ is the location, and t is time, ω is the frequency, and the three constants, $\overrightarrow{k}$, $\overrightarrow{E}_o$, $\overrightarrow{H}_o$ are constrained by

$$\overrightarrow{k}\cdot\overrightarrow{E}_o = 0 \tag{2.5}$$

$$\overrightarrow{k}\cdot\overrightarrow{E}_o = 0 \tag{2.6}$$

$$\overrightarrow{k}\times\overrightarrow{E}_o = \omega\mu\overrightarrow{H}_o \tag{2.7}$$

$$\overrightarrow{k}\times\overrightarrow{H}_o = -\omega\mu\overrightarrow{E}_o \tag{2.8}$$

where μ is the magnetic permeability, ε is the electric permittivity. Due to the above relations, we can just use the electric field to describe the electromagnetic wave. In addition, since the waves are transverse (as indicated in (2.5)&(2.6)), one can decompose the electric field on a plane perpendicular to the wave vector $\overrightarrow{k}$ as

$$\widetilde{E} = \begin{pmatrix} E_\alpha \\ E_\beta \end{pmatrix} e^{i\overrightarrow{k}\cdot\overrightarrow{r}-i\omega t} \tag{2.9}$$

where E_α and E_β are two complex components of E_o along two orthogonal directions. Since E_α and E_β are still complex, they can hardly be measured directly. It is therefore more useful to give an equivalent description using four real numbers, called Stokes pa-

rameters,

$$\mathbf{I} = \begin{pmatrix} I \\ Q \\ U \\ V \end{pmatrix} = \begin{pmatrix} E_\alpha {E_\alpha}^* + E_\beta {E_\beta}^* \\ E_\alpha {E_\alpha}^* - E_\beta {E_\beta}^* \\ E_\alpha {E_\beta}^* + {E_\alpha}^* E_\beta \\ i(E_\alpha {E_\beta}^* - E_\beta {E_\alpha}^*) \end{pmatrix}. \tag{2.10}$$

If the light beam is quasi-monochromatic, these parameters should be defined as its time-averaged counterpart. The Stokes parameters definition guarantee the following relation,

$$I^2 \geq Q^2 + U^2 + V^2. \tag{2.11}$$

The degree of polarization is defined as

$$D_p = \frac{\sqrt{Q^2 + U^2 + V^2}}{I}, \tag{2.12}$$

and the degree of linear polarization is defined as

$$D_{lp} = \frac{\sqrt{Q^2 + U^2}}{I} \tag{2.13}$$

2.2 The Single-Scattering Properties

Assume that a small particle is illuminated by a plane monochromatic electromagnetic wave $\overrightarrow{E}_i$ along $\widehat{e}_z$ direction, the scattered field is generated due to the present of this obstacle. At large distances, it can be proved that the scattered electric field $\widehat{E}_s$ has the form [79],

$$\overrightarrow{E}_s \sim \frac{e^{ikr}}{-ikr} \overrightarrow{E}_{so} \tag{2.14}$$

where k is the wavenumber and r is the distance along $\widehat{e}_r$, and $\overrightarrow{E}_{so}$ satisfies

$$\widehat{e}_r \cdot \overrightarrow{E}_{so} = 0 \tag{2.15}$$

The incident and scattered directions define the scattering plane. We can decompose the amplitudes of the incident wave and scattered waves with respect to the scattering plane, and their relation can be written as

$$\begin{pmatrix} E_{\alpha s} \\ E_{\beta s} \end{pmatrix} = \frac{e^{ik(r-z)}}{-ikr} \begin{pmatrix} S_2 & S_3 \\ S_4 & S_1 \end{pmatrix} \begin{pmatrix} E_{\alpha i} \\ E_{\beta i} \end{pmatrix}, \tag{2.16}$$

where

$$S = \begin{pmatrix} S_2 & S_3 \\ S_4 & S_1 \end{pmatrix} \tag{2.17}$$

is the amplitude scattering matrix, a function of scattering direction. The scattering direction can be specified by an azimuth angle ϕ and the scattering angle θ, i.e. the angle between the incident and scattering directions.

If we apply the Stokes parameters definition to Eq.(2.16), it can be written as

$$\begin{pmatrix} I_s \\ Q_s \\ U_s \\ V_s \end{pmatrix} = \frac{1}{k^2 r^2} \begin{pmatrix} M_{11} & M_{12} & M_{13} & M_{14} \\ M_{21} & M_{22} & M_{23} & M_{24} \\ M_{31} & M32 & M_{33} & M_{34} \\ M_{41} & M_{42} & M_{43} & M_{44} \end{pmatrix} \begin{pmatrix} I_i \\ Qi \\ U_i \\ V_i \end{pmatrix} \tag{2.18}$$

where the M_{ij} are the elements of the so-called Mueller matrix. The relations between the

amplitude scattering matrix elements and the Mueller matrix elements are as followed,

$$
\begin{aligned}
M_{11} &= \frac{1}{2}(|S_2|^2 + |S_3|^2 + |S_4|^2 + |S_1|^2) && (2.19)\\
M_{12} &= \frac{1}{2}(|S_2|^2 - |S_3|^2 + |S_4|^2 - |S_1|^2) && (2.20)\\
M_{13} &= Re(S_2 S_3^* + S_1 S_4^*) && (2.21)\\
M_{14} &= Im(S_2 S_3^* - S_1 S_4^*) && (2.22)\\
M_{21} &= \frac{1}{2}(|S_2|^2 + |S_3|^2 - |S_4|^2 - |S_1|^2) && (2.23)\\
M_{22} &= \frac{1}{2}(|S_2|^2 - |S_3|^2 - |S_4|^2 + |S_1|^2) && (2.24)\\
M_{23} &= Re(S_2 S_3^* - S_1 S_4^*) && (2.25)\\
M_{24} &= Im(S_2 S_3^* + S_1 S_4^*) && (2.26)\\
M_{31} &= Re(S_2 S_4^* + S_1 S_3^*) && (2.27)\\
M_{32} &= Re(S_2 S_4^* - S_1 S_3^*) && (2.28)\\
M_{33} &= Re(S_2 S_1^* + S_3 S_4^*) && (2.29)\\
M_{34} &= Im(S_2 S_3^* + S_4 S_3^*) && (2.30)\\
M_{41} &= Im(S_4 S_2^* + S_1 S_3^*) && (2.31)\\
M_{42} &= Im(S_4 S_2^* - S_1 S_3^*) && (2.32)\\
M_{43} &= Im(S_1 S_2^* - S_3 S_4^*) && (2.33)\\
M_{44} &= Re(S_1 S_2^* - S_3 S_4^*) && (2.34)
\end{aligned}
$$

When the elements of Mueller matrix M_{ij} has an dependency on azimuth angle ϕ, the scattering cross-section can be defined as

$$
\begin{aligned}
C_{sca} = \frac{1}{k^2}\int_0^{2\pi} d\phi \int_0^{\pi} d\theta sin(\theta)[M_{11}(\theta,\phi) + M_{12}(\theta,\phi)[\frac{Q_1}{I_i}cos(2\phi) \\
-\frac{V_i}{I_i}sin(2\phi)] + M_{13}(\theta,\phi)[\frac{Q_i}{I_i}sin(2\phi) + \frac{U_i}{I_i}cos(2\phi)] + M_{14}(\theta,\phi)\frac{V_i}{I_i}],
\end{aligned}
\tag{2.35}
$$

Otherwise it can be defined as

$$C_{sca} = \frac{2\pi}{k^2} \int_0^{\pi} d\theta sin(\theta)[M_{11}(\theta) + M_{14}(\theta)\frac{V_i}{I_i}]. \tag{2.36}$$

It can be proved that the extinction cross-section is

$$C_{ext} = \frac{4\pi}{k^2} Re\left[S_1(0)\right] \tag{2.37}$$

The absorption cross-section can then be obtained due to the conservation of energy,

$$C_{abs} = C_{ext} - C_{sca} \tag{2.38}$$

Some other useful quantities include the scattering, extinction and absorption efficiencies, defined as

$$E_{sca/ext/abs} = \frac{C_{sca/ext/abs}}{G}, \tag{2.39}$$

where G is the geometric cross-section of the particle along the incident direction. And the single-scattering albedo defined as

$$\omega = \frac{C_{sca}}{C_{ext}} \tag{2.40}$$

2.3 Radiative Transfer Equation and Multiple Scattering Properties

In atmosphere and ocean system, the scattering medium is often assumed to be plane-parallel. The real environment will not be strictly plane-parallel, but on a large scale, the plane-parallel assumption could be a fair approximation. In this case, the radiative transfer equation (RTE) can be written as,

$$\mu\frac{d}{dz}I(z,\Omega) = (\alpha_p(z)+\sigma_p(z))I(z,\Omega)$$
$$-\frac{\omega_p(z)}{4\pi}(\alpha_p(z)+\sigma_p(z))\int M_p(z,\Omega,\Omega')I(z,\Omega')d\Omega' \tag{2.41}$$

where μ is $cos(\theta)$, θ is the zenith angle of the radiance propagation direction, z is the vertical coordinate for the assumed plane-parallel geometry, $\alpha_p(z))$ and $\sigma_p(z)$are the absorption and scattering coefficients respectively of the particles in the medium, $\omega_p(z)$ is the single- scattering albedo, and $M_p(z,\Omega,\Omega')$ is the scattering phase matrix. The subscript 'p' indicates that the parameter is the bulk scattering properties of the particle ensemble. Two directions Ω and Ω' form a plane called scattering plane, form an angle Θ called scattering angle. Assuming that each volume element contains an equal number of particles and mirror particles in random orientation, on a specific scattering plane, the scattering phase matrix has a block-diagonal form, given by

$$P_p = \begin{pmatrix} P_{11} & P_{12} & 0 & 0 \\ P_{12} & P_{22} & 0 & 0 \\ 0 & 0 & P_{33} & P_{34} \\ 0 & 0 & -P_{34} & P_{44} \end{pmatrix} \tag{2.42}$$

An important dimensionless quantity called optical thickness is defined as

$$\tau = (\alpha_p(z)+\sigma_p(z))D_z \tag{2.43}$$

where D_z is the depth of the medium along z direction. With τ, the RTE can be written as

$$\mu\frac{d}{d\tau}I(z,\Omega) = I(z,\Omega) - \frac{\omega_p(z)}{4\pi}\int M_p(z,\Omega,\Omega')I(z,\Omega')d\Omega' \tag{2.44}$$

For a particular layer of medium, the outgoing radiance $I(\Omega)$ measured at the top of the medium in response to the incoming irradiance $I_o(\Omega)$ can be written as,

$$I(\Omega) = \mu_0 R(\Omega, \Omega_o) I_o(\Omega_o) \tag{2.45}$$

where the quantity $R(\Omega, \Omega_o)$ is the reflectivity of the medium, and μ_0 is the cosine of the incoming irradiance zenith angle. If polarization is considered, $R(\Omega, \Omega_o)$ becomes a 4 by 4 matrix called polarized reflectivity. The reflectivity is one of the most important multiple scattering properties of the medium, and it is independent of the incoming irradiance.

3. NUMERICAL METHODS SURVEY

In this chapter, we introduce some numerical methods relevant to this study. Small particles in real environment are complex in terms of shape, size and composition. To simulate their optical properties, different numerical techniques need to be applied in accordance with the characteristics of particles as well as the desired accuracy. First, we introduce the widely used Lorenz-Mie theory, which provides an analytical solution to spheres. Next we discuss the Invariant-Imbedding T-matrix method (II-TM), which can be applied to particles with relatively small size and moderate complex geometry. Lastly, we briefly introduce the basic principle of the Physical-Geometric Optics Hybrid method (PGOH), which is useful for relatively large particles with facet morphology.

3.1 Lorenz-Mie Theory

Lorenz-Mie theory provides an analytical solution to the light scattering problem of particle with perfect spherical geometry. It has been widely used in many areas thanks to its efficiency and accuracy. [80, 81]. Below we provide a brief survey on this method.

The time-harmonic electromagnetic field $(\overrightarrow{E}, \overrightarrow{H})$ satisfy the following vector Helmholtz equation in a linear, isotropic, homogeneous medium, i.e.

$$\nabla^2 \overrightarrow{E} + k^2 \overrightarrow{E} = 0, \tag{3.1}$$

$$\nabla^2 \overrightarrow{H} + k^2 \overrightarrow{H} = 0, \tag{3.2}$$

where k is the wave number. In addition, the fields are constrained by Eq(2.5-2.8) as apllied to $(\overrightarrow{E}_o, \overrightarrow{H}_o)$.

Construct the following wave functions $\overrightarrow{M}$ and $\overrightarrow{N}$ as,

$$\overrightarrow{M} = \nabla \times (\overrightarrow{c}\psi), \tag{3.3}$$

$$\overrightarrow{N} = \frac{\nabla \times \overrightarrow{M}}{k}, \tag{3.4}$$

where $\overrightarrow{C}$ is a constant vector, and ψ is a scalar. It can be shown that $\overrightarrow{M}$and $\overrightarrow{N}$ satisfy the vector Helmholtz equation if ψ satisfy the scalar Helmholtz equation,

$$\nabla^2\psi + k^2\psi = 0. \tag{3.5}$$

To obtain $\overrightarrow{M}$ and $\overrightarrow{N}$, one can first solve the above equation for ψ. By using the separation of variables technique in spherical polar coordinates (θ, ϕ, r), we can find the basic solutions to the equation,

$$\psi_{ml} = e^{im\phi}P_l^m(cos(\theta))z_l(kr). \tag{3.6}$$

By choosing $\overrightarrow{c} = \overrightarrow{r}$, the corresponding basic vector solutions are

$$\overrightarrow{M}_{ml} = \nabla \times (\overrightarrow{r}\psi_{ml}), \tag{3.7}$$

$$\overrightarrow{N}_{ml} = \frac{\nabla \times \overrightarrow{M}_{ml}}{k}. \tag{3.8}$$

By using these basic solutions, one can construct the electric fields with coefficients to be determined.

$$\overrightarrow{E} = \sum_{l=0}^{\infty}\sum_{m=-l}^{l}(a_{ml}\overrightarrow{M}_{ml} + b_{ml}\overrightarrow{N}_{ml}), \tag{3.9}$$

while the magnetic field can always be determined from the electric field,

$$\overrightarrow{H} = \frac{c}{ik}\nabla \times \overrightarrow{E}, \tag{3.10}$$

where c is light speed.Accordingly, considering the characteristics of the fields, one can write the incident, internal, and scattering fields in the following form,

$$\overrightarrow{E}_{inc} = \sum_{l=0}^{\infty}\sum_{m=-l}^{l}(a_{ml,inc}\overrightarrow{M}_{ml}^{(1)} + b_{ml,inc}\overrightarrow{N}_{ml}^{(1)}), \tag{3.11}$$

$$\overrightarrow{E}_{int} = \sum_{l=0}^{\infty}\sum_{m=-l}^{l}(a_{ml,int}\overrightarrow{M}_{ml}^{(1)} + b_{ml,int}\overrightarrow{N}_{ml}^{(1)}), \tag{3.12}$$

$$\overrightarrow{E}_{sca} = \sum_{l=0}^{\infty}\sum_{m=-l}^{l}(a_{ml,sca}\overrightarrow{M}_{ml}^{(3)} + b_{ml,sca}\overrightarrow{N}_{ml}^{(3)}), \tag{3.13}$$

where the superscript (1) denotes the spherical Bessel function of the first kind j_l, and the superscript (3) denotes the spherical Bessel function of the third kind $h_l^{(1)}$. Assume that the incident wave is a plane wave as introduced in last chapter, then the coefficients $a_{ml,inc}$ and $b_{ml,inc}$ can be derived analytically[81]. The internal and scattered fields can be determined from the boundary conditions at the particle surface $r = r_p$, where r_p is the radius of the particle. Specifically, the components of these fields on the surface satisfy

$$E_{inc,\theta} + E_{sca,\theta} = E_{int,\theta} \tag{3.14}$$

$$E_{inc,\phi} + E_{sca,\phi} = E_{int,\phi} \tag{3.15}$$

$$H_{inc,\theta} + H_{sca,\theta} = H_{int,\theta} \tag{3.16}$$

$$H_{inc,\phi} + H_{sca,\phi} = H_{int,\phi} \tag{3.17}$$

With the field inside and outside the particle determined, the scattering amplitude matrix for each scattering direction can be then derived[81]. Due to the symmetry of the particle,

the scattering amplitude matrix has the form,

$$S(\theta) = \begin{pmatrix} S_2(\theta) & 0 \\ 0 & S_1(\theta) \end{pmatrix} \tag{3.18}$$

Consequently, the Mueller matrix has the form

$$M(\theta) = \begin{pmatrix} M_{11}(\theta) & M_{12}(\theta) & 0 & 0 \\ M_{12}(\theta) & M_{11}(\theta) & 0 & 0 \\ 0 & 0 & M_{33}(\theta) & M_{34}(\theta) \\ 0 & 0 & -M_{34}(\theta) & M_{33}(\theta) \end{pmatrix} \tag{3.19}$$

It can be seen that M only has 4 independent parameters.

3.2 Invariant-Imbedding T-matrix Method

Obtaining T-matrix based on volume-integral equation with invariant-imbedding technique was originally proposed by Johnson [82], and later it has been implemented for obtaining the scattering properties of ice and aerosol particles[19, 20]. Below we outline the framework of this method.

In last section, we've introduced the expansion of the incident and scattering fields in terms of $\overrightarrow{M}^{(1)}_{ml}$, $\overrightarrow{N}^{(1)}_{ml}$, $\overrightarrow{N}^{(3)}_{ml}$, and $\overrightarrow{N}^{(3)}_{ml}$. Since the Maxwell equations are linear, there must be a linear relation between the expansion coefficients of the incident field and those of the scattered field. This relation can be written as

$$\begin{pmatrix} a_{ml,sca} \\ b_{ml,sca} \end{pmatrix} = \sum_{l'=1}^{\infty} \sum_{m'=-l'}^{l'} \begin{pmatrix} T^{11}_{mlm'l'} & T^{12}_{mlm'l'} \\ T^{21}_{mlm'l'} & T^{22}_{mlm'l'} \end{pmatrix} \begin{pmatrix} a_{m'l',inc} \\ a_{m'l',inc} \end{pmatrix}. \tag{3.20}$$

The relation defines a matrix called T-matrix with elements $T^{ij}_{mlm'l'}(i,j = 1,2)$. One of

the advantages of T-matrix method is that obtaining the orientation averaged scattering properties would be analytical once the rotation rules for the T-matrix are specified [18]. Let's first rewrite the basic functions in matrix form,

$$\mathbf{Y}_{ml}(\theta,\phi) = (-1)^m \sqrt{\frac{2l+1}{4\pi l(l+1)}} e^{-im\phi} \begin{pmatrix} 0 & 0 & \sqrt{l(l+1)} d^l_{0m}(\theta) \\ i\pi_{ml}(\theta) & \tau_{ml}(\theta) & 0 \\ -\tau_{ml}(\theta) & i\pi_{ml}(\theta) & 0 \end{pmatrix} \tag{3.21}$$

where

$$d^l_{0m}(\theta) = (-1)^m \sqrt{\frac{(l-m)!}{(l+m)!}} P^m_l(\theta) \tag{3.22}$$

$$\pi_{ml}(\theta) = \frac{m}{sin\theta} d^l_{0m}(\theta) \tag{3.23}$$

$$\tau_{ml}(\theta) = \frac{d}{d\theta} d^l_{0m}(\theta) \tag{3.24}$$

and the radial functions

$$\mathbf{Z}_l(kr) = \begin{pmatrix} z_l(kr) & 0 \\ 0 & \frac{1}{kr}\frac{d}{dr}(r z_l(kr)) \\ 0 & \frac{\sqrt{(l+1)l}}{kr} z_l(kr) \end{pmatrix} \tag{3.25}$$

From now on, we use $\mathbf{J}_l(kr)$ to denote this matrix when $z_l(kr)$ is the spherical Bessel function of the first kind j_l, and use $\mathbf{H}_l(kr)$ when $z_l(kr)$ is the spherical Bessel function of the third kind $h^{(1)}_l$. The radial green function can then be written as

$$\mathbf{g}_l(r,r') = \begin{cases} ik\mathbf{H}_l(r)\mathbf{J}^T_l(r'), r > r' \\ ik[\mathbf{H}_l(r)\mathbf{J}^T_l(r') + \mathbf{J}_l(r)\mathbf{H}^T_l(r')]/2, r = r' \\ ik\mathbf{J}_l(r)\mathbf{H}^T_l(r'), r < r' \end{cases} \tag{3.26}$$

where T denotes the transpose operation. At spherical shell $r = r_p$, an integral associated with the refractive index distribution called U matrix can be written in component form as

$$\mathbf{U}_{mlm'l'}(r_p) = r_p^2 \int d\Omega \mathbf{Y}^+_{ml}(\Omega) q(r_p, \Omega) \mathbf{V}(r_p, \Omega) \mathbf{Y}_{m'l'}(\Omega) \tag{3.27}$$

where

$$\mathbf{V}(r, \Omega) = \begin{pmatrix} \frac{1}{\epsilon(r,\Omega)} & 0 & 0 \\ 0 & 1 & 0 \\ 0 & 0 & 1 \end{pmatrix} \tag{3.28}$$

and

$$q(r, \Omega) = k^2(\epsilon(r, \Omega) - 1), \tag{3.29}$$

where the $(+)$ denotes the Hermitian transpose operation, and ϵ is the electric permittivity. The U matrix contains the information of shape and inhomogeneity of the particle. With U matrix, we can compute the Q matrix at the corresponding shell r_p as

$$\mathbf{Q}(r_p) = w_p[\mathbf{I} - w_p \mathbf{U}(\mathbf{r_p})]^{-1} \mathbf{U}(\mathbf{r_p}) \tag{3.30}$$

and $\mathbf{Q}_{ij}$ as

$$\mathbf{Q}_{11}(r_p) = ik\mathbf{H}^T(r_p)\mathbf{Q}(r_p)\mathbf{H}(r_p), \tag{3.31}$$

$$\mathbf{Q}_{12}(r_p) = ik\mathbf{H}^T(r_p)\mathbf{Q}(r_p)\mathbf{J}(r_p), \tag{3.32}$$

$$\mathbf{Q}_{21}(r_p) = ik\mathbf{J}^T(r_p)\mathbf{Q}(r_p)\mathbf{H}(r_p), \tag{3.33}$$

$$\mathbf{Q}_{22}(r_p) = ik\mathbf{J}^T(r_p)\mathbf{Q}(r_p)\mathbf{J}(r_p) \tag{3.34}$$

where the w_p is the integration weights. With the above matrices, the iteration equation

for T-matrix can be written as

$$\mathbf{T}(r_p) = \mathbf{Q}_{22}(r_p) + (\mathbf{I} + \mathbf{Q}_{21}(r_p))[\mathbf{I} - \mathbf{T}(r_{p-1})\mathbf{Q}_{11}(r_p)]^{-1}\mathbf{T}(r_{p-1})(\mathbf{I} + \mathbf{Q}_{12}(r_p)) \quad (3.35)$$

For obvious reason, when $r = 0$, $\mathbf{T} = 0$. The iterative computation of T-matrix can be terminated when U becomes zero, i.e. when the spherical shell contains the particle entirely. The above equations online the computational procedure of the II-TM method, while the detailed derivation of the invariant-imbedding equation can be found in [82]. For complex particle shapes, the computation of U matrix becomes difficult. However, in real environment the particle could be very irregular. In this study, we modified the II-TM code from Lei Bi [19, 20], such that it can deal with the faceted and spherical geometries at the same time.

3.3 Physical-Geometric Optics Hybrid Method

The Physical-Geometric Optics Hybrid method includes two basic computational procedure [83]: first, compute the electromagnetic field on the particle surface or inside the particle by applying a ray-tracing method; second, map the near field into the far field based on either the surface integral equation or the volume integral equation.

In this study, the volume integral mapping procedure for PGOH method is used. Below we briefly introduce the computational procedure of this method. For a specified point inside the particle, the electric field can be written as the summation of fields associated with different orders of reflection and refraction events, i.e.,

$$\overrightarrow{E}(\overrightarrow{r}') = \sum_{p=1}^{N} \overrightarrow{E}_p(\overrightarrow{r}') \quad (3.36)$$

The number of order N is selected such that the field converges with enough accuracy. With the beam-splitting technique, the number of beams only depends on the shape of

the faceted particles and does not increase with the size of particle. This could improve the efficiency of the ray-tracing processes for large particles. At the far field zone, the scattered field can be decomposed with respect to the scattering plane as

$$\overrightarrow{E}^s(\overrightarrow{r}) = E^s_\alpha(\overrightarrow{r})\hat{\alpha} + E^s_\beta(\overrightarrow{r})\hat{\beta} \tag{3.37}$$

where $\hat{\alpha}$ and $\hat{\beta}$ are two orthogonal unit directions, parallel and perpendicular to the scattering plane respectively. The mapping equation can then be expressed as

$$\begin{pmatrix} E^s_\alpha \\ E^s_\beta \end{pmatrix}_{kr\to\infty} = \frac{k^2 e^{ikr}}{4\pi r} \iiint_V (\epsilon - 1) \begin{pmatrix} \hat{\alpha}\cdot\overrightarrow{E}(\overrightarrow{r}') \\ \hat{\beta}\cdot\overrightarrow{E}(\overrightarrow{r}') \end{pmatrix} e^{-(ik\hat{r}\cdot\hat{r}')} d^3\hat{r}' \tag{3.38}$$

where k is the wave number, ϵ is the electric permittivity. The mapping automatically includes the interferences between the diffracted and reflected rays.

Compared to numerical exact methods, the inaccuracy of the PGOH method arises from so-called the edge effect, which can be semi-empirically evaluated by the following formula,

$$Q_{edge,ext/abs} = \frac{f_{ext/abs}}{(kr)^{2/3}} \tag{3.39}$$

where $Q_{edge,ext/abs}$ is the difference of the extinction (absorption) efficiency between he numerical exact methods and PGOH method. $f_{ext/abs}$ is determined by the difference and applied to different sizes of particle.

4. MODELING THE INHERENT OPTICAL PROPERTIES OF AQUATIC PARTICLES*

In this chapter, we first introduce the model, i.e. an the irregular hexahedral ensemble, for simulating the inherent optical properties of aquatic particles. As we've mentioned, Lorenz-Mie theory has been heavily relied on for acquiring the optical properties of the aquatic particles. In the results and discussion, we therefore focus on the comparison between the results based on irregular ensemble models and those based on the spherical models.

4.1 Model and Properties of Interests

An irregular hexahedral ensemble is generated by randomly tilting the faces of multiple regular hexahedra. The method of obtaining an irregular hexahedron from a regular counterpart is detailed in Bi et al. [17] . Different particles in the aquatic environment could have similar shapes, but are rarely identical. This shape variability is characterized through the concept of particle geometric irregularity, which is defined by the degree of randomness in the shape generating process. Specifically, the slopes of each particle facet in an ensemble follow the normal distribution:

$$P(s_x, s_y) = \frac{1}{\pi\sigma^2} exp(-\frac{s_x^2 + s_y^2}{\sigma^2}) \tag{4.1}$$

where s_x and s_y are the slopes along two orthogonal directions with respect to the original facet, and σ^2 is the particle geometric irregularity parameter. Figure 4.1 shows the geometry of a group of particles with a geometric irregularity $\sigma^2 = 0.4$.

*Part of this chapter is reprinted from Journal of Quantitative Spectroscopy & Radiative Transfer, 191, 30-39, 2017, Xu, G., Sun, B., Brooks, S.D., Yang, P., Kattawar, G.W. and Zhang, X, "Modeling the inherent optical properties of aquatic particles using an irregular hexahedral ensemble", Copyright 2017, with permission from Elsevier.

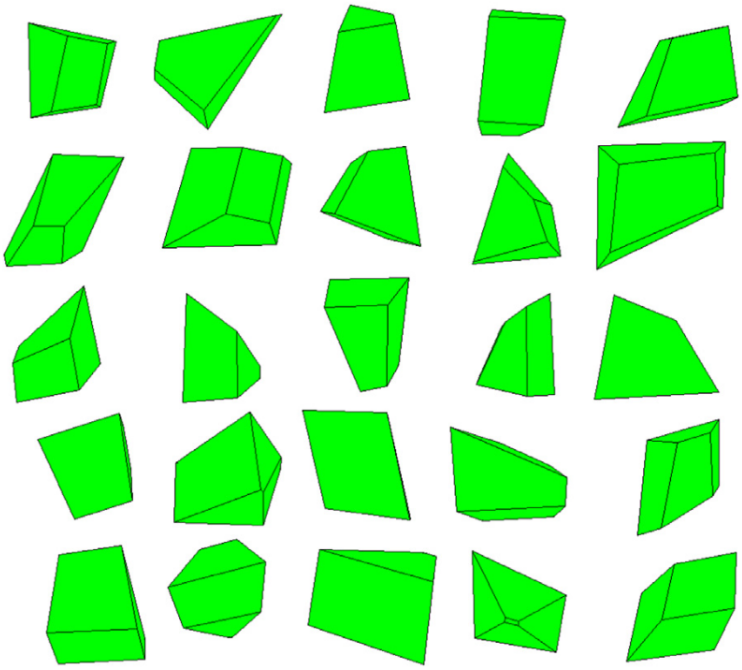

Figure 4.1: A particle group composed of 25 irregular hexahedra with a geometric irregularity value of 0.40

A study from Liu et al. [84]concludes that the particle geometric irregularity is optically equivalent to the particle surface roughness. In this study, a hexahedral ensemble has 25 randomly generated shapes. The IOPs of a hexahedral ensemble are obtained via two steps of calculation. The first step is to perform the orientation average for each individual shape. For the size range (small size) handled by II-TM, the orientation average can be evaluated with an analytical form, whereas for the size range (large size) handled by PGOH, 2000 orientations are used. The second step is to perform the average of the IOPs over all 25 particle shapes. The scattering phase matrix P_{ij} , extinction efficiency Q_{ext} ,

and absorption efficiency Q_{abs}, are obtained using the following formulas:

$$P_{ij}(\theta) = \frac{\sum_{k=1}^{25} C_{k,sca} P_{ij,k}(\theta)}{\sum_{k=1}^{25} C_{k,sca}}, \tag{4.2}$$

$$Q_{ext/abs} = \frac{\sum_{k=1}^{25} C_{k,ext/abs}}{\sum_{k=1}^{25} S_k/4}. \tag{4.3}$$

The ratio of water-leaving spectral radiance to the solar downwelling irradiance forms the spectral remote sensing reflectance, a fundamental quantity an airborne ocean color sensor measures. Under the quasi-single-scattering approximation, the reflectance of the water body is proportional to the Gordon parameter, which is determined by IOPs of water constituents [1] in the form

$$G = \frac{\sigma(c)\kappa + b_w}{\sigma(c)\kappa + a_p(c) + b_w + a_{cdom} + a_w} \tag{4.4}$$

where $a_p(c)$ and $\sigma(c)$ are the particulate bulk absorption and scattering coefficients respectively as functions of particle concentration c, κ is the particulate backscattering ratio, b_w is the backscattering coefficient of water, a_{cdom} is the absorption coefficients of colored dissolved organic matter, and a_w is the absorption coefficient of pure water. Values of a_p and σ both increase with particle concentration, c, which can be evaluated through integration of the absorption and scattering cross sections respectively over a range of particle size, while κ is evaluated through integration of the VSF over the backscattering hemisphere normalized by the bulk scattering coefficient. The bio-optical models often utilize the spectral absorption of the marine particles to infer the concentration of the biomass. However in some cases the marine particle back-scattering will dominate the absorption, exhibiting high reflectivity from the water volume (e.g., a bloom of E. huxleyi [85]). These situations generally coincide with a high c, in which the Gordon parameter depends largely on the IOPs of the particulate matter. In these cases, the Gordon parameter can be approx-

imated by

$$G = \frac{\sigma(c)\kappa + b_w}{\sigma(c)\kappa + a_p(c) + b_w + a_{cdom} + a_w} \approx \frac{\sigma(c)\kappa}{\sigma(c)\kappa + a_p(c)} \tag{4.5}$$

where c is large. It is therefore of particular interest to model the reflectivity of marine particles through their IOPs.

The particle size distribution is assumed to be of the Junge type (power law distribution) [86] [34] given by

$$\frac{dN(r)}{dr} = Ar^{-\xi}, \tag{4.6}$$

where A is the number concentration factor, and ξ is the differential Junge slope. The particle size is defined in terms of the volume-equivalent-sphere radius. To evaluate the influence of the integrated size range on resultant scattering properties, we introduce a constant by setting the following relation

$$(r_{min}, r_{max}) = (\rho r_1, \rho r_2) = \rho(r_1, r_2), \tag{4.7}$$

where (r_1, r_2) is the reference size range, (r_{min}, r_{max}) is the range for integration over particle size, and ρ is a constant referred to as the size range ratio. The integration size range (r_{min}, r_{max}) can be determined by setting ρ to a constant value and choosing a reference size range (r_1, r_2). Since scattering properties are determined by the ratio of particle size to the incident wavelength, a shifted size range is equivalent to a shifted incident wavelength when the refractive index is constant. Particles in the aquatic medium include living organisms (e.g., bacteria, phytoplankton, zooplankton), organic detritus, and minerogenic particles. Organic particles normally have greater water content than minerals, and therefore have lower indices of refraction, while those with inorganic origin have higher indices of refraction. The in situ measured VSF can be evaluated by a two-component model, namely a sum of contributions from organic and inorganic particles.

We use the following equation to calculate the VSF:

$$\beta(\theta) = \int_{r_{min}}^{r_{max}} [f_o P_{11,o}(\theta, r) C_{sca,o}(r) \frac{dN_o}{dr}(r) + f_i P_{11,i}(\theta, r) C_{sca,i}(r) \frac{dN_i}{dr}(r)] \qquad (4.8)$$

where f_o and f_i are the concentration fractions of organic particles and inorganic particles respectively. Hence $f_o + f_i = 1$. $N_o(r)$ and $N_i(r)$ are the size distributions of each type of particle. Note that the bulk polarimetric properties can also be evaluated by Eq. (4.8).

4.2 Results and Discussions

For aquatic particles, which are optically soft, different approximation methods can be applied to calculate the scattering properties according to their particle sizes and refractive indices.For particle size from small to large, the Rayleigh Approximation (RA), Rayleigh-Gans-Debye (RGD) Approximation, the Anomalous Diffraction Approximation (ADA), and Geometric Optics (GO) method can be accordingly applied. II-TM is found to be valid up to and including the ADA region (a few microns), while the PGOH method is used for larger particles. A comparison between the II- TM and PGOH methods is shown in Figure 4.2. Compared to P_{11}, the differences of polarimetric scattering properties between methods are generally larger. In addition to the approximate nature of geometric optics, the orientation averaging procedure for PGOH also contributes to this discrepancy. For larger particles, angular scattering properties (especially polarimetric properties) are more sensitive to particle orientation with respect to the incident wave. The comparison demonstrates reasonable consistency between the numerically accurate method II-TM and the approximate PGOH method, thus demonstrating the capability of expanding the size parameter range of our models.

To mimic the uncertainty regarding the shapes of a group of suspended particles in a real aquatic environment, we introduce the concept of geometric irregularity in computing IOPs. Figure 4.3 displays an example of the scattering phase matrices of 25 shapes and

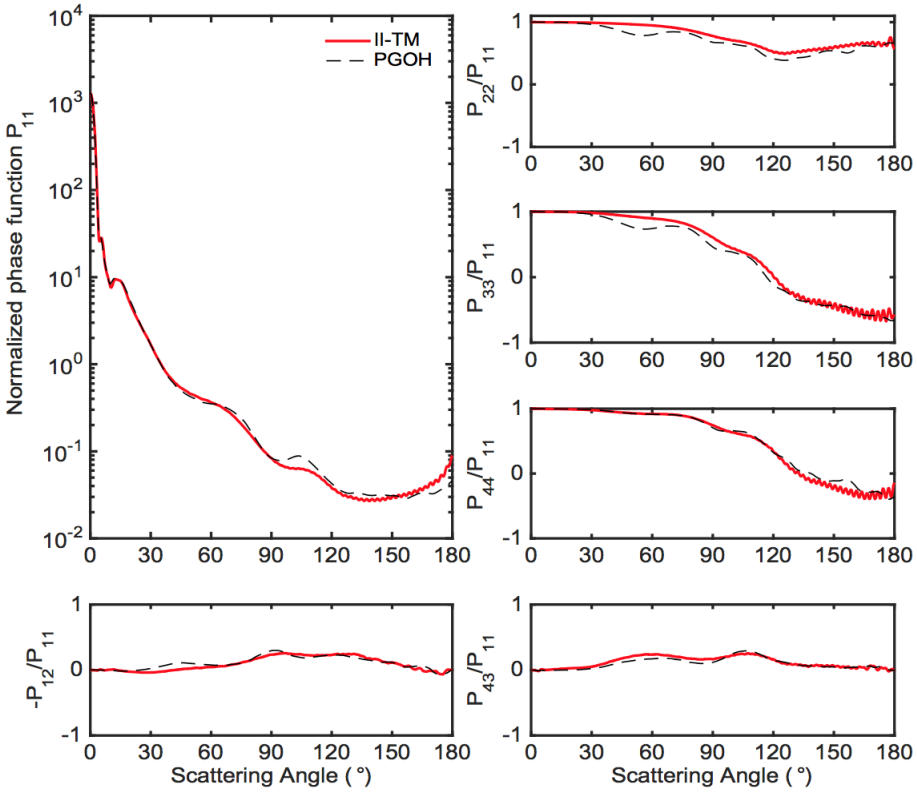

Figure 4.2: Nonzero elements of the scattering phase matrix of a single distorted hexahedron simulated by the II-TM and PGOH methods. The particle size is $5.0\mu m$, the refractive index is $1.20 + 0.0005i$, and the incident wavelength is $658nm$.

their ensemble average. The result reveals that geometric variation produces pronounced variations in the scattering matrices for those particles. This shape-dependent pattern poses a great challenge for accurately simulating the VSF of marine particles. By computing the ensemble average of all shapes, a relatively featureless scattering phase matrix is generated as a proxy for the group.

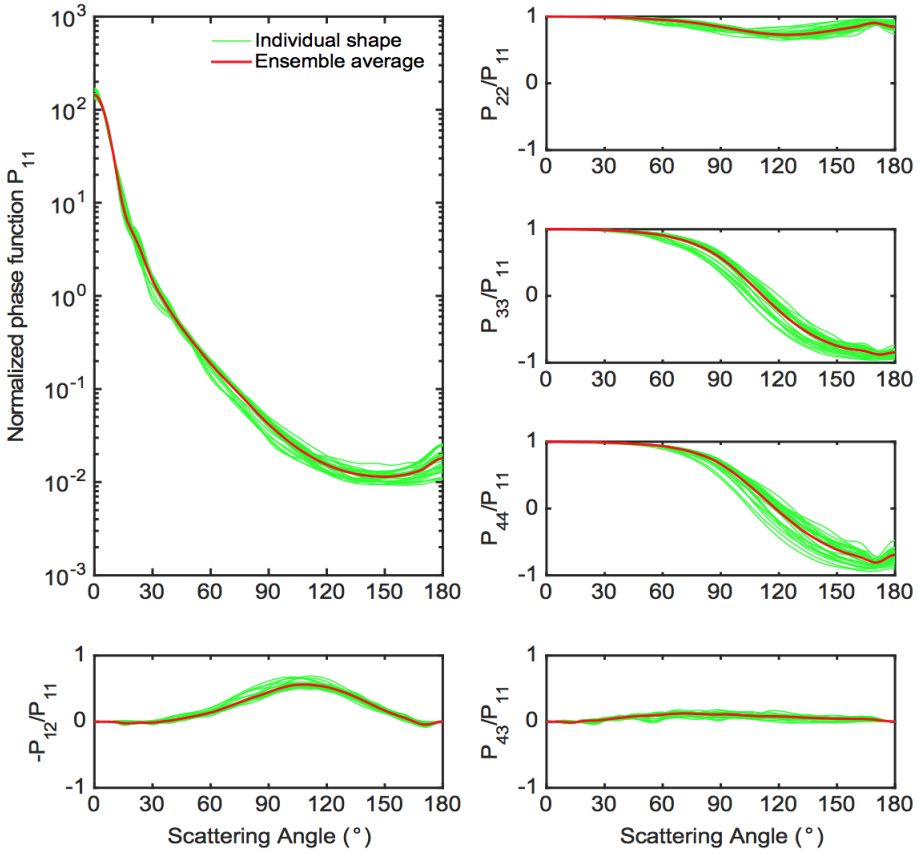

Figure 4.3: Nonzero elements of the scattering phase matrix of individual irregular hexahedra (in green) and their ensemble average counterpart (in red). The geometric irregularity parameter for the particle ensemble is 0.4, particle size is $1.48\mu m$ in terms of volume-equivalent sphere radius, particle aspect ratio is 1.0, the particle refractive index is $1.20 + 0.0005i$, and the incident wavelength is $658nm$.

In contrast to the sensitivity of the scattering phase matrix to particle shape, we find that shifting the geometric irregularity parameter from one value to another seems to have much smaller impact on the scattering phase matrix (for $\sigma^2 > 0.05$). Figure. 4.4 demonstrates two ensemble-averaged scattering phase matrices with geometric irregularities of $\sigma^2 = 0.4$ and 0.05. Distinct differences can only be seen in P_{11} at large scattering angles (120 to 180 degrees). The result reveals the strong constraints in simulating angular scattering properties posed by averaging over particle shapes.

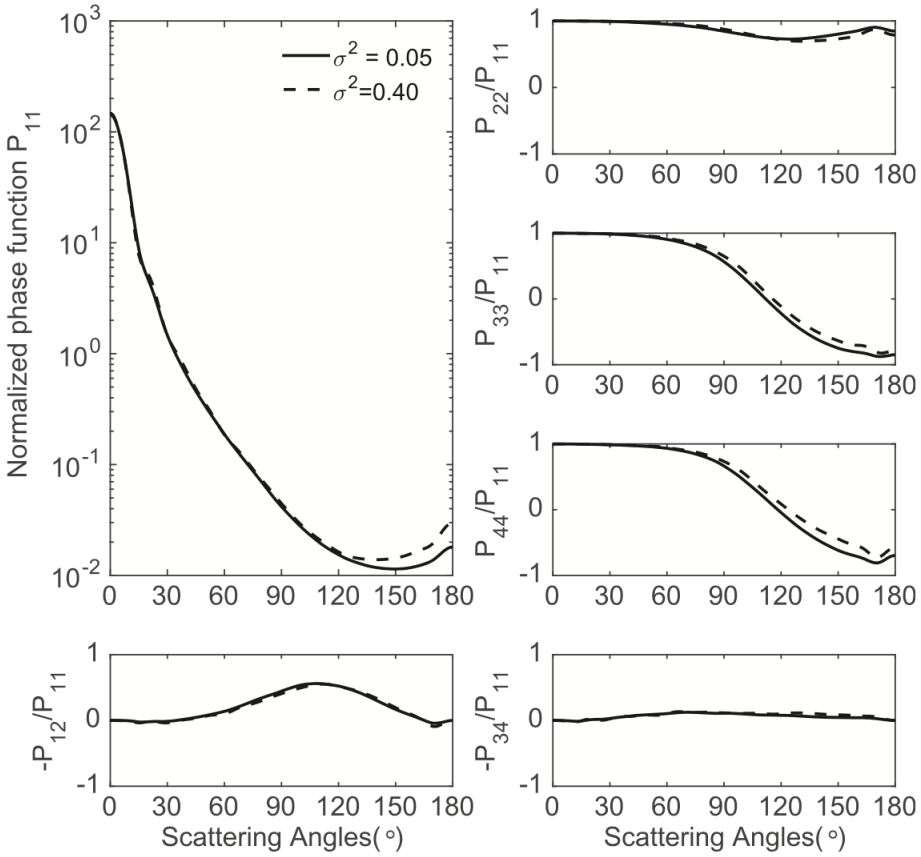

Figure 4.4: Nonzero elements of the scattering phase matrices simulated for two hexahedral ensembles with geometric irregularity parameters 0.4 and 0.05. The other parameters used are the same as in Figure 4.3. The particle size is defined with respect to the volume-equivalent-sphere radius.

Figure 4.5 displays the integral scattering properties (i.e. extinction efficiency Q_{ext} , absorption efficiency Q_{abs} , asymmetry factor f , and single-scattering albedo ω) as functions of particle size for hexahedral and spherical models. The edge effects on the extinction and absorption efficiencies are very small and therefore not shown in the figure for the sake of clarity. A refractive index $1.05 + 0.002i$ is used in the calculations. In the figure, different optical regions are marked approximately with dashed vertical lines over the entire size range. Differences between the two models for these IOPs are summarized as follows. For the extinction efficiency and scattering albedo, the spherical model demonstrates an oscillatory pattern within intermediate size particle regions (RGD and ADA), whereas all scattering properties vary smoothly for the hexahedral model from the RA to the GO region.

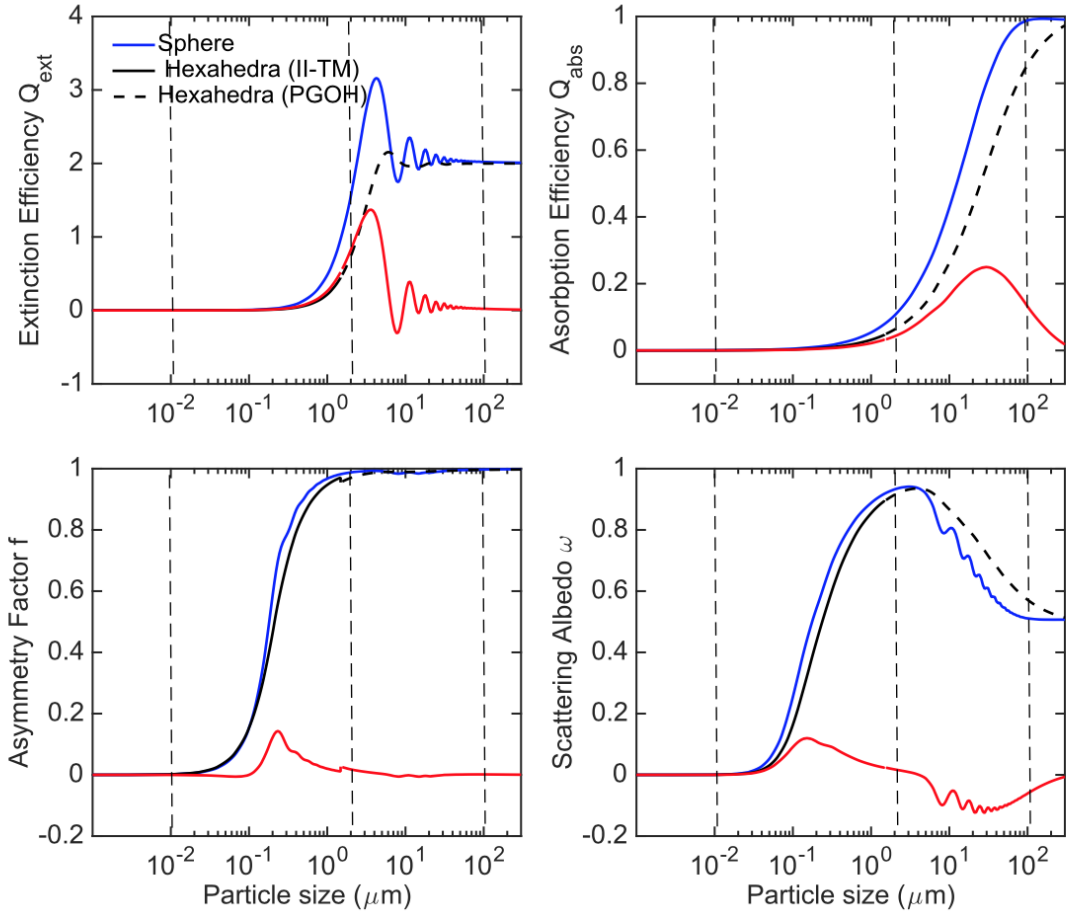

Figure 4.5: Integral scattering properties of a hexahedral ensemble and a sphere. The red line indicates the differences between the two models (spheres minus hexahedra). The particle size varies from to, the refractive index is, particle aspect ratio is 1.0, the particle geometric irregularity is 0.4, and the incident wavelength is $658nm$. The vertical dashed lines roughly mark the different optical regions, namely the RA, RGD, ADA, and GO regions.

The extinction efficiencies for both models approach the geometric optics asymptotic value, 2, as size increases. The oscillation pattern leads to a maximum value of the extinction efficiency for spheres that is much larger than that for the hexahedral ensemble. Within the RGD and ADA regions, the extinction coefficients of a marine particle assemblage estimated by a spherical model could be larger than those estimated by a hexahedral

ensemble. The absorption efficiency estimated by the spherical models is equal to or larger than that estimated by the hexahedral models in all optical regions. This is consistent with the finding that spheroids produce lower or equal absorption efficiency than spheres regardless of particle size and aspect ratio [16]. The asymmetry factors predicted by both models have a similar curve, but within the RGD and ADA regions, spheres predict a higher asymmetry factor than those obtained from hexahedra, which corresponds to a stronger forward scattering phase function. Note that this feature is also found when comparing Lorenz-Mie scattering simulations with the laboratory-measured scatter- ing function of aquatic particles [10]. The single scattering albedo predicted by spherical models has a similar but shifted shape to that of hexahedral models. Both curves approach an asymptotic value of one half in the geometric optics region. However for sizes within RGD regions, the predictions from hexahedral models are larger than those from spherical models, whereas in the ADA and GO regions, the predictions are smaller. In other words, spheres underestimate the scattering effect in the RGD region and over- estimate the scattering effect within the ADA and GO regions. Such differences of IOPs in various optical regions lead to different bulk scattering behaviors between models, especially for an assemblage with sizes that are confined to the intermediate optical regions.

Next we discuss the bulk scattering properties in the backward direction. The backscattering properties are of major significance in optical remote sensing in oceanography, because reflectance is dominated by the ratio of backscattering coefficients to absorption coefficients [1]. Modeling backscattering properties accurately is a difficult task, since they are highly sensitive to morphological details of particles. Currently the interpretation of backscattering measurements in most studies largely relies on Mie scattering calculations [87, 88, 89, 90], even though the nonspherical effects and internal inhomogeneity are found to be important [13, 14, 15, 16]. Figure 4.6 displays the backscattering ratio variation with size distribution in terms of differential Junge slope for different compositions, shapes and

integration size ranges. The integration size range from $0.1\mu m$ to $1.0\mu m$corresponds to plankton size group picoplankton, while $1.0\mu m$ to $10.0\mu m$ corresponds to nanoplankton.

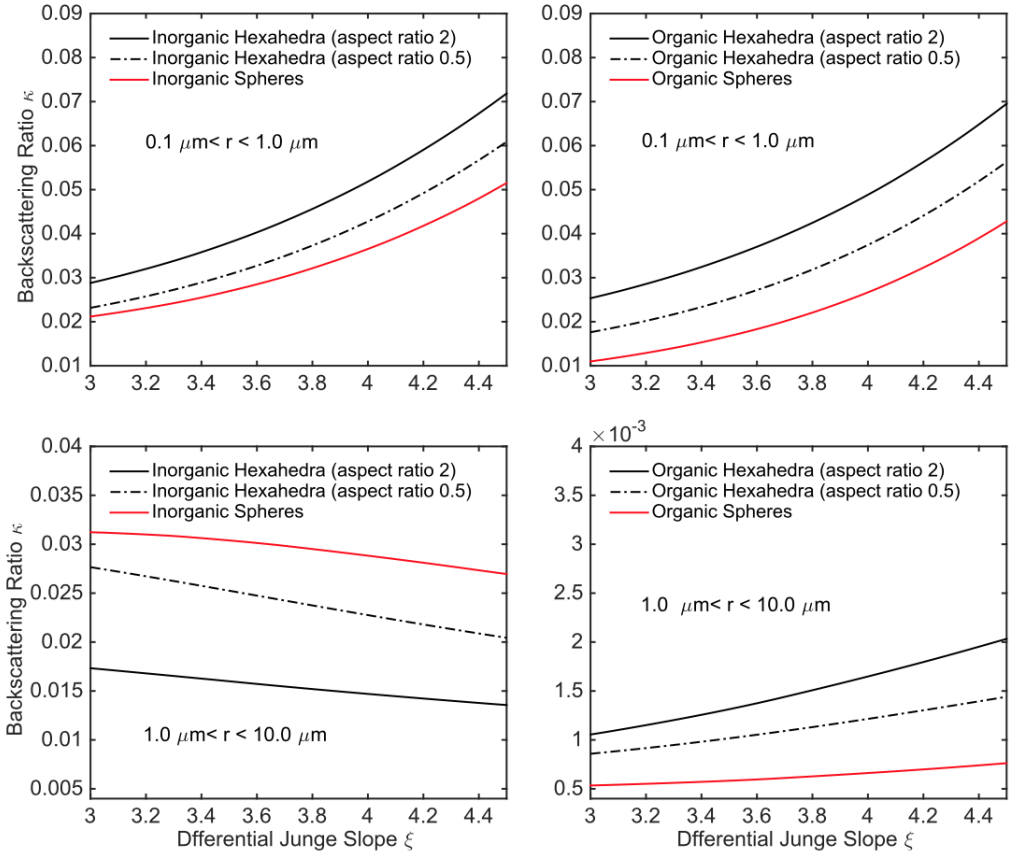

Figure 4.6: Backscattering ratio as a function of size distribution in terms of differential Junge slope for different models, compositions and integrated size ranges. The refractive index is assumed to be $1.05 + 0.002i$ for organic particles, whereas it is assumed to be $1.20 + 0.0005i$ for inorganic particles. The particle geometric irregularity parameter is 0.4, and the incident wavelength is $658nm$.

Two hexahedral ensembles that are statistically associated with aspect ratios 2 and 0.5 are used in the comparison. The magnitude of backscattering ratio displays a higher sensitivity to size groups for the organic particles than for the inorganic particles. A spher-

ical model produces smaller backscattering ratios than the predictions from hexahedral models for the organic particles regardless of the size group and aspect ratio. For inorganic particles, the sign of the biases is dependent on the particle size group. Specifically the spherical model produces higher backscattering ratios than the hexahedral model for nanoplankton size group, but lower back- scattering ratios for picoplankton size group. Because the backscattering ratio generally increases with a larger real part of the refractive index, and the backscattering ratio and size distribution are in-situ measurable quantities, the relations revealed in the figure can be used to estimate the refractive indices of marine particles (for a given geometric irregularity in the case of hexahedra). Such studies are normally conducted using spherical models [3]. The figure indicates some biases caused by the spherical model employed in these studies. If a hexahedral ensemble is employed, the inferred refractive index for the organic particles will be lower than inferred from the spherical model, since hexahedral model predicts a higher backscattering ratio than spheres for both particle size groups. But for the inorganic particles, the sign of biases caused by spherical model is uncertain, depending on particle size group.

Compared to the backscattering ratio, the optical signal received by a remote sensor is more sensitive to the Gordon para- meter. Figure 4.7 displays the Gordon parameter simulated from an organic hexahedral ensemble and spheres as a function of integration size range. The reference size range is from $0.1\mu m$ to $20\mu m$, covering both picoplankton and nanoplankton. A differential Junge slope of 4.0 is assumed for the calculation. The size range ratios from 0.7 to 1.7 are selected so that the incident wavelengths are equivalently confined to $300nm$ to $700nm$ for the reference size range. Both models predict a decreasing trend of the Gordon parameter towards large size range ratios (or shorter wavelengths for the particle assemblage of reference size range), resulting from a decrease in the ratio of backscattering to absorption coefficients. The decreasing slope as well as the average magnitude of the Gordon parameter are the main differences between the two models. As

size range ratio increases, the Gordon parameter simulated based on a hexahedral ensemble is larger and decreases less drastically than that based on spheres. The magnitude of the Gordon parameter simulated from a hexahedral ensemble could be twice that from spheres of the same size. This suggests that particle morphology is important in accounting for the reflectivity of the particle assemblages.

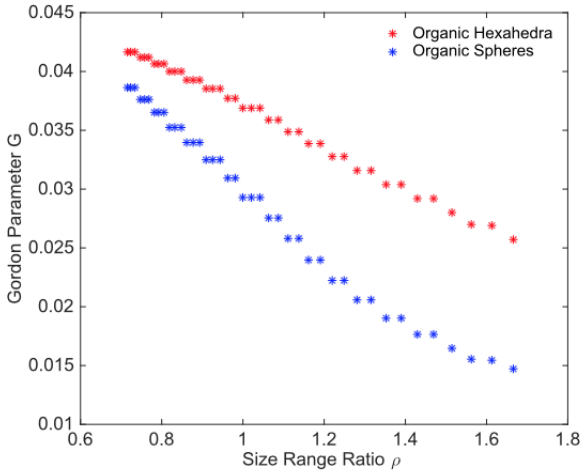

Figure 4.7: Gordon parameter as a function of particle size range ratio, using spherical and hexahedral models. The refractive index used is $1.05 + 0.002i$, particle aspect ratio is 1.0, geometric irregularity is 0.4, the reference size range is from $0.1\mu m$ to $20\mu m$, and the incident wavelength is $500nm$.

Particles with organic and inorganic origins constitute two major categories of optically important particles in the aquatic medium. Next we compare the scattering phase matrices between the organic and inorganic particles using a hexahedral ensemble with a geometric irregularity parameter of 0.4. The results are shown in Figure 4.8. The refractive indices chosen are relatively extreme for aquatic particles. For particles with organic origins, refractive index $1.01 + 0.0i$ is assigned, and for particles with in- organic origin, $1.20 + 0.0005i$ is assigned. The P_{11} comparison suggests that the backscattering intensity

of inorganic particles is much higher than for organic particles. In addition, the polarimetric scattering properties of inorganic particles differ considerably from organic particles, which have a scattering pattern similar to Rayleigh scattering. As the real part of the organic particle refractive index increases, the backscattering part of the P_{11} curve increases and approaches that of the inorganic particle (not shown).

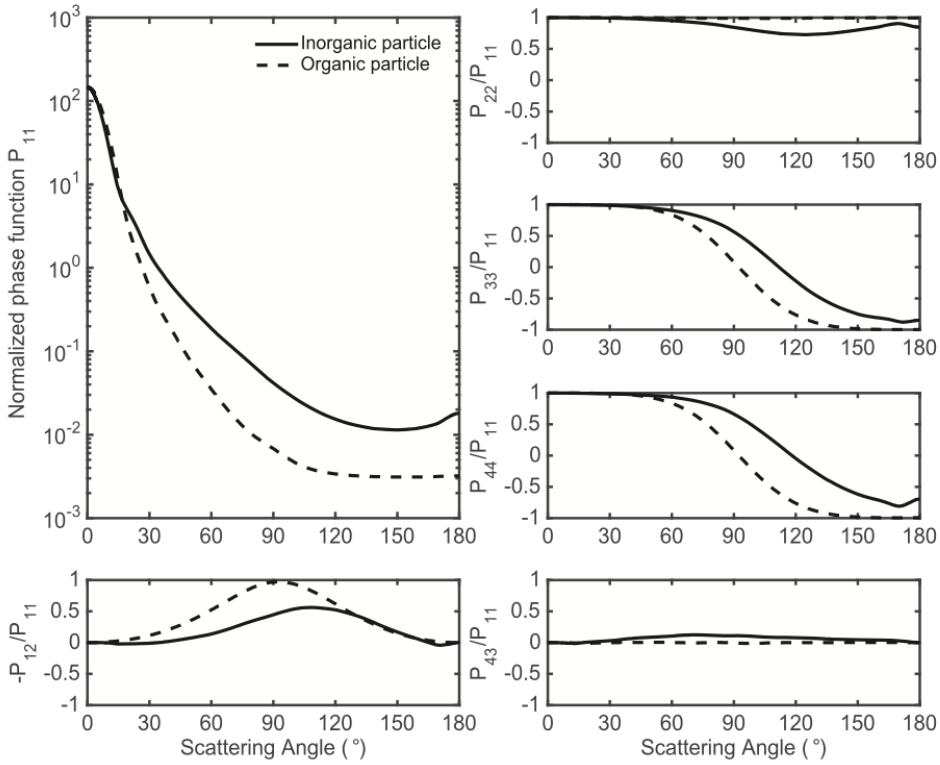

Figure 4.8: Nonzero elements of the scattering phase matrices of organic and inorganic aquatic particles, simulated by a hexahedral ensemble with a geometric irregularity parameter of 0.4 and aspect ratio 1.0 . A refractive index $1.20 + 0.0005i$ is used for the inorganic particle, and $1.01 + 0.0i$ is used for the organic particle. The compared particle size is $1.48\mu m$, and the incident wavelength is $658nm$.

The two-component model that separately accounts for contributions from organic and inorganic particles can be applied to analyze the in situ measured data. Previously, a

spherical two- component model has been utilized to interpret the in-situ mea- sured VSF in the Sargasso Sea [5] . In this study, we use a two-component hexahedral model to fit the widely used average VSF measured by Petzold [91]. The VSF of the two component model is evaluated using Eq.(4.6), in which three parameters are inferred from a best fit, i.e. the organic fraction, and two differential Junge slopes for the size distributions of organic and inorganic particles. The upper panel in Figure 4.9 displays the best fitting curve simulated from hexahedra as well as the spherical counterpart using the inferred parameters. Similar to the study in the Sargasso Sea, a large proportion of organic particles (97.1%) has to be assumed to obtain the best fit. The analysis for the Sargasso Sea indicates that only a combination of small organic particles and large inorganic particles can account for the measurements. Here, using the same integration size range for both organic and inorganic particles, the inferred differential Junge type slope of 3.96 for the organic particles, is just slightly lower than 4.095 for the inorganic particles. The inferred slope values of 4 are in agreement with the global ocean mean. This is in contrast with the previous finding in the Sargasso Sea since no significant difference between organic and inorganic particles is found in terms of particles size distributions. We also compute the VSF using spherical model with the inferred size distributions and organic fraction. Large differences are found in the backscattering hemisphere (90 to 180 degrees) between hexahedral and spherical models, whereas the VSF at forward scattering angles (0 to 90 degrees) for both models are quite similar. In the backscattering hemisphere, the VSF simulated from the spherical models appears to be more oscillatory than both the measurement and the simulation by hexahedral models. In particular, the exact backscattering peak produced from the spherical model is much higher than from either measurement or simulations from the hexahedral model. This is the well known glory peak, which is virtually unique to spheres. We notice that the measured VSF also has a oscillation pattern over the angular range from 120^o to 180^o, while the hexahedral model seems to better pre-

dict the average magnitude, rather than the oscillation pattern within the range. This may due to the fact that the organic particles often have smooth surfaces, rather than the sharp edges that a hexahedral model has. In addition to the VSF, we also compare the degree of linear polarization, using the inferred size distributions and organic fraction for both models, which is displayed in the lower panel in Figure 4.9. Since Petzold's data does not include polarimetric measurements, the measured data is not shown. From the figure, a hexahedral two-component model predicts a higher peak of linear polarization than the prediction from a spherical two-component model. Apparent inconsistency of linear polarization between the two models is shown for both backscattering and forward scattering hemispheres. The inconsistency could be larger if different parameters are inferred (e.g., if the differential Junge slope for the inorganic particles is smaller), whereas the VSFs would remain similar in the forward scattering hemisphere.

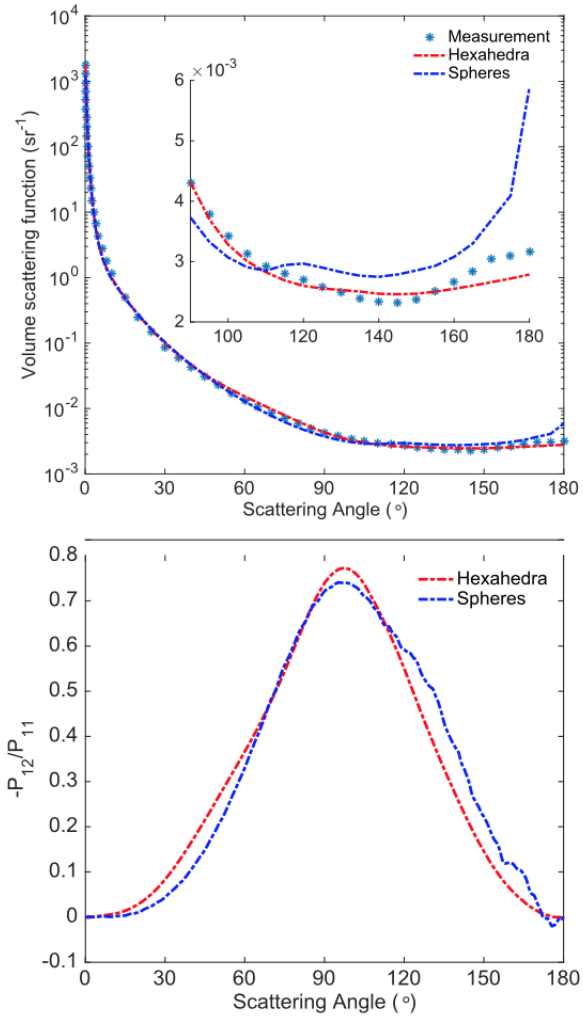

Figure 4.9: Upper panel: Measured VSF from Petzold and the best-fit curve simulated from a two-component hexahedral ensemble and its spherical counterpart using the same organic fraction and particle size distributions. Lower panel: The degree of linear polarization from hexahedral and spherical models with respect to the best fit. The particle sizes range from $0.001\mu m$ to $69.5\mu m$, and the refractive indices used for organic and inorganic particles are $1.20 + 0.0005i$ and $1.01 + 0.0i$, respectively. The particle geometric irregularity parameter is 0.4, and aspect ratio is 1.0.

4.3 Summary and Conclusions

In contrast to using a spherical shape model, we employ a randomly generated hexahedral ensemble to evaluate the IOPs of aquatic particles. We demonstrate that the aspect ratio parameter used to statistically characterize the particle geometry provides effective constraints on the modeling of shape-dependent angular scattering properties. A computationally practical method using II- TM and PGOH allows us to simulate the IOPs of aquatic particles in a broad size range from the RA to the GO regions. In this study, we discussed various aspects of IOPs of a hexahedral ensemble model, highlighting the differences between this model and the widely used spherical model. In the intermediate particle size range (RGD and ADA regions), where most marine particles are found, the predicted absorption and extinction efficiencies by a hexahedral ensemble are overestimated where a spherical shape is assumed. This is consistent with similar findings from spheroid-sphere comparisons [16]. For organic particles, the asymmetry factor predicted by a hexahedral ensemble is smaller than the prediction based on spheres, producing a less steep phase function. The spherical model also underestimates the single scattering albedo of a hexahedral ensemble within the RGD region, whereas it overestimates the single scattering albedo within the ADA region. These size-resolved differences give rise to differences in bulk scattering properties that are dependent on the form of the particle size distribution between the two models. We examine the differences of the backscattering ratio and Gordon parameter be- tween a hexahedral ensemble and spheres. For particles with organic origin, the backscattering ratios predicted by the spherical model are generally smaller than those predicted by the hexahedral ensemble. The sign of the backscattering ratio bias for in- organic particles depends on the particle size range. For the size range relating to picoplankton and nanoplankton, the Gordon parameter simulated by a hexahedral ensemble can be under- estimated using a spherical model by a factor of two. The inherent

differences between the two models are also manifested in the VSF comparison. The data-model comparison demonstrates that a two-component hexahedral ensemble reproduces the measured VSF in the backscattering hemisphere, while a spherical model displays an unrealistic peak in the backscattering direction. In the forward scattering hemisphere, distinct differences between the two models can be seen only through polarimetric properties, e.g. the degree of linear polarization. The overall analyses in this study illustrate the limits of a spherical model. On the other hand, the results reveal the potential applicability of a hexahedral ensemble model in modeling the IOPs of marine particles. Future work is needed to explore various shape parameters statistically associated with an irregular hexahedral ensemble, such as the aspect ratio, geometric irregularity, inhomogeneity and the comparisons with other nonspherical models (e.g. spheroid).These investigations could provide deeper insights into the morphological impact of IOPs of marine particles.

5. MODELING THE SINGLE AND MULTIPLE SCATTERING PROPERTIES OF THE SOOT-LADEN MINERAL DUST AEROSOLS*

In this chapter, we present a numerical study on the single and multiple scattering properties of soot-laden mineral dust aerosols. We first introduce the fractal morphologies employed for modeling the single scattering properties of soot particles, pure dust , and dust-soot aggregates. Then we discuss the numerical results in comparison with other studies, by which the applicability of these models is accessed. Next, we introduce the parameterization scheme for the bulk properties. Last, we discuss the multiple scattering properties and the associated uncertainties on either forward modeling processes or on the retrieval processes.

5.1 Particle Models and Properties of Interests

Freshly emitted black carbon tends to have a complex chain-like structure and becomes more compact as the particle ages [92, 93]. Given such morphological complexity and variability, modeling the single-scattering properties of black carbon is not a trivial task. To circumvent this difficulty, it was commonly assumed in the past that soot particles could be sufficiently described by a spherical shape. Unfortunately, the spherical approximation may lead to large errors for both single-scattering calculations and radiative forcing estimates [94, 95].

A more realistic model for soot particles is the aggregation of numerous spherical monomers [96]. However, this model introduces more degrees of freedom than using the spherical approach. In addition, the variable irregular shape of a mineral dust particle can lead to a large uncertainty in modeling its single scattering properties. All these uncer-

*Part of this chapter is reprinted from Optics Express, 25(24), pp.A990-A1008, 2017, Xu, G., Stegmann, P.G., Brooks, S.D. and Yang, P., "Modeling the single and multiple scattering properties of soot-laden mineral dust aerosols", Copyright 2017, with permission from OSA.

tainties should be reasonably constrained before one can investigate the mixing effects on their bulk scattering properties.

The morphology of a soot particle can be characterized by [96]

$$N_m = k_o(\frac{R_g}{a})^{D_f} \tag{5.1}$$

where N_m is the total number of monomers, k_o is a constant called the fractal pre-factor, R_g is the radius of gyration, a is the radius of each monomer, and D_f is the fractal dimension. The fractal dimension determines the compactness of the particle, and hence influences the efficiency of the particle to extinguish light. In this study, we focus on relatively aged soot particles and the fractal dimension is between 2 and 3. This scaling law provides a realistic description of the overall morphological structure of black carbon particles.

Table 5.1 lists the morphological parameters used in this study, where L is the major axis of the particle, defined as the maximum distance between any two monomers' center at A and B, W is the minor axis of the particle, defined as the maximum distance between any two monomers in a plane perpendicular to and across the center of AB, AR is the aspect ratio of L to W, r is the particle radius in terms of volume equivalent sphere. The particle aspect ratio is confined to the range of 1.3 to 1.8 [55]. Two fractal dimensions 2.5 and 2.2 are selected to represent particles with different degrees of compactness. Figure 5.1 illustrates the morphology of $S6$ from Table 5.1. To compute the single-scattering properties of these soot model particles, we employ the semi-analytical Multiple Sphere T-matrix method [97].

To improve upon the commonly used spheroidal model with a smooth surface for mineral dust particles, we employ a fractal polyhedron with randomly tilted facets to model the single-scattering properties of pure mineral dust [98]. According to in-situ measurements [99, 100, 101], the median particle aspect ratio of a mineral dust particle tends to

Case	N_m	L(μ m)	W(μ m)	AR	r(μ m)	D_f
S1	80	0.33	0.24	1.39	0.086	2.5
S2	120	0.40	0.24	1.66	0.099	2.5
S3	200	0.44	0.30	1.45	0.12	2.5
S4	280	0.53	0.33	1.60	0.13	2.5
S5	80	0.41	0.25	1.64	0.086	2.2
S6	120	0.53	0.30	1.76	0.099	2.2
S7	200	0.60	0.40	1.49	0.12	2.2
S8	280	0.78	0.47	1.67	0.13	2.2

Table 5.1: The parameters of soot models.

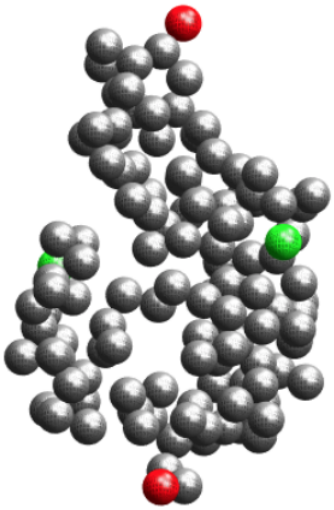

Figure 5.1: Particle shape for case S6. A line connecting the red colored monomers is the major axis of the particle, while the green colored monomers denote the minor axis of the particle.

be in the range of 1.4 to 1.9. In this study, 1.7 is assigned to the pure dust particle model. Figure 5.2 shows a particle shape with 24 facets used in the single-scattering calculation for a pure mineral dust particle.

The mixing of black carbon and mineral dust aerosol can be either external or semi-

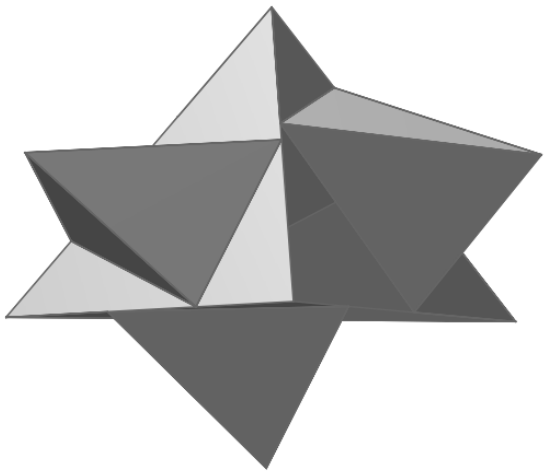

Figure 5.2: Particle shape for a pure mineral dust particle.

external [42, 102, 103, 104]. In this study, ”semi-externally mixed” refers to cases in which soot is attached to the surface of the mineral dust. Due to the agglomeration of black carbon, the single-scattering properties of a semi-external mixture are generally different from their externally mixed counterparts. These differences may include a reduced single-scattering albedo, depolarization ratio, and may subsequently give rise to differences in the multiple scattering properties [105] . The semi-externally mixed model (aggregate model) has a morphology displayed in Figure 5.3.

The semi-externally mixed particle is modeled using simple spheres as a representation for the soot attached to the random Koch fractal. Using a fractal structure for the mineral dust particle and the attached soot at the same time would lead to a much poorer convergence in the single-scattering calculations, rendering such an approach impractical. Without providing appreciable differences in the results, the soot attachments are assumed to be comparatively small. Table 5.2 lists the parameters of the dust models used in this study, where VMR is the volume-mixing ratio (the ratio of the volume of soot to the vol-

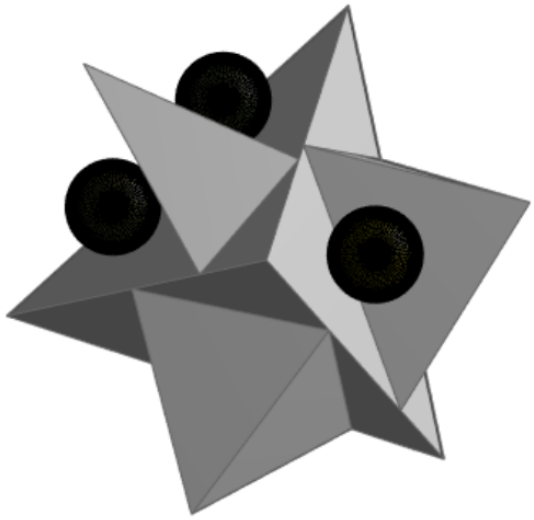

Figure 5.3: The particle shape of a dust-soot aggregate.

ume of the host particle), N_s denotes the number of the attached soot particles, and r denotes the radius of the whole particle. For the aggregate particle, one spherical soot globule has around 1.48% of the volume of the host particle. We apply the semi-analytical invariant imbedding T-matrix method [106, 20] to compute the single-scattering properties for both pure dust and dust-soot aggregates.

Case	VMR	N_s	AR	r(μm)
D1	0%	0	1.7	0.31
D2	0%	0	1.7	0.60
D3	0%	0	1.7	0.97
D4	2.9%	2	1.7	0.31
D5	2.9%	2	1.7	0.60
D6	2.9%	2	1.7	0.97
D7	5.8%	4	1.7	0.31
D8	5.8%	4	1.7	0.60
D9	5.8%	4	1.7	0.97

Table 5.2: The parameters of dust models.

The particle size distribution of dust particles $n(r)$ [107]is assumed to be a gamma distribution,

$$n(r) = \frac{\mathrm{d}N(r)}{\mathrm{dr}} = \frac{1}{\Gamma(\frac{1-2\nu_e}{\nu_e})}(\nu_e r_e)^{\frac{2\nu_e-1}{\nu_e}}(r^{\frac{1-3\nu_e}{\nu_e}})(e^{-\frac{r}{v_e r_e}}) \tag{5.2}$$

where N is the total number of particles, r is particle radius, nu_e is the effective variance (set to be 0.2), and r_e is the effective radius. This form of the size distribution ensures its normalization to unity and is convenient to use.

In addition to polarized reflectivity and scattering phase matrix, the following properties are also discussed in this study:

(1). The mass scattering and absorption coefficients (MSC, MAC):

$$MSC = \frac{C_{sca}(r)}{\rho(4/3)\pi r^3}, \tag{5.3}$$

$$MAC = \frac{C_{abs}(r)}{\rho(4/3)\pi r^3} \tag{5.4}$$

where ρ is the effective density of the particle.

(2).The single-scattering albedo:

$$\omega = \frac{\sigma_p}{\alpha_p+\sigma_p} \tag{5.5}$$

(3) The asymmetry factor :

$$g = \frac{1}{2}\int_{-1}^{1} P_{11}(cos(\theta))cos(\theta)d(cos(\theta)) \tag{5.6}$$

(4)The linear depolarization ratio:

$$\delta(\theta) = \frac{P_{11}(\theta)-P_{22}(\theta)}{P_{11}(\theta)+2P_{12}(\theta)+P_{22}(\theta)} \times 100\% \tag{5.7}$$

In this study, single-scattering property calculations are performed at multiple wavelengths including $440nm$, $500nm$, $532nm$, $550nm$, $675nm$, $870nm$, $1020nm$, and $1064nm$. The refractive indices of black carbon and the mineral dust particle are those suggested by Chang and Charalampopoulos [108] and Wagner et al. [109], respectively.

5.2 Single-Scattering Properties

5.2.1 Properties Without Angular Dependence

The mass absorption coefficient (MAC) is important for evaluating the radiative forcing of black carbon because of its high value at visible wavelengths. Figure 5.4 shows the simulated MACs of the cases listed in Table 5.1 in comparison with the values from other simulation studies and in-situ measurements at the specific wavelength of $550nm$. For the calculations, a density of $1.8g/cm^3$ is assumed for soot particles. The range of MAC values is around $5.0m^2/g$ to $5.5m^2/g$, which is in reasonable agreement with other studies. These results suggest that different cases of the model selected from Table 1 produce similar MAC values. For the wavelength range from $440nm$ to $675nm$, the absorption and extinction Angstrom exponents are 1.15 ± 0.11 and 1.45 ± 0.13, respectively.

In the case of external mixing with soot, the single-scattering properties of different particles are additive because their light scattering events can be treated independently. On the other hand, when the two components are attached to each other, their combined optical properties are no longer a direct sum. The computation of the bulk scattering properties therefore requires the knowledge of the single-scattering properties of dust-soot aggregates. Figure 5.4 displays the spectral MSCs of pure dust and dust-soot aggregates with parameters listed in Table 5.2. The MSCs of both pure dust and the dust-soot aggregates exhibit a strong wavelength-dependency, especially for the cases with particle size of $1.0\mu m$. As indicated by Figure 5.5, the semi-external mixing by black carbon significantly alters the absorptivity of the dust aerosol. The single-scattering albedos and asymmetry

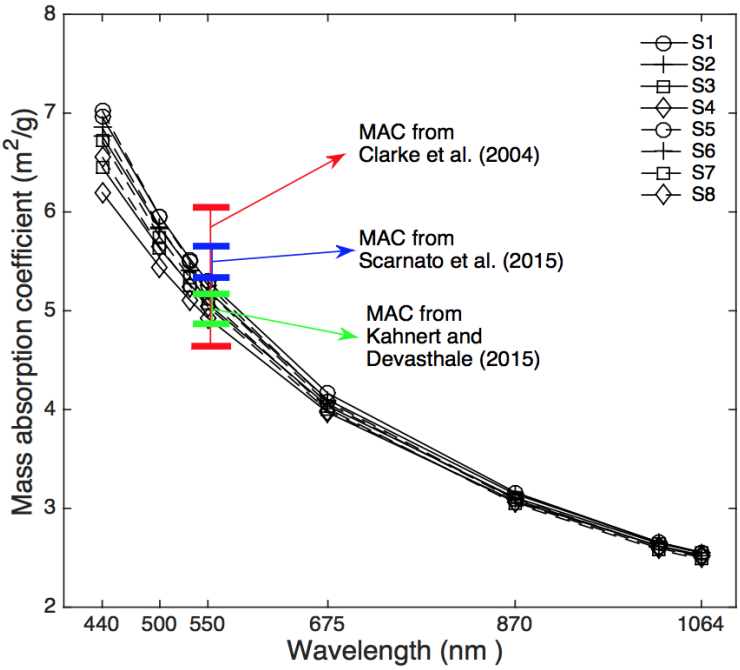

Figure 5.4: Simulated spectral mass absorption coefficients and extinction coefficients for the cases listed in Table 5.1

factors of all cases of mineral dust and soot particles (Table 5.1 & 5.2) can be summarized as follows: for soot particles, the asymmetry factor exhibits a strong wavelength dependence, ranging from 0.1 to 0.8, and their single-scattering albedo ranges from 0.1 to 0.4. For dust particles, the asymmetry factors of all cases are within the range of 0.67 to 0.8, and the semi-external mixing leads to a reduction of the albedo from 0.9 to 0.8. These results indicate a large variability of the bulk scattering properties of soot-laden mineral dust aerosols.

5.2.2 Properties With Angular Dependence

Accurately modeling the angular distribution of scattered intensity or polarization benefits the retrieval of important microphysical and optical properties, such as the effec-

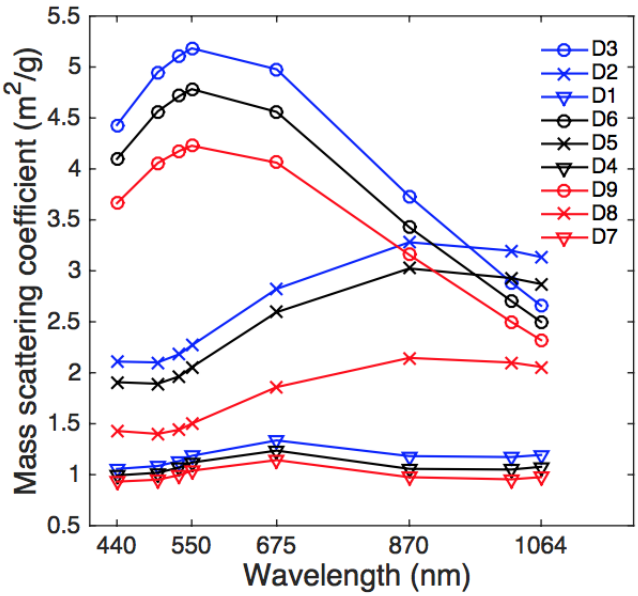

Figure 5.5: Simulated spectral scattering and absorption mass coefficients of dust/dust-soot aggregation at wavelengths from $440nm$ to $1064nm$

tive particle size and optical depth of mineral dust aerosols on a large scale. The first-generation random Koch fractal can reproduce the laboratory-measured scattering phase matrix of feldspar sufficiently well [110], as shown in Figure 5.6. The measured data are from the Amsterdam light scattering database [111], which provides an effective size of $1.0\mu m$, particle size distribution and refractive index of $1.50 + 0.001i$ for the simulations at wavelength $441.6nm$. The comparison demonstrates that the fractal polyhedral model captures the angular distribution pattern of intensity and polarization well. Spheroidal particle models may also be able to reproduce the measurement results, but multiple aspect ratios are often required to be mixed.

The most characteristic effect of the mixing of black carbon with mineral dust is the enhancement of the absorption efficiency. External mixing generally leads to weaker ab-

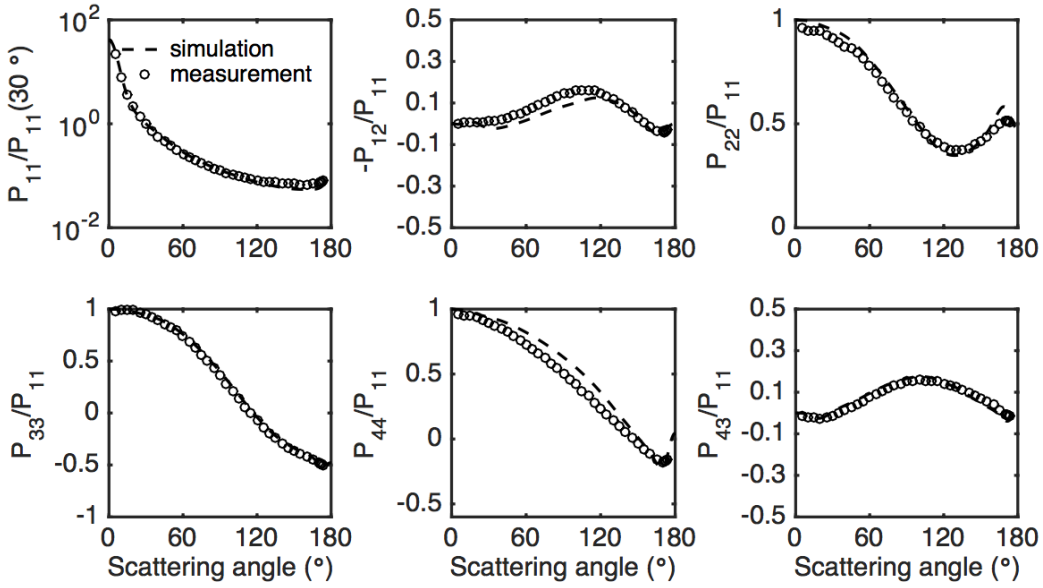

Figure 5.6: Comparison between the simulated and laboratory-measured scattering phase matrix of mineral dust aerosols.

sorption than semi-external mixing due to a lower degree of agglomeration of soot. Figure 5.7 shows the scattering phase matrix elements of the three possible soot-mineral dust configurations in a polluted dust layer. The properties of the pure soot are the average of cases listed in Table 5.1. Both the pure dust and the dust-soot aggregate have a particle size of $800nm$ in radius, while the latter has 5.8% of the volume of attached soot. The result displays the changes induced by the attachment of soot on the scattering phase matrix. In particular, the degree of linear polarization $-P_{12}/P_{11}$ of an aggregate is slightly higher than pure dust, and P_{22}/P_{11} gets closer to unity at the backward scattering angles, indicating that the aggregate behaves more similarly to a spherical particle than the pure dust. These changes seem to be modest at first glance, but the scattering cross-section has been drastically reduced.

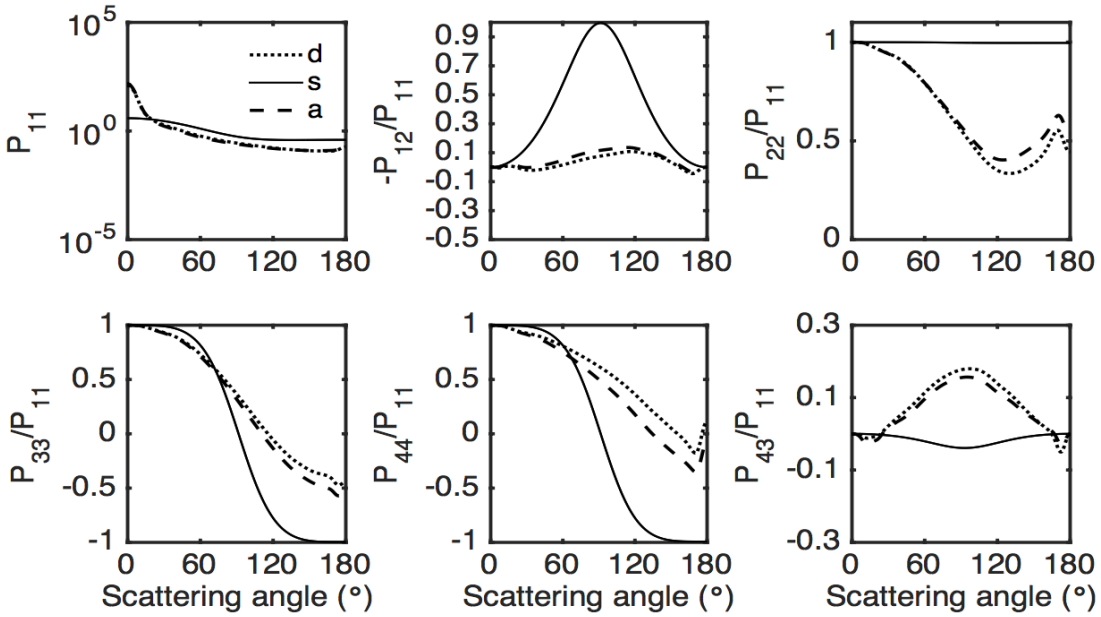

Figure 5.7: Scattering phase matrices of each possible component of a polluted dust aerosol. "d" denotes pure dust, "s" denotes pure soot, and "a" denotes dust-soot aggregate.

5.3 Parameterization

Conventionally, the effective bulk properties of the mixed aerosol can be computed using the effective medium approximation. In the effective medium approximation, the number of aerosol components reduces to one effective component, and the effect of mixing can be characterized by a volume-mixing ratio. Alternatively, one could first compute the single-scattering properties of each possible component, and parameterize the bulk properties according to their number density weights. The preceding analysis suggests that semi-external mixing yields the single-scattering properties quite different from the external-mixing counterparts. This warrants the introduction of dust-soot agglomerates as a class distinct from pure dust and pure soot. Below we present a method to properly parameterize the bulk optical properties of the dust-soot mixed aerosol.

The mixing state can be characterized by the number density weight of each component, denoted as

$$\mathbf{S} = (w_d, w_s, w_a)^T \tag{5.8}$$

The subscripts "d", "s", and "a" denote the parameters associated with pure dust, soot, and their aggregates, respectively. The sum of the weights equals to the unity,

$$w_d + w_s + w_a = 1 \tag{5.9}$$

A special case, the state of pure dust can be represented by

$$\mathbf{S_o} = (1, 0, 0)^T \tag{5.10}$$

The component of the dust-soot aggregate is characterized by so-called the aggregation ratio, i.e. the volume of the aggregated soot divided by the volume of the host dust particle,

$$\beta = \frac{V_{aggregated\_soot}}{V_{host\_dust}} \tag{5.11}$$

where β should be considered as an effective parameter of all dust-soot aggregates. For instance, if it is a function of particle size, then

$$\beta = \frac{\int_{r_{max}}^{r_{min}} (\frac{4}{3}\pi r^3) \frac{\beta_o(r)}{\beta_o(r)+1} \frac{dN_a}{dr}(r) dr}{\int_{r_{max}}^{r_{min}} (\frac{4}{3}\pi r^3) \frac{1}{\beta_o(r)+1} \frac{dN_a}{dr}(r) dr} \tag{5.12}$$

where $N_a(r)$ is the total number of dust-soot aggregates with particle size up to r, $\beta_o(r)$ is the aggregation ratio of particle with size r, and r_{min} and r_{max} are the maximum and minimum size of the aggregates. The aggregation ratio describes how much soot is attached to a unit volume of dust for the aggregates. If the aggregation ratio goes to zero, the mixed aerosol reduces to simply two components, i.e. pure dust, and pure soot. The

introduction of this parameter therefore becomes necessary when the semi-external mixing effects are to be evaluated.

Once the effective aggregation ratio β is known, another two effective parameters of the bulk, namely the total volume mixing ratio γ together with the degree of aggregation η , can be used to characterize the mixing state

$$\gamma = \frac{w_s V_s + w_a V_d \beta}{w_a V_d + w_d V_d} \tag{5.13}$$

$$\eta = \frac{w_a V_d \beta}{w_s V_s + w_d V_d \beta} \tag{5.14}$$

where V_s and V_d are the effective particle volumes of pure soot and clean dust before the mixing. The total volume mixing ratio γ is the volume ratio of soot to dust without specifying the ways of their mixing. The degree of adhesion η is the volumetric proportion of the attached soot to all mixed soot. γ can be viewed as an index of the total effect of the soot mixing, while η can be viewed as an index of the semi-external mixing effect.

Eq. (5.9), Eq. (5.13) and Eq. (5.14) together lead to a parameterization of the mixing state,

$$\mathbf{S} = \mathbf{F}^{-1}(\gamma, \beta, \eta)\mathbf{S_0} \tag{5.15}$$

where $\mathbf{F}$ is

$$\mathbf{F}(\gamma, \beta, \eta) = \begin{pmatrix} 1 & 1 & 1 \\ \gamma V_d & -V_s & (\gamma - \beta) V_d \\ 0 & \eta V_s & (\eta - 1)\beta V_d \end{pmatrix} \tag{5.16}$$

The single-scattering properties of the mixture layer of aerosol can then be obtained

by the following dot products,

$$\sigma_p = \sigma \cdot (\mathbf{F}^{-1}\mathbf{S}_0) \tag{5.17}$$

$$\alpha_p = \alpha \cdot (\mathbf{F}^{-1}\mathbf{S}_0) \tag{5.18}$$

$$\sigma_p \mathbf{P}_p(\theta) = \mathbf{P}(\theta) \cdot (\mathbf{F}^{-1}\mathbf{S}_0) \tag{5.19}$$

where the subscript "p" denotes the parameterized bulk properties. The three vectors are called component vectors, formed by the effective scattering properties of each component,

$$\sigma = (\sigma_d, \sigma_s, \sigma_a) \tag{5.20}$$

$$\alpha = (\alpha_d, \alpha_s, \alpha_a) \tag{5.21}$$

$$\mathbf{P}(\theta) = (\mathbf{P}_d(\theta)\sigma_d, \mathbf{P}_s(\theta)\sigma_s, \mathbf{P}_a(\theta)\sigma_a) \tag{5.22}$$

The above equations provide a set of single scattering properties labeled by three parameters, namely the total volume mixing ratio γ, aggregation ratio β, and the degree of adhesion η. The aggregation ratio β is assumed to be inherent to aerosol types. Figure 5.8 and Figure 5.9 show the parameterization sensitivity for the single-scattering albedo (as a scattering property without angular dependence), and the linear depolarization ratio (as a property with angular dependence) at 180 degree, respectively. The aggregation ratio is fixed at 5.8%. The effective size of the pure dust and aggregate is $1.0\mu m$, and the effective size of soot is around $0.1\mu m$. The figures clearly demonstrate how different ways of mixing, i.e. externally or semi-externally, change the bulk scattering properties of soot-laden dust aerosol.

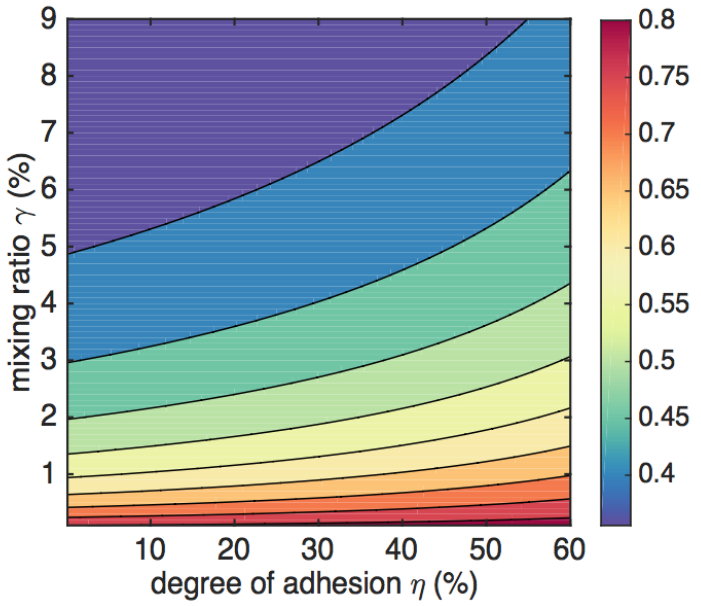

Figure 5.8: The parameterized single-scattering albedo of the bulk.

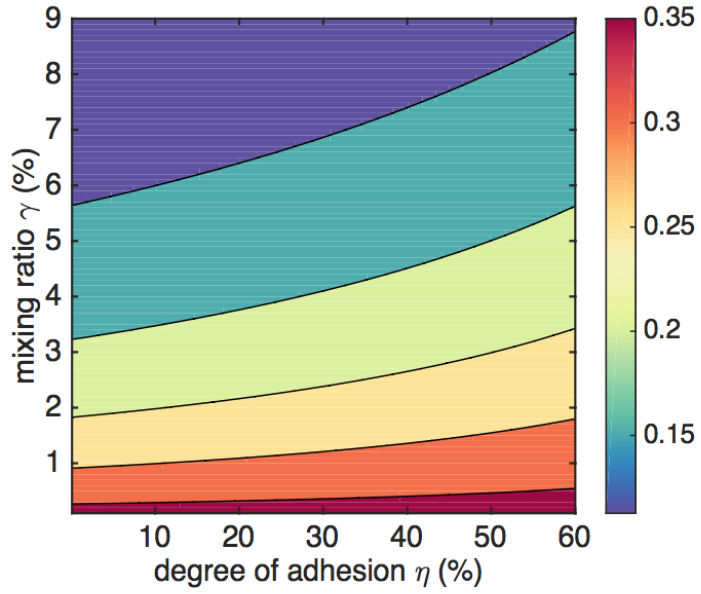

Figure 5.9: Parameterized linear depolarization ratio at 180 degree.

5.4 Multiple Scattering Properties and Analysis

5.4.1 Labeled Polarized Reflectivity

This section discusses the multiple scattering properties of the soot-contaminated dust aerosol by solving the radiative transfer equation with proper boundary conditions. The adding- doubling method [112]is applied for this purpose. In the multiple scattering calculations an idealized plane-parallel atmosphere with a single homogeneous aerosol layer and terminated by a Lambertian surface of albedo 0.1 is assumed. Using the parameterization introduced in previous section, we can label the RTE as follow,

$$\begin{aligned} &\mu \tfrac{\mathrm{d}}{\mathrm{d}z}\mathbf{I}(z,\Omega) = (\alpha_p(z)+\sigma_p(z))_{\gamma,\eta}\mathbf{I}(z,\Omega) \\ &-\tfrac{\omega_p(z)}{4\pi}(\alpha_p(z)+\sigma_p(z))_{\gamma,\eta}\int(\mathbf{M}_p(z,\Omega,\Omega'))_{\gamma,\eta}\mathbf{I}(z,\Omega')\mathrm{d}\Omega' \end{aligned} \tag{5.23}$$

Consequently, the polarized reflectivity, as a solution to the RTE can be labeled as,

$$\mu_o R_{ij}(\Omega,\Omega_0) = Sol[RTE_{\gamma,\eta}] \tag{5.24}$$

where "Sol" denotes the solving operation for the polarized reflectivity. We first compute the polarized reflectivity with five cases listed in Table 5.3. Figure 5.10 shows the polar plots of Stokes vector component or their ratios, I, $-Q/I$, U/I as a function of viewing direction in these five cases. The optical depth and effective particle size of dust are 0.60 and $0.80\mu m$, respectively. The solar zenith angle is 45 degree. In each polar plot, the radius is the viewing zenith angle, the angle is the relative azimuthal angle, and the color represents the values of the component. To show the contour lines more clearly, the axes of the plots are displayed separately. The plot in the middle displays the pattern associated with pure dust, while the other surrounding plots show the pattern associated with the soot-laden dust. It is clear that the intensity patterns are fairly similar among these five

cases, whereas the polarization patterns are quite distinguishable.

Case	γ	η
E0	0%	0%
E1	2%	0%
E2	4.5%	0%
E3	2%	50 %
E4	4.5%	50%

Table 5.3: The labels used for the RTE solutions.

5.4.2 Analysis

An analysis scheme is introduced to quantify the uncertainties of the multiple scattering properties due to the uncertainty on the aerosol mixing states. In accordance with observations [42, 43, 47, 48], the amount of mixed soot, compared to mineral dust, is much smaller. Presumably, the interaction with black carbon plays a secondary role in determining the aerosols multiple scattering properties. Here the way of their mixing is treated as a source of uncertainty for modeling the multiple scattering properties. Under idealized conditions, the polarized reflectivity observed by a multiple-angle airborne satellite, can be viewed as a function of viewing direction, optical depth, particle size, and the mixing state:

$$\mu_o R_{ij} = f(\Omega, \tau, r_d, \gamma, \eta) \tag{5.25}$$

where τ is the optical thickness of the aerosol, r_d is effective particle size of pure dust, $\Omega = (\mu, \phi)$ is the viewing direction in a spherical coordinate system, R_{ij} could be associated with any of the four components of the Stokes vector. It should be noted that the idealized condition is confined to the situation where the solar incidental direction is

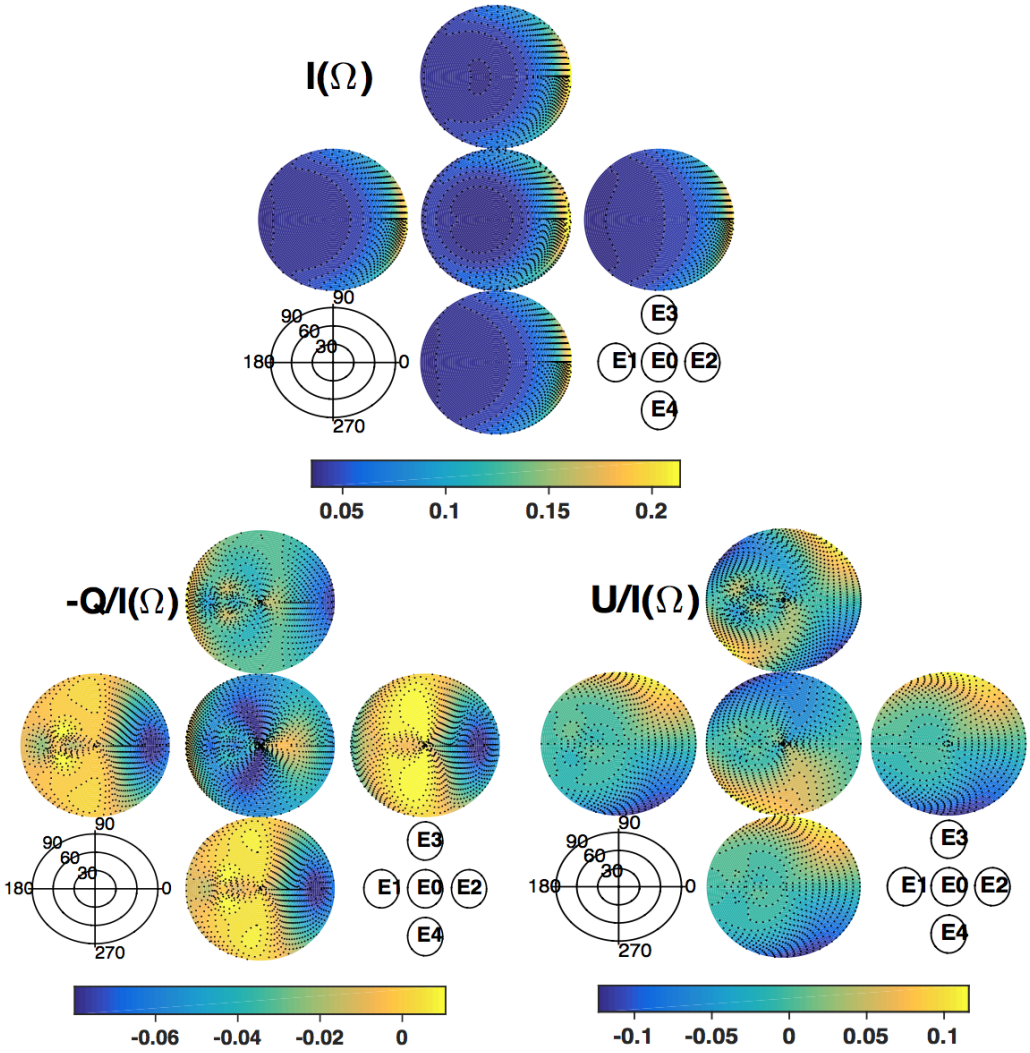

Figure 5.10: The polar plot of I, $-Q/I$, U/I as a function of view angle for labels listed in Table 5.3.

fixed, and the variability of soot particle size r_s and the aggregation ratio β are small. On the other hand, if we ignore the aerosol's mixing effects, the reflectivity reduces to

$$\mu_o {R_{ij}}^o = f_o(\Omega, \tau, r_d) = f(\Omega, \tau, r_d, 0, 0) \tag{5.26}$$

The forward modeling deviation can be defined as the difference between the two

functions integrated over an observational range of an instrument,

$$D(\gamma,\eta)=\frac{1}{\Delta\Omega'}\iint|\frac{f_o(\Omega',\tau_o,r_d^o)-f(\Omega',\tau_o,r_d^o,\gamma,\eta)}{f_o(\Omega',\tau_o,r_d^o)}|d\Omega'\times 100\% \tag{5.27}$$

It should be noted that here the parameter pair $(\tau,r_d)=(\tau_o,r_d^o)$ is now constant, referred to as the standing point. Furthermore, in accordance with the instruments, the viewing direction is confined to

$$\Omega'\in\Omega_{\max} \tag{5.28}$$

where $\mathbf{M}_{max}$ is the maximum satellite observational range. For instance, the MISR-type instruments has a maximum observation range so that the scattering angle is confined to 82^o to 148^o , meaning that all viewing directions within this range constitute its maximum observational range. If the observational range is discretized into a finite number of directions with equal weightings, the above equation becomes

$$D(\gamma,\eta)=\frac{1}{N}\sum_{k=1}^{N}|\frac{f_o(\Omega^k,\tau_o,r_d^o)-f(\Omega^k,\tau_o,r_d^o,\gamma,\eta)}{f_o(\Omega^k,\tau_o,r_d^o)}|\times 100\% \tag{5.29}$$

The value of this function can be computed when a standing point $(\tau_o,r_d^o)$and the satellite observational range $\mathbf{M}_{max}$ are specified. As we already mentioned, the functions f and f_o can be either associated with intensity or polarization. Therefore, the deviation function defined above could be either associated with intensity or the degree of polarization.

The deviation function at a specific standing point and observational range is associated with the forward modeling process, i.e. the theoretical observations by the satellite instruments. Given certain probability distribution of (γ,η), one can compute the average, minimum, and maximum deviations from the pure dusts on the polarized reflectivity. Figure 5.11 shows a contour plot of $D(\gamma,\eta)$ associated with the intensity component, and

Figure 12 shows the $D(\gamma, \eta)$ associated with the degree of linear polarization. From the two figures, it can be seen that the intensity deviation can go up to 60% when the total mixing ratio is around 3% to 5%, while the deviation on the linear polarization can go up to 150%. These results suggest that 1) the labeled multiple scattering properties have a similar pattern to those of the single- scattering properties; 2) compared to radiance intensity, much larger uncertainties are observed for the degree of linear polarization.

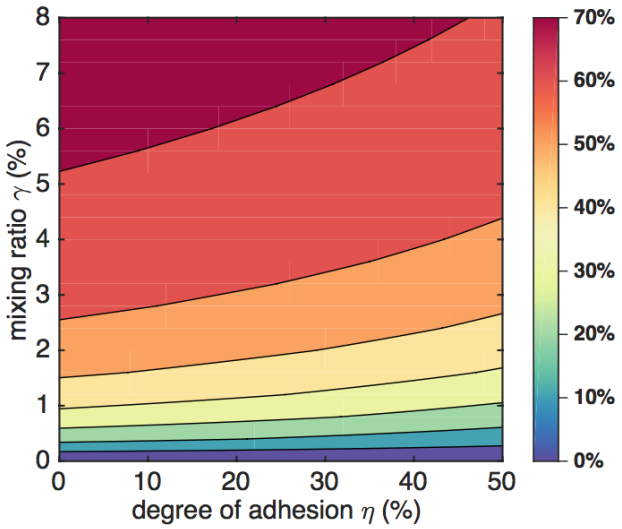

Figure 5.11: Deviation function $D(\gamma, \eta)$ associated with the radiance intensity. The standing point for this computation is $(1.0, 0.8\mu m)$, meanwhile 7485 viewing directions with scattering angle ranging from 82^o to 148^o are used.

On other hand, it is also desirable to quantify the uncertainties in the retrieval process. Similar to the deviation function, we can introduce the following the so-called criterion function as

$$C(\tau, r_d) = \frac{1}{\Delta\Omega'} \iint \left| \frac{f_o(\Omega', \tau, r_d) - f(\Omega', \tilde{\tau}, \tilde{r}_d, \gamma_o, \eta_o)}{f_o(\Omega', \tau, r_d)} \right| d\Omega' \times 100\% \tag{5.30}$$

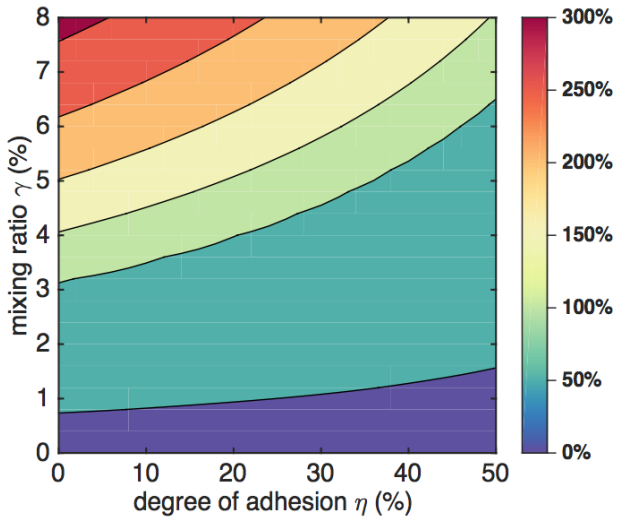

Figure 5.12: The deviation function $D(\gamma, \eta)$ associated with the degree of linear polarization. The parameters used are the same as used in Figure 5.11

Note that here two pairs of parameters $(\tilde{\tau}, \tilde{r}_d)$ and (γ_o, η_o) are constant. Now the two functions f_o and f can be interpreted in different ways. $f_o(\Omega', \tau, r_d)$ can be viewed as the quantities associated with the standard models in the retrieval process, whereas $f(\Omega', \tilde{\tau}, \tilde{r}_d, \gamma_o, \eta_o)$ can be viewed as the quantities associated with a quasi-realistic models. When $C(\tau, r_d)$ becomes small enough, the model fits well with the observation, we then call it a retrieval event, and the fulfilled parameters (τ, r_d) are called retrieved parameters. Since $f(\Omega', \tilde{\tau}, \tilde{r}_d, \gamma_o, \eta_o)$ is associated with the quasi-realistic model, the constant parameters $(\tilde{\tau}, \tilde{r}_d)$ are referred to as goal parameters, and (γ_o, η_o) are referred to as confusion parameters. Because satellite observation is always limited to a limited number of viewing angles at a specific time and location, it is not able to reach its maximum observation range for a particular layer of mineral dust. Thus, the integration range for the criterion function must be a small subset of the maximum observational range, i.e.,

$$\Omega' \in \Omega \subset \Omega_{\max} \tag{5.31}$$

Again, if the integration range is discretized into a finite number of directions, then the criterion function becomes

$$C(\tau, r_d) = \frac{1}{M} \sum_{k=1}^{M} \left| \frac{f_o(\Omega^k, \tau, r_d) - f(\Omega^k, \tilde{\tau}, \tilde{r}_d, \gamma_o, \eta_o)}{f_o(\Omega^k, \tau, r_d)} \right| \times 100\% \tag{5.32}$$

Accordingly the number of directions M is much smaller than N ,

$$M << N \tag{5.33}$$

We then can introduce the following criteria using $C(\tau, r_d)$:

(A). When f_o or $f \equiv I$, and $C_A(\tau, r_d) \leq 1\%$, namely the intensity criterion;

(B). When f_o or $f \equiv \sqrt{Q^2 + U^2}/I$, and $C_B(\tau, r_d) \leq 1\%$, namely, the polarization criterion;

(C). $C_C(\tau, r_d) = C_A(\tau, r_d) \times C_B(\tau, r_d) \leq 1\%$, namely, the intensity plus polarization criterion;

Given a set of goal parameters, under the "confusion" of the confusion parameters, it can be retrieved by applying the above three criteria. The retrieval quality can then be accessed. Figure.5.13 displays the fulfilled parameter range for the intensity, polarization and intensity plus polarization criterion. For all three criteria, the local minimum of the criterion function for two polluted cases (denoted by blue and red colors) can differ largely from the goal parameter. For example, for the goal parameters $(\tau_o, {r_d}^o) = (0.6, 0.4\mu m)$, the retrieved parameter would be around $(0.4, 0.7\mu m)$ using the intensity criterion and a confusion parameter $(\gamma_o, \eta_o) = (3\%, 100\%)$. Such results suggest that by using a pure dust look-up table to infer the optical thickness and particle size of the polluted dust aerosol, the retrieved values might differ largely from the true values. However, noting that if more complex retrieval methods are used, the quality of the retrieval needs to be reevaluated.

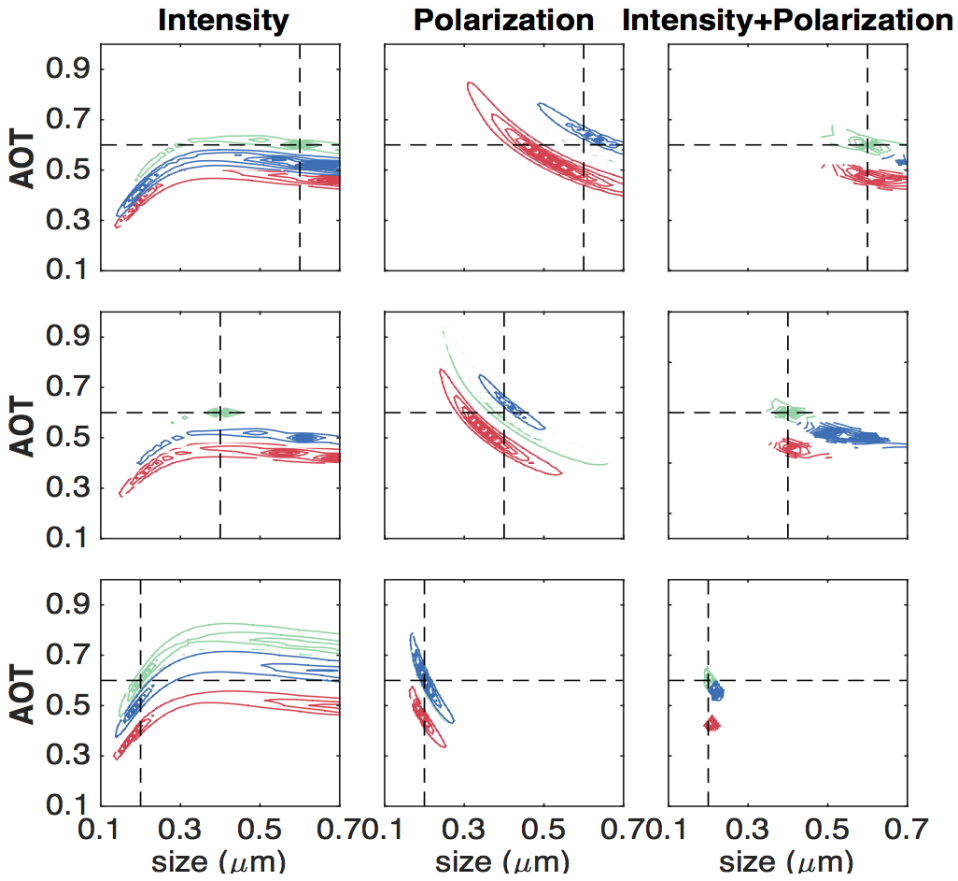

Figure 5.13: Simulated retrieval of particle size and optical thickness of the dust aerosols. The green color lines denote the fulfilled range associated with confusion parameters $(\gamma_o, \eta_o) = (0\%, 0\%)$, meaning the standard model perfectly matches the quasi-realistic model. The blue color lines denote the fulfilled range with confusion parameters $(\gamma_o, \eta_o) = (3\%, 0\%)$, while the red color is associated with the confusion parameters $(\gamma_o, \eta_o) = (3\%, 100\%)$. Nine viewing directions are used in the computation

5.5 Conclusions

Accurately modeling the single and multiple scattering properties of mineral dust particles is a challenging task because of their irregular shapes, complex compositions and interactions with other aerosols. As an effort towards a more realistic modeling, more parameters should be taken into account in accordance with the observations. This study

investigates the effect of soot mixing on the single-scattering characteristics as well as the uncertainties caused by this factor in the multiple scattering modeling. In the single-scattering modeling, the parameters of the models are carefully selected, such that the applied models reasonably capture the characteristic scattering properties of the dust and soot particles. The introduced parameterization scheme quantitatively maps the mixing state to bulk single-scattering properties of aerosol. In the multiple-scattering modeling, the polarized reflectivity is viewed as not only a function of optical depth and particle size, but also the mixing states of the aerosol under the assumed setups. The results of the deviation function and criterion function indicate that large uncertainty may be introduced by ignoring the state of mixing of soot on both forward and inverse modeling on the polarized reflectivity of mineral dust.

6. MODELING THE REFLECTION AND TRANSMISSION PROPERTIES OF A DYNAMIC OCEAN SURFACE

In this chapter, we first introduce the construction of the ocean surface in accordance with the ocean wave spectra. Next, we introduce the Monte-Carlo radiative transfer model for simulating the reflection and transmission properties of a dynamic ocean surface. The results and discussion will focus on the temporal fluctuation of the reflected and transmitted irradiance and the wind-induced vertical energy variation.

6.1 Description of the Model and Properties of Interests

6.1.1 Ocean Surface Construction

This section provides a description on the ocean surface generation. Capturing the elevation and slope statistics of the ocean surface is the key for an ocean surface construction, since these statistical properties determine the reflection and transmission of light. The basic ideas for ocean surface construction are: (a) the ocean surface is viewed as a superposition of 2-D sinusoidal wave with different frequencies and amplitudes; (b) accordingly, the surface elevation can be constructed by the inverse Fourier transform of the 2-D randomly generated amplitudes. However, the amplitudes for various frequencies must satisfy some physical statistics associated with the energy of the ocean waves on the frequency domain. In other words, the construction of the ocean surface from a random process is meaningful only if we sample the amplitude in accordance with the variance spectra of the ocean wave. In this study, we apply the variance spectral density function proposed by Elfouhaily et al.[113], i.e.,

$$\Psi_{1s}(k,\varphi) = \frac{1}{k} S(k)\Phi(k,\varphi) \tag{6.1}$$

where (k, φ) are the polar coordinates, $\Psi_{1s}(k, \varphi)$ is the so-called one-sided variance spectra, $S(k)$is the omnidirectional spectral density, and $\Phi(k, \varphi)$ is the non-dimensional spreading functions, which has the following form [114],

$$\Phi(k, \varphi) = C(s)[\cos^{2s}(\varphi/2)] \tag{6.2}$$

where $C(s)$ is the normalization constant as a function of s , and s is a function of k . The detailed form of variance spectra is given in Elfouhaily et al. [113]. With the above variance spectra, one can write out the random amplitudes that match the statistics of the wave variance spectra. According to Tessendorf [115], the explicit formula for generating the random amplitudes is,

$$\hat{z}_o(k_{xy}) \equiv \frac{1}{\sqrt{2}}[\rho(k_{xy}) + i\sigma(k_{xy})][\frac{\Psi_{1s}(k = k_{xy})}{2}\Delta k_x \Delta k_y]^{1/2} \tag{6.3}$$

where $\rho(k_{xy})$ and $\sigma(k_{xy})$ are two independent random real numbers with distribution of zero mean and unit variance generated at frequency of k_{xy} , Δk_x and Δk_y are the frequency intervals along x and y directions. With this form of amplitude, it can be shown that it is consistent with the chosen variance spectra[116] . But direct application of the inverse Fourier transform operation to the above amplitude would not generate real numbers for the heights of the ocean waves, simply because the $\hat{z}_o(k_{xy})$ is not Hermitian.

In order to make the amplitude Hermitian and varies with time, the following amplitude is used [115],

$$\hat{z}(k_{xy}, t) \equiv \frac{1}{\sqrt{2}}[\hat{z}_o(+k_{xy}) \exp(-i\omega_{xy}t) + \hat{z}_o^*(-k_{xy}) \exp(+i\omega_{xy}t)] \tag{6.4}$$

With above amplitudes generated for various frequencies, one can obtain ocean surface high by the inverse Fourier transform,

$$z(x, y, t) = FT_{2D}^{-1}(\hat{z}(k_{xy}, t)) \tag{6.5}$$

As a function of wind speed, the variance spectra represent the energy density of the ocean wave over the frequency domain. It is therefore expected that for the same wind speed, the generated ocean surfaces are similar and would have similar reflection and transmission properties. Figure 6.1 displays the constructed ocean surface at the wind speed of 10 m/s by applying above procedures.

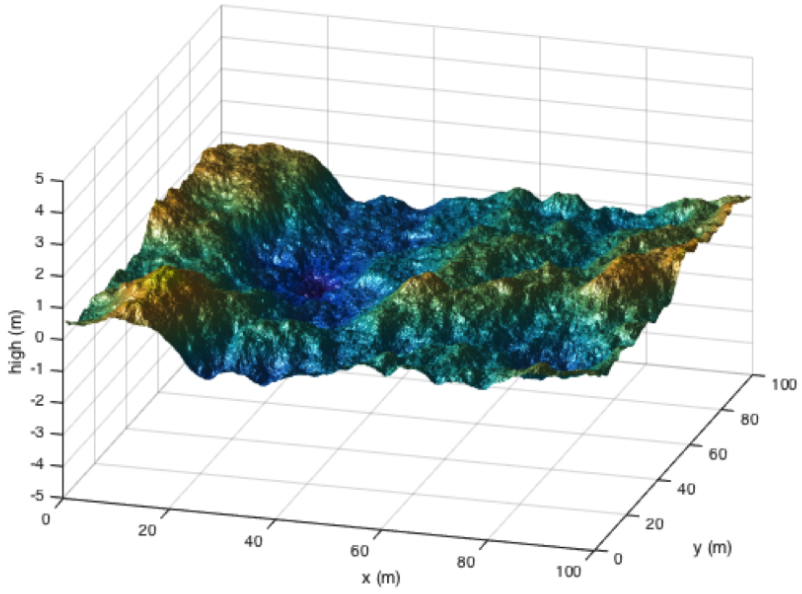

Figure 6.1: Ocean surface wave constructed using Fourier transform technique in accordance with the wave variance spectra at wind speed of 10 m/s.

6.1.2 A Monte-Carlo Radiative Transfer Model

A Monte-Carlo radiative transfer code is developed to simulate the reflection and transmission properties for an air-sea interface layer. This model applies the ray-tracing algo-

rithm proposed by Mobley [116] for the randomly faceted ocean surface. This model incorporates the scattering processes of photons in the water or in the air, in addition to the reflection and transmission of the photons, such that we are able to simulate the polarized reflected light field or transmitted light field for an air-sea interface layer with a finite optical thickness and specific inherent optical properties.

The Monte-Carlo model tracks the photons' paths and weights until the photons are out of the layer. The ocean surface wave facets are represented in Cartesian coordinate system, while the directions of photon paths are specified by the corresponding spherical coordinate (θ, ϕ) . The value of zenith angle θ is determined with respect to $+z$ direction, while the value of azimuthal angle ϕ is determined with respect to $+x$ direction. To collect the outgoing photons, we discretize the upper hemisphere or lower hemisphere into different quads. The zenith angle is partitioned into 180 directions, while the azimuthal angle is partitioned into 360 directions. Figure 6.2 displays the discretized quads with azimuthal angle interval 1^o and zenith angle interval 1^o (the figure is scaled for better presentation). The radiation strength within a specific quad can be computed directly from the Monte-Carlo simulation, and it is the irradiance confined to the solid angle associated with the quad as followed,

$$I_{irad,quad} = \int_{quad} I_{rad} cos(\theta) d\Omega \tag{6.6}$$

where θ is the corresponding zenith angle of the quad, $I_{irad,quad}$ is the average radiance within the quad. The centers of the quads can be treated as the corresponding incident or outgoing directions of the photons. Accordingly, we can assign a direction to the irradiance within the quad.

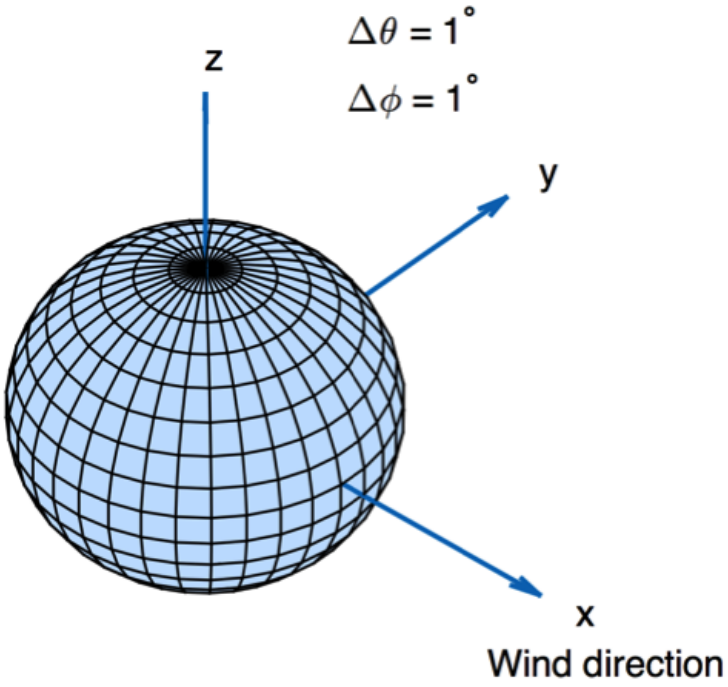

Figure 6.2: Coordinate system used for ocean surface and directions of the light beam propagations

Given an incident irradiance $I_{inc,quad}(\Omega_o)$ from the quad associated with direction Ω_o , the Monte Carlo model computes the outgoing irradiance $I(\Omega_f)$ propagating along Ω_f by tracking the photons until the photons are out of the medium. For a specific pair of incident and outgoing directions (Ω_o, Ω_f) , it is the following effective Mueller matrix to be computed from the model,

$$I_{out,quad}(\Omega_f) = M_e(\Omega_f, \Omega_o) I_{inc,quad}(\Omega_o) \tag{6.7}$$

The effective Mueller matrix can be obtained from a sequence of events encountered by the incident photons, including scatterings, reflections and transmissions, which can be expressed as

$$M_e(\Omega_f, \Omega_o) = R(\alpha_f)M_f(\Omega_f, \Omega_j)R(\alpha_{f,j})...R(\alpha_{2,1})M_1(\Omega_1, \Omega_o)R(\alpha_{1,o}) \tag{6.8}$$

where $M_j(\Omega_j, \Omega_{j-1})$ can be one of the reflection, transmission matrices and the scattering phase matrix (multiplied by the scattering albedo) associated with the scattering plane formed by (Ω_j, Ω_{j-1}) , $R(\alpha_{j,j-1})$ rotates $(j-1)th$ reference plane to jth reference plane, $\alpha_{j,j-1}$ is the corresponding rotation angle, and $R(\alpha_f)$ rotates the scattering plane to the final meridian plane. The above effective Mueller matrix is for the computation of irradiance, to compute the radiance, the effective Mueller matrix should be multiplied by the ratio of incident to outgoing solid angle as well as the ratios of the cosines of zenith angles, .i.e.,

$$I_{out,rad} = M_e(\Omega_i, \Omega_{out})(\frac{|u_i|}{|u_{out}|}\frac{\Omega_{i,solid}}{\Omega_{out,solid}})I_{in,rad} \tag{6.9}$$

where $I_{out,rad}$ and $I_{in,rad}$ denote the outgoing and incident radiance respectively, Ω_i is the effective Mueller matrix for irradiance with incident direction Ω_i and outgoing direction Ω_{out} , $|u_i|$ and $|u_{out}|$ are the absolute values of cosines of incident and outgoing zenith angles, $\Omega_{i,solid}$ is the solid angle associated with the incident beams, and $\Omega_{out,solid}$ is the solid angle associated with the outgoing beams.

Figure 6.3 is a schematic representation of the process of tracking each photon impinging into the air-sea interface. Specifically, the weights of the photons are initialized to be a unit 4 by 4 matrix with an selected incident direction. The photon will then be moved according to exponential decay law if they are available to be tracked. The algorithm then determines whether the tracking photon encounters a scattering or reflection and transmission event according to the photon's updated location. When a scattering

event happens, the future propagation direction will be randomly sampled according to the scattering properties of the medium. The sampling strategy is based on the method introduced in [117]. When the reflection and transmission happens, the directions and weights of the reflected and transmitted beams will be computed according to Fresnel reflection and transmission matrices. The reflected photon will be further tracked until it is out of the region, whereas the transmitted photon will be stored for future tracking. After all the stored photons have been tracked, the weights for each direction will be added. By repeating the above process for a large number of incident photons, one can obtain the statistical reflection and transmission properties for the layer. For the results presented in this study, the ocean surface is constructed with area of $100m \times 100m$ with its center at the origin of the coordinate system. For each simulation, the photons are initiated to strike near center of the ocean surface. If the photon reaches the boundary of the layer, it will be reinitiated at the same depth towards (or from) the center of the surface. The refractive index of the air and water are 1.31 and 1.0 respectively. The scattering properties of the air are computed from Rayleigh scattering theory, while the scattering properties of water are based on the hexahedral ensemble models introduced previously. In our discussion, a fixed incident zenith angle of 49.5^o is used, and the scattering albedo of the water is fixed at 0.4.

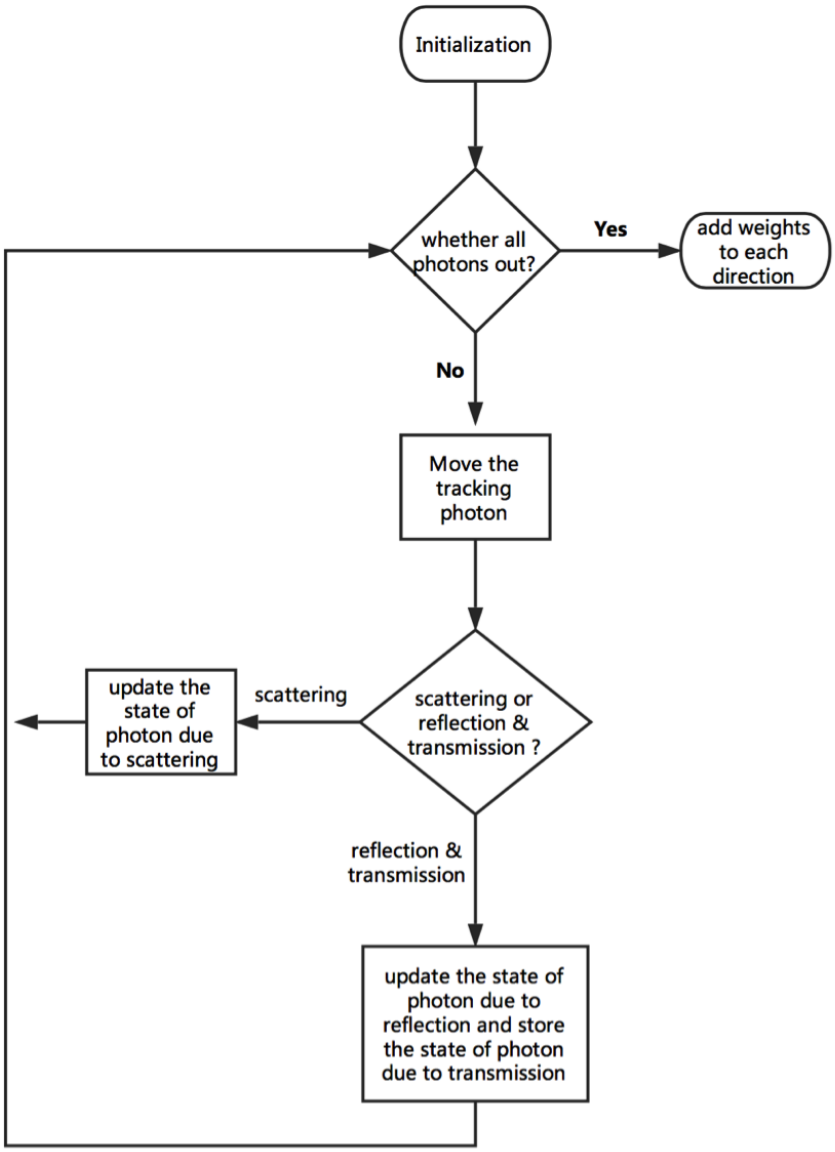

Figure 6.3: A schematic representation of the procedure for computing the reflection and transmission properties of air-sea interface layer.

6.1.3 Test of the Model

In principle, every construction of the air-sea interface is unique and has different reflection and transmission properties. In order to validate our model, we consider relatively

simple cases, i.e. the flat surface with relatively thin optical thickness. By applying to these simple cases, we can test whether the model tracks the path of the photon correctly and whether the intensity and polarization of the outgoing photon is correctly computed.

When a relatively thin layer near the air-sea interface is considered, the maximum transmitted irradiance of the layer can be approximated by the following expression,

$$I_{trans} = T(\theta_t) I_{inc}(\theta_i) \exp(-\tau_{water}/\cos(\theta_t)) \exp(-\tau_{air}/\cos(\theta_i)) \tag{6.10}$$

where $T(\theta_t)$ is the Fresnel transmission matrix with transmission angle θ_t , $I_{inc}(\theta_i)$ is the incident irradiance with incident angle θ_i , τ_{water} is the optical thickness of water and τ_{air} is the optical thickness of the air. And the reflected irradiance can be approximated as,

$$I_{ref} = R(\theta_i) I_{inc}(\theta_i) \exp(-2\tau_{air}/\cos(\theta_i)) \tag{6.11}$$

where $R(\theta_i)$ is the Fresnel reflection matrix with reflection angle θ_i . On the other hand, the Monte Carlo model can simulate these two quantities directly for the ocean surface with zero wind speed. When the incident angle and the optical thickness are relatively small, the analytical approximation for the reflected and transmitted irradiance should match well with our model simulations. A comparison between the approximated results and simulated results for the reflected and transmitted irradiances are displayed on Figure 6.3 and Figure 6.4. The results demonstrate that the developed Monte Carlo model is able to accurately simulate the reflection and transmission properties of an air-sea interface layer.

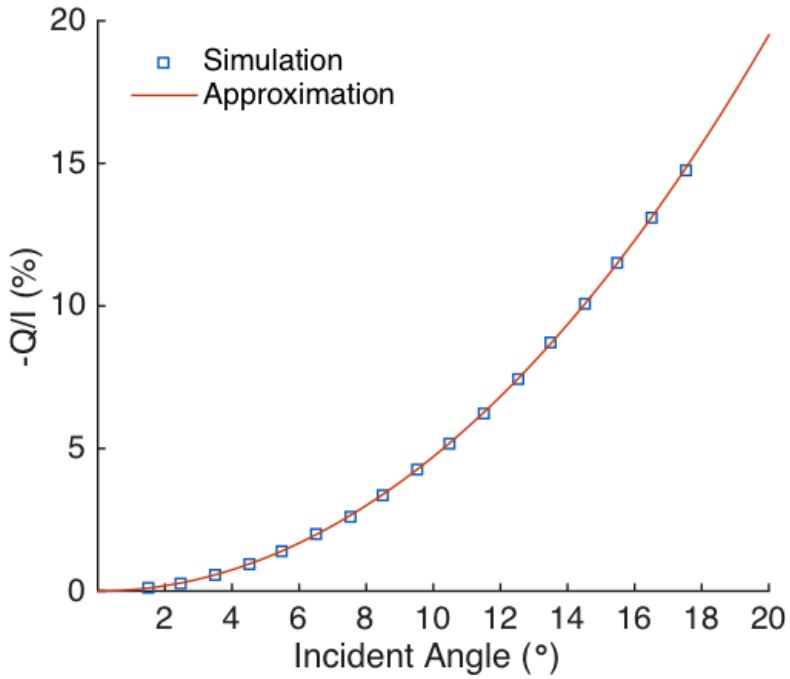

Figure 6.4: A comparison between the analytical approximation and the Monte Carlo simulation on the reflected $-Q/I$ associated with the irradiance. The layer is assumed to has an optical thickness 1.0 for the water and zero for air.

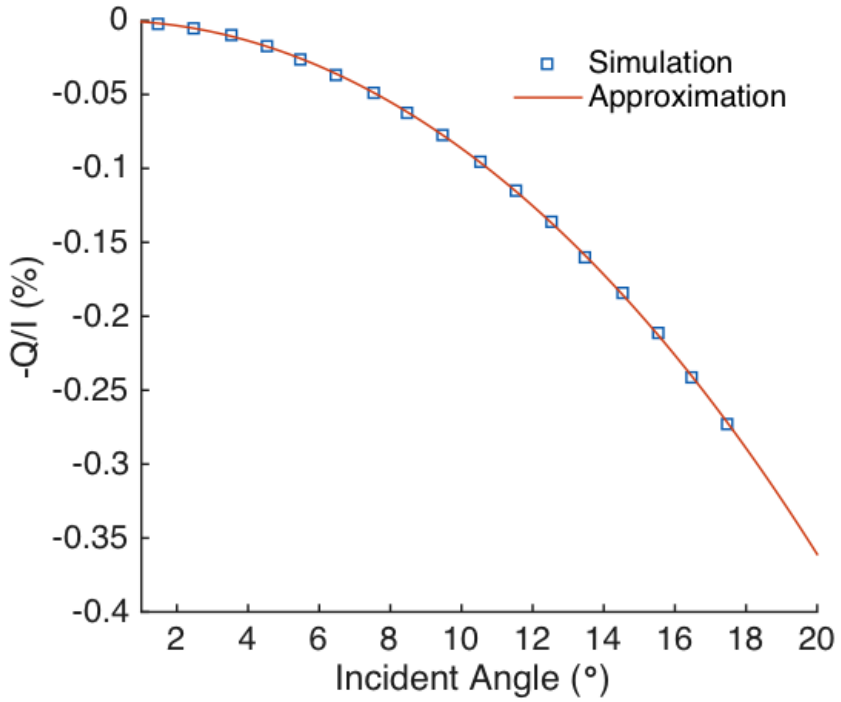

Figure 6.5: Same as Figure 6.4, except that the compared quantity is the transmitted counterpart.

6.2 Results and Discussions

6.2.1 Temporal Fluctuation of the Irradiance and Radiance

With the developed Monte Carlo model, one can compute the polarized reflection and transmission of an air-sea interface layer for a specific construction of the ocean waves. In this study, we mainly discuss the properties related to the dynamic aspect of ocean. Specifically, we focus on the reflected and transmitted irradiance for the dynamic ocean surface layer. It should be noted that the validity of our results is confined to a layer of medium containing the ocean surface and water with finite optical thickness, rather than the entire air-sea system with specific boundary conditions. The results can serve as an approximation to the case of a deep ocean with biases relating to the upwelling radiance

beneath the layer. As we've mentioned in the introduction, the dynamic ocean could potentially induce rapid fluctuations of reflected and transmitted light fields. The magnitude of the fluctuation can only be quantified using the dynamic ocean surface model, as introduced in last section. Figure 6.6 displays the snapshots for the ocean surface wave at three different time steps of 0.1s, 0.6s and 1.1s with wind speed of 10 m/s at 10 meters above the sea level. The surface is generated with a resolution of 1024×512 along x and y direction respectively, and therefore the shortest resolvable wavelength along direction is around 0.1953 m. As displayed in the figure, a small crest at around $x = 70m$ could turn into a trough within one second.

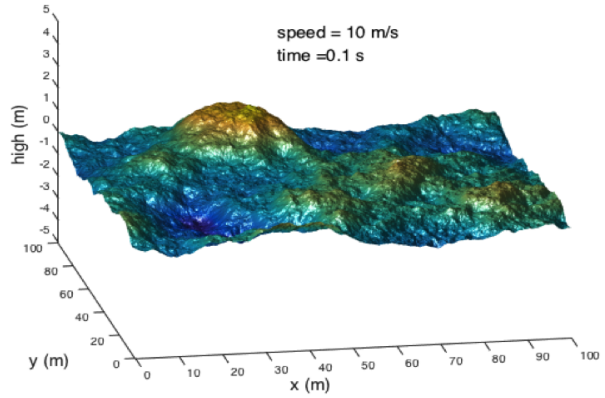

(a) The ocean surface at time =0.1 s, with wind speed of 10 m/s

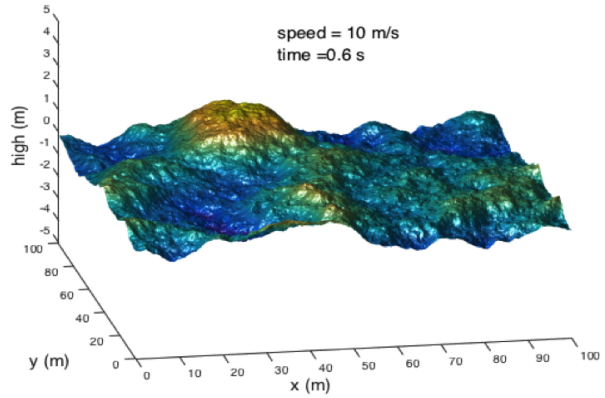

(b) The ocean surface at time =0.6 s.

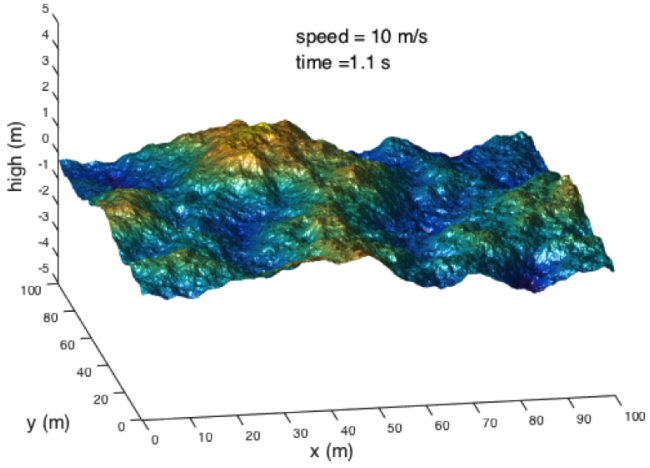

(c) The ocean surface at time =1.1 s

Figure 6.6: Snapshots for the dynamic ocean surface with wind speed of 10m/s

To simulate the light field fluctuation induced by the moving surface, we generate 20 seconds of the moving ocean surfaces with a resolution of 0.1 second, i.e. 200 sampled constructions at the wind speed of 14 m/s. To evaluate the change at different depth of ocean, we compute the reflection and transmission properties for the layer with optical thickness of 1, 3 and 5, which corresponds to depths around 6.6 m, 20 m, 33.3 m respectively with an extinction coefficient of $0.15m^{-1}$.

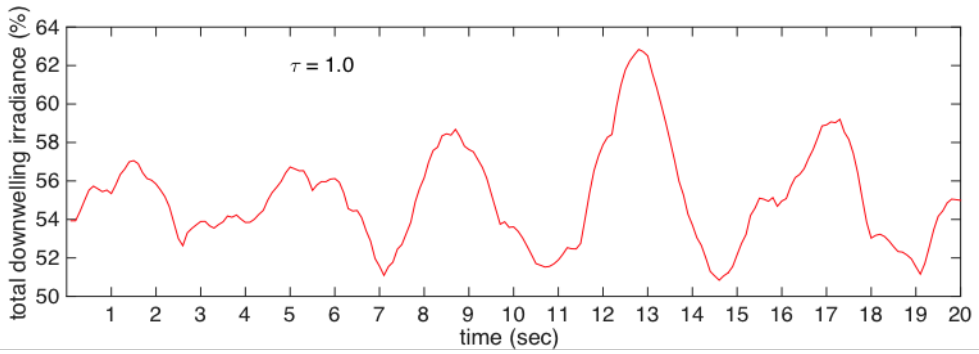

(a) For layer with optical thickness of 1.0.

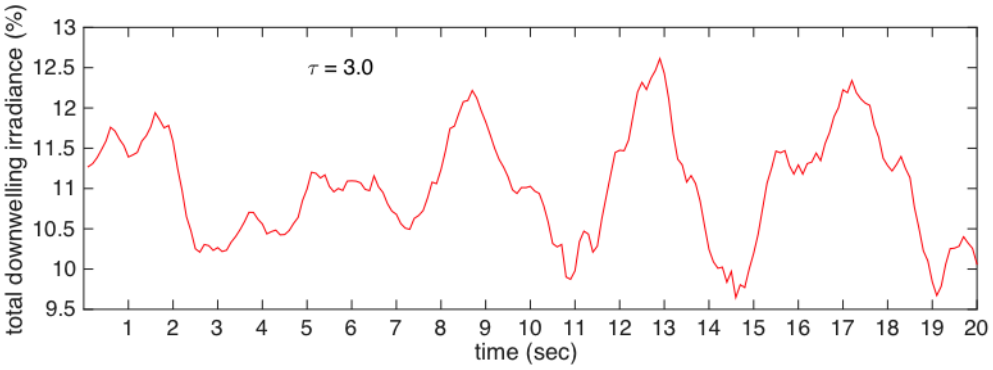

(b) For layer with optical thickness of 3.0.

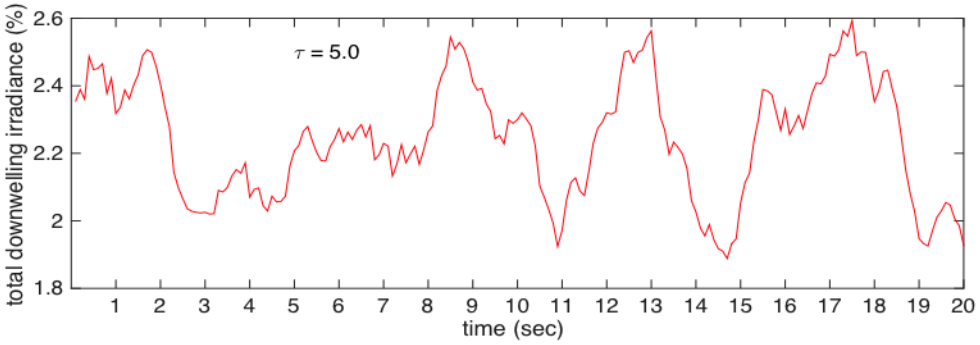

(c) For layer with optical thickness of 5.0.

Figure 6.7: The down welling irradiance for dynamic ocean layers with different optical thicknesses. The values are computed in terms of the percentage of the incident irradiance.

Figure 6.7 displays the simulated fluctuation for the total irradiance (in terms of the percentage of the incident irradiance) transmitted through the ocean as a function of time. For each time step, 100000 photons are used to simulate the light field. For different

optical depths, it is clear that the fluctuation patterns are similar due to the fact that this fluctuation is mainly induced by the ocean surface geometry. Due to the exponential decay law, the average magnitude and the variation range for these cases are quite different. For example, for optical thickness of 1.0, the difference between the minimum and maximum transmitted irradiance could be around 13 percent with an average value around 55 percent. For optical depth of 5.0, on the other hand, the corresponding variation is 0.8 percent with an average magnitude of 2.2 percent. Another noteworthy feature relates to the peaks of the irradiance. For small optical depth, the highest peak could be a few percent larger than the others, while as the optical depth gets larger, the variation of the peak values turn to be much smaller. This effect is due to the enhanced multiple scattering of light in the water as the optical depth gets larger. Figure 6.8 displays the reflected total irradiance associated with those cases in Figure 6.7. It can be seen that the reflected irradiance fluctuation are almost entirely determined by the ocean surface geometry, which means as optical depth get larger, the water-leaving radiance increase is almost negligible. This is expected since a relatively small albedo of 0.4 is assumed for the water. From the figure, one can see that the variation on the reflected irradiance is within two percent with an average value of 3.5 percent.

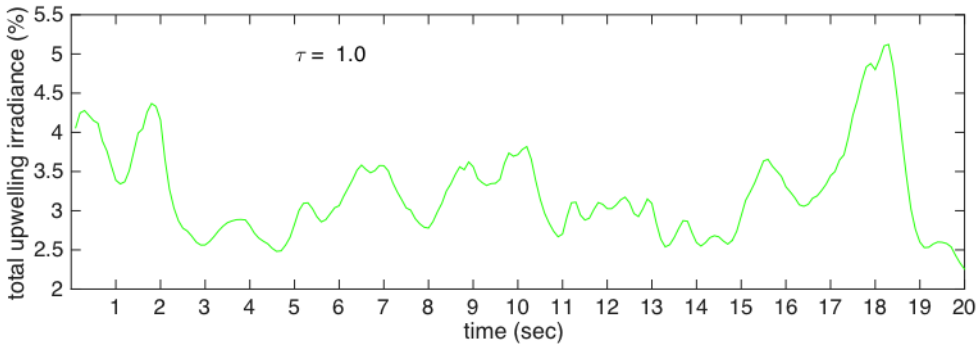

(a) For layer with optical thickness of 1.0.

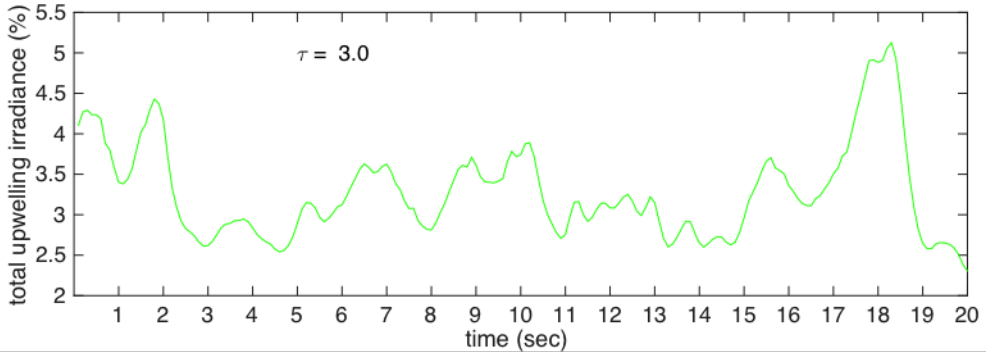

(b) For layer with optical thickness of 3.0.

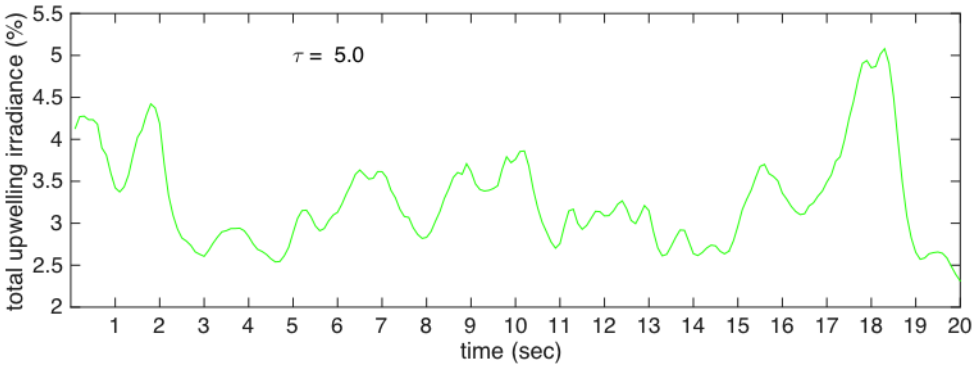

(c) For layer with optical thickness of 5.0.

Figure 6.8: The upwelling irradiance for dynamic ocean layers with different optical thicknesses. The values are computed in terms of the percentage of the incident irradiance.

A dynamic ocean surface deflects the incident light to various directions, causing the directional fluctuations on both the reflected and transmitted radiance. To demonstrate this

reflected and transmitted radiance directional fluctuation, we plot the strength of the radiance on a spherical surface. The locations on the spherical surface correspond to different directions as mentioned in last section. In this way, we can demonstrate both the directional reflected and transmitted radiance at the same time. A video of 20 seconds duration is made for each optical depth. Figure 6.9, 6.10, and 6.11 display some snapshots of the videos for different optical depths. The video shows how the reflected light beam and transmitted light beam moves with time. Since the incident light is only from one direction, both the reflected and transmitted light beams are confined to relatively small areas on the spherical surface. Compared to the transmitted beams, the reflected beams move much faster on the spherical surface, meaning the directional variation is much stronger. The red spot on the lower hemisphere for optical depth of 1.0 denotes the direction of the peak downward irradiance. The peak value for the optical depth of 1.0 could be a few orders of magnitude stronger than its surrounding directions, whereas for optical depth of 5.0, the difference between the peak and its surrounding directions is much smaller.

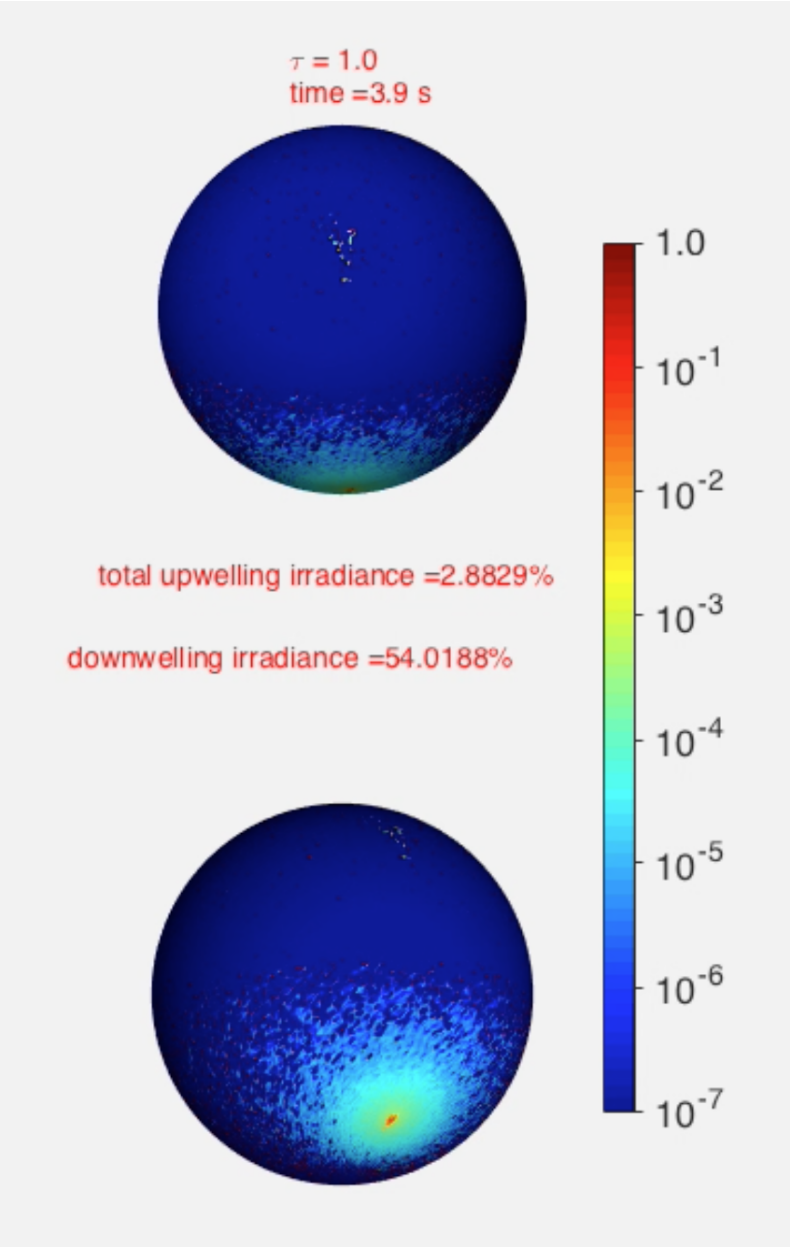

Figure 6.9: The snapshots of video showing the angular distribution of the reflected and transmitted radiance for different optical depths and times.

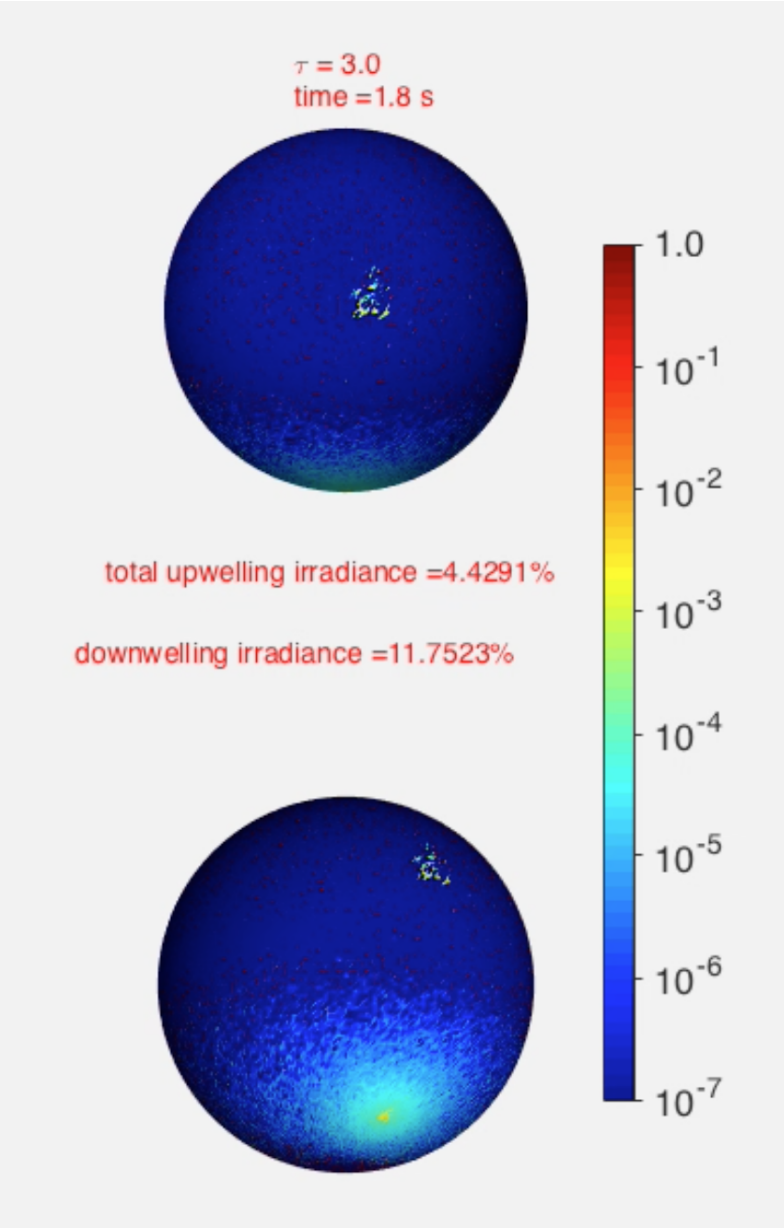

Figure 6.10: Same as Figure 6.9, except that optical thickness of the water is 3.0.

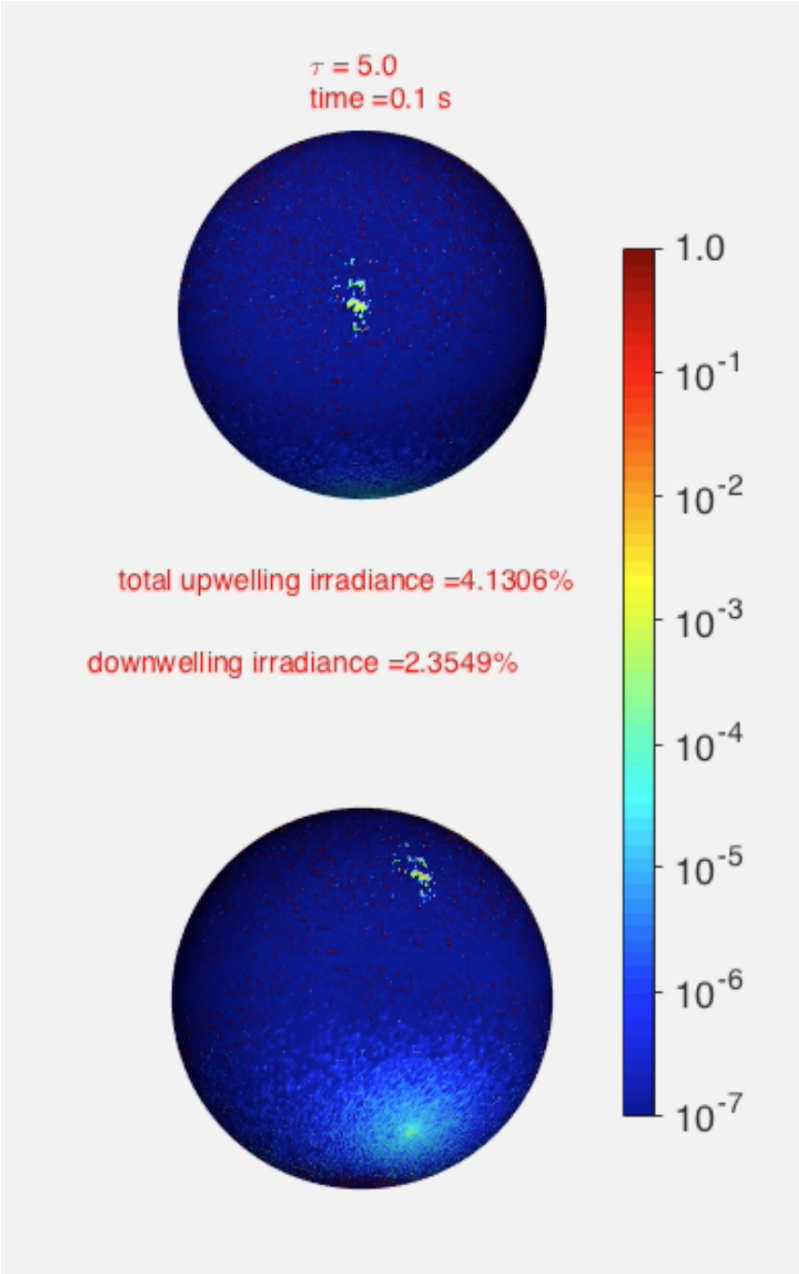

Figure 6.11: Same as Figure 6.9, except that optical thickness of the water is 5.0.

Figure 6.12 displays the fluctuation of the reflected and transmitted peak radiance in terms of the percentage of the incident radiance. Compared to the pattern of total irradiance, the variances of the fluctuation on the peak radiances are apparently larger. In other

word, the radiance could change dramatically as the ocean wave moves in a short duration.

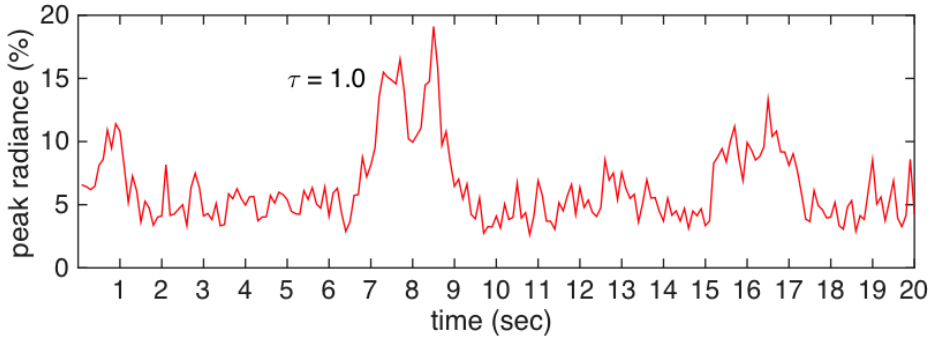

(a) the fluctuation of the down welling peak radiance

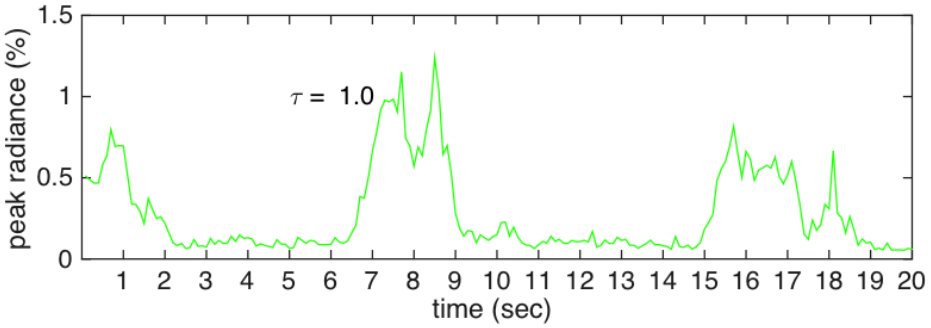

(b) the fluctuation of the upwelling peak radiance

Figure 6.12: The temporal fluctuations of the peak radiance of a dynamic ocean surface.The values are computed in terms of the percentage of the incident radiance.

Another noteworthy feature is that the peak radiance fluctuation patterns for the reflected and transmitted radiance are quite similar, in contrast to the total irradiance fluctuation patterns. This is due to the fact that the peak value of the radiance is mainly determined by the roughness degree of the ocean at a specific time.

6.2.2 Energy Distribution Variation

The dynamic ocean surface not only causes the temporal fluctuation of light field, but also may change the average energy distribution over a short period of time along

the vertical direction. Figure 6.13 shows the total transmitted and reflected energy as a function of depth under different wind conditions. It is clear that as the wind speed becomes larger, more energy could be transferred into deeper ocean. On the other hand, the reflected energy could be reduced. But as the depth becomes larger, this influence will become smaller.

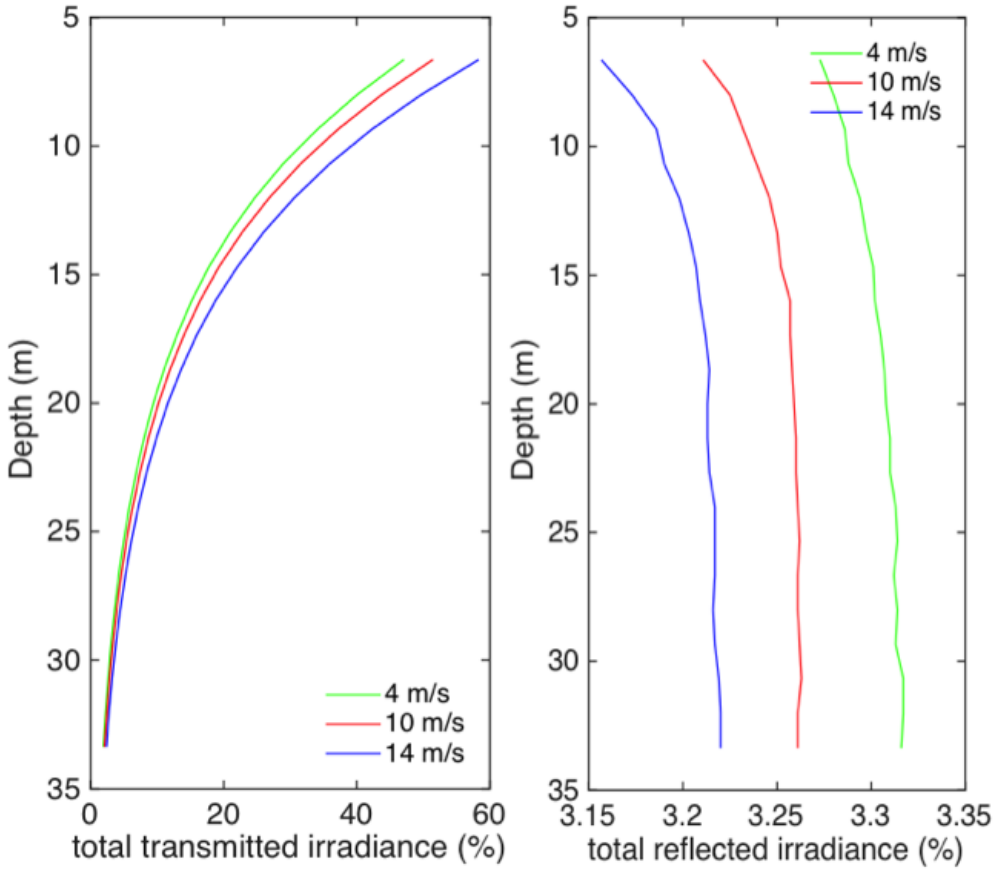

Figure 6.13: The total transmitted and reflected energy as a function of depth under different wind speed conditions. The results are the average profiles for duration of two seconds of ocean wave propagation.

6.3 Summary and Conclusions

In this study, we introduce the ocean surface model as well as the developed Monte Carlo radiative transfer model for simulating the reflected and transmitted light fields of an air-sea interface layer. The ocean surface model includes the dynamic feature, such that we are able to simulate the light field as a function of time. The Monte-Carlo model incorporates the ray tracing process of a random faceted geometry in addition to the conventional scattering sampling techniques. As an application of this model, we discuss the results relating to the dynamic aspect of ocean. Specifically, the fluctuation patterns of the total transmitted and upwelling irradiance for various optical depths are discussed. In addition, the angular fluctuation patterns of the radiance are demonstrated. Furthermore, we simulate the peak radiance fluctuation with some interesting feature noted. The variance of radiance fluctuations turns to be much larger than that of the total irradiance fluctuations. Last, we discussed the energy distribution variation under different wind speed conditions, and results suggest that the vertical distribution of the energy could be changed due to the dynamic nature of the ocean surface.

7. SUMMARY AND CONCLUSIONS

In this dissertation, numerical studies are presented on modeling the light scattering properties of some environmental components, including the aquatic particle, soot-laden mineral dust aerosols, and the air-sea interface layer. The light scattering properties of these environmental components can potentially serve as the prior knowledge for the applications of remote sensing.

For aquatic particles, an ensemble of irregular hexahedra are used to simulate their inherent optical properties. The differences between using the spherical and non-spherical models are discussed, particularly on the backscattering properties. The results suggest large differences between the spherical and non-spherical particles. With the proposed ensemble models, we are able to reproduce the in-situ measurement more accurately.

We simulate the optical properties of three possible components in the soot-laden mineral dust aerosols, i.e. the pure dust, pure soot, and dust-soot aggregates. The accuracy of the computation is assessed by comparing the results with other experimental or numerical studies. The introduced parameterization scheme computes the effective bulk properties of aerosols in term of the state of mixing. The results suggest that small uncertainty associated with the soot's mixing may induce large uncertainty on the forward and inverse modeling processes.

A Monte Carlo radiative transfer model has been developed for the purpose of simulating the reflection and transmission properties of an dynamic air-sea interface. In particular, the model incorporates the ray tracing process for the ocean surface and Monte-Carlo scattering sampling for the medium. As an application of the model, the temporal fluctuations on the reflection and transmission properties of the air-sea interface layer have been discussed.

The light scattering simulation techniques have been improved dramatically over the last fifty years. The research presented in this dissertation demonstrates the potential applications of these techniques to broad areas.

REFERENCES

[1] H. R. Gordon, O. B. Brown, and M. M. Jacobs, "Computed relationships between the inherent and apparent optical properties of a flat homogeneous ocean," *Applied Optics*, vol. 14, no. 2, pp. 417–427, 1975.

[2] D. Stramski and D. A. Kiefer, "Light scattering by microorganisms in the open ocean," *Progress in Oceanography*, vol. 28, no. 4, pp. 343–383, 1991.

[3] M. S. Twardowski, E. Boss, J. B. Macdonald, W. S. Pegau, A. H. Barnard, and J. R. V. Zaneveld, "A model for estimating bulk refractive index from the optical backscattering ratio and the implications for understanding particle composition in case i and case ii waters," *Journal of Geophysical Research: Oceans*, vol. 106, no. C7, pp. 14129–14142, 2001.

[4] E. Boss, W. S. Pegau, W. D. Gardner, J. R. V. Zaneveld, A. H. Barnard, M. S. Twardowski, G. Chang, and T. Dickey, "Spectral particulate attenuation and particle size distribution in the bottom boundary layer of a continental shelf," *Journal of Geophysical Research: Oceans*, vol. 106, no. C5, pp. 9509–9516, 2001.

[5] O. B. Brown and H. R. Gordon, "Two component mie scattering models of sargasso sea particles," *Applied Optics*, vol. 12, no. 10, pp. 2461–2465, 1973.

[6] O. B. Brown and H. R. Gordon, "Size–refractive index distribution of clear coastal water particulates from light scattering," *Applied Optics*, vol. 13, no. 12, pp. 2874–2881, 1974.

[7] J. R. V. Zaneveld, D. M. Roach, and H. Pak, "The determination of the index of refraction distribution of oceanic particulates," *Journal of Geophysical Research*, vol. 79, no. 27, pp. 4091–4095, 1974.

[8] M. I. Mishchenko, J. W. Hovenier, and L. D. Travis, *Light Scattering by Nonspherical Particles: Theory, Measurements, and Applications*. Academic press, 1999.

[9] A. L. Whitmire, W. S. Pegau, L. Karp-Boss, E. Boss, and T. J. Cowles, "Spectral backscattering properties of marine phytoplankton cultures," *Optics Express*, vol. 18, no. 14, pp. 15073–15093, 2010.

[10] H. Volten, J. De Haan, J. Hovenier, R. Schreurs, W. Vassen, A. Dekker, H. Hoogenboom, F. Charlton, and R. Wouts, "Laboratory measurements of angular distributions of light scattered by phytoplankton and silt," *Limnology and Oceanography*, vol. 43, no. 6, pp. 1180–1197, 1998.

[11] R. D. Vaillancourt, C. W. Brown, R. R. Guillard, and W. M. Balch, "Light backscattering properties of marine phytoplankton: relationships to cell size, chemical composition and taxonomy," *Journal of Plankton Research*, vol. 26, no. 2, pp. 191–212, 2004.

[12] M. Quinby-Hunt, A. Hunt, K. Lofftus, and D. Shapiro, "Polarized-light scattering studies of marine chlorella," *Limnology and Oceanography*, vol. 34, no. 8, pp. 1587–1600, 1989.

[13] J. C. Kitchen and J. R. V. Zaneveld, "A three-layered sphere model of the optical properties of phytoplankton," *Limnology and Oceanography*, vol. 37, no. 8, pp. 1680–1690, 1992.

[14] A. Quirantes and S. Bernard, "Light scattering by marine algae: two-layer spherical and nonspherical models," *Journal of Quantitative Spectroscopy and Radiative Transfer*, vol. 89, no. 1, pp. 311–321, 2004.

[15] S. Bernard, T. Probyn, and A. Quirantes, "Simulating the optical properties of phytoplankton cells using a two-layered spherical geometry.," *Biogeosciences Discus-*

sions, vol. 6, no. 1, 2009.

[16] R. Gibson, R. Atkinson, and J. Gordon, "Inherent optical properties of non-spherical marine-like particles from theory to observation," *Oceanography and Marine Biology: An Annual Review*, vol. 45, pp. 1–38, 2007.

[17] L. Bi, P. Yang, G. W. Kattawar, and R. Kahn, "Modeling optical properties of mineral aerosol particles by using nonsymmetric hexahedra," *Applied Optics*, vol. 49, no. 3, pp. 334–342, 2010.

[18] M. I. Mishchenko, L. D. Travis, and A. A. Lacis, *Scattering, Absorption, and Emission of Light by Small Particles*. Cambridge university press, 2002.

[19] L. Bi, P. Yang, G. W. Kattawar, and M. I. Mishchenko, "Efficient implementation of the invariant imbedding t-matrix method and the separation of variables method applied to large nonspherical inhomogeneous particles," *Journal of Quantitative Spectroscopy and Radiative Transfer*, vol. 116, pp. 169–183, 2013.

[20] L. Bi and P. Yang, "Accurate simulation of the optical properties of atmospheric ice crystals with the invariant imbedding t-matrix method," *Journal of Quantitative Spectroscopy and Radiative Transfer*, vol. 138, pp. 17–35, 2014.

[21] K. Yee, "Numerical solution of initial boundary value problems involving maxwell's equations in isotropic media," *IEEE Transactions On Antennas and Propagation*, vol. 14, no. 3, pp. 302–307, 1966.

[22] P. Yang and K. Liou, "Finite-difference time domain method for light scattering by small ice crystals in three-dimensional space," *JOSA A*, vol. 13, no. 10, pp. 2072–2085, 1996.

[23] E. M. Purcell and C. R. Pennypacker, "Scattering and absorption of light by nonspherical dielectric grains," *The Astrophysical Journal*, vol. 186, pp. 705–714, 1973.

[24] B. T. Draine, "The discrete-dipole approximation and its application to interstellar graphite grains," *The Astrophysical Journal*, vol. 333, pp. 848–872, 1988.

[25] B. T. Draine and P. J. Flatau, "Discrete-dipole approximation for scattering calculations," *JOSA A*, vol. 11, no. 4, pp. 1491–1499, 1994.

[26] M. A. Yurkin and A. G. Hoekstra, "The discrete dipole approximation: an overview and recent developments," *Journal of Quantitative Spectroscopy and Radiative Transfer*, vol. 106, no. 1, pp. 558–589, 2007.

[27] Q. H. Liu, "The pseudospectral time-domain (pstd) algorithm for acoustic waves in absorptive media," *IEEE Transactions on Ultrasonics, Ferroelectrics, and Frequency Control*, vol. 45, no. 4, pp. 1044–1055, 1998.

[28] Q. H. Liu, "The pstd algorithm: A time-domain method requiring only two cells per wavelength," *Microwave and Optical Technology Letters*, vol. 15, no. 3, pp. 158–165, 1997.

[29] G. Chen, P. Yang, and G. W. Kattawar, "Application of the pseudospectral time-domain method to the scattering of light by nonspherical particles," *JOSA A*, vol. 25, no. 3, pp. 785–790, 2008.

[30] L. Bi, P. Yang, G. W. Kattawar, Y. Hu, and B. A. Baum, "Scattering and absorption of light by ice particles: solution by a new physical-geometric optics hybrid method," *Journal of Quantitative Spectroscopy and Radiative Transfer*, vol. 112, no. 9, pp. 1492–1508, 2011.

[31] I. Chiapello, G. Bergametti, B. Chatenet, F. Dulac, I. Jankowiak, C. Liousse, and E. S. Soares, "Contribution of the different aerosol species to the aerosol mass load and optical depth over the northeastern tropical atlantic," *Journal of Geophysical Research: Atmospheres*, vol. 104, no. D4, pp. 4025–4035, 1999.

[32] P. Ginoux, M. Chin, I. Tegen, J. M. Prospero, B. Holben, O. Dubovik, and S.-J. Lin, "Sources and distributions of dust aerosols simulated with the gocart model," *Journal of Geophysical Research: Atmospheres*, vol. 106, no. D17, pp. 20255–20273, 2001.

[33] M. O. Andreae, R. J. Charlson, F. Bruynseels, H. Storms, R. Van Grieken, and W. Maenhaut, "Internal mixture of sea salt, silicates, and excess sulfate in marine aerosols," *Science*, vol. 232, no. 4758, pp. 1620–1623, 1986.

[34] C. S. Zender, R. Miller, and I. Tegen, "Quantifying mineral dust mass budgets: Terminology, constraints, and current estimates," *Eos, Transactions American Geophysical Union*, vol. 85, no. 48, pp. 509–512, 2004.

[35] C. Textor, M. Schulz, S. Guibert, S. Kinne, Y. Balkanski, S. Bauer, T. Berntsen, T. Berglen, O. Boucher, M. Chin, *et al.*, "Analysis and quantification of the diversities of aerosol life cycles within aerocom," *Atmospheric Chemistry and Physics*, vol. 6, no. 7, pp. 1777–1813, 2006.

[36] R. Swap, M. Garstang, S. Greco, R. Talbot, and P. Kållberg, "Saharan dust in the amazon basin," *Tellus B*, vol. 44, no. 2, pp. 133–149, 1992.

[37] M. Chin, T. Diehl, P. Ginoux, and W. Malm, "Intercontinental transport of pollution and dust aerosols: implications for regional air quality," *Atmospheric Chemistry and Physics*, vol. 7, no. 21, pp. 5501–5517, 2007.

[38] I. Uno, K. Eguchi, K. Yumimoto, T. Takemura, A. Shimizu, M. Uematsu, Z. Liu, Z. Wang, Y. Hara, and N. Sugimoto, "Asian dust transported one full circuit around the globe," *Nature Geoscience*, vol. 2, no. 8, p. 557, 2009.

[39] I. Sokolik, D. Winker, G. Bergametti, D. Gillette, G. Carmichael, Y. Kaufman, L. Gomes, L. Schuetz, and J. Penner, "Introduction to special section: Outstanding

problems in quantifying the radiative impacts of mineral dust," *Journal of Geophysical Research: Atmospheres*, vol. 106, no. D16, pp. 18015–18027, 2001.

[40] J. J. McCarthy, O. F. Canziani, N. A. Leary, D. J. Dokken, and K. S. White, "Climate change 2001: Impacts, adaptation, and vulnerability. contribution of working group ii to the third assessment report of the intergovernmental panel on climate change, 2001," *J Appl Meteorol*, vol. 44, no. 5, p. 7009716Messerli, 2001.

[41] Y. Kaufman, "Remote sensing of direct and indirect aerosol forcing," *Aerosol Forcing of Climate*, pp. 297–332, 1995.

[42] A. Clarke, Y. Shinozuka, V. Kapustin, S. Howell, B. Huebert, S. Doherty, T. Anderson, D. Covert, J. Anderson, X. Hua, *et al.*, "Size distributions and mixtures of dust and black carbon aerosol in asian outflow: Physiochemistry and optical properties," *Journal of Geophysical Research: Atmospheres*, vol. 109, no. D15, 2004.

[43] S. Takahama, S. Liu, and L. Russell, "Coatings and clusters of carboxylic acids in carbon-containing atmospheric particles from spectromicroscopy and their implications for cloud-nucleating and optical properties," *Journal of Geophysical Research: Atmospheres*, vol. 115, no. D1, 2010.

[44] O. Dubovik, A. Sinyuk, T. Lapyonok, B. N. Holben, M. Mishchenko, P. Yang, T. F. Eck, H. Volten, O. Munoz, B. Veihelmann, *et al.*, "Application of spheroid models to account for aerosol particle nonsphericity in remote sensing of desert dust," *Journal of Geophysical Research: Atmospheres*, vol. 111, no. D11, 2006.

[45] A. Glen and S. Brooks, "A new method for measuring optical scattering properties of atmospherically relevant dusts using the cloud and aerosol spectrometer with polarization (caspol)," *Atmospheric Chemistry and Physics*, vol. 13, no. 3, pp. 1345–1356, 2013.

[46] S. K. Mishra and S. Tripathi, "Modeling optical properties of mineral dust over the indian desert," *Journal of Geophysical Research: Atmospheres*, vol. 113, no. D23, 2008.

[47] S. Alfaro, S. Lafon, J. Rajot, P. Formenti, A. Gaudichet, and M. Maille, "Iron oxides and light absorption by pure desert dust: An experimental study," *Journal of Geophysical Research: Atmospheres*, vol. 109, no. D8, 2004.

[48] J. Lelieveld, H. Berresheim, S. Borrmann, P. Crutzen, F. Dentener, H. Fischer, J. Feichter, P. Flatau, J. Heland, R. Holzinger, *et al.*, "Global air pollution crossroads over the mediterranean," *Science*, vol. 298, no. 5594, pp. 794–799, 2002.

[49] R. C. Sullivan and K. A. Prather, "Investigations of the diurnal cycle and mixing state of oxalic acid in individual particles in asian aerosol outflow," *Environmental Science Technology*, vol. 41, no. 23, pp. 8062–8069, 2007.

[50] R. Subramanian, G. Kok, D. Baumgardner, A. Clarke, Y. Shinozuka, T. Campos, C. Heizer, B. Stephens, B. De Foy, P. B. Voss, *et al.*, "Black carbon over mexico: the effect of atmospheric transport on mixing state, mass absorption cross-section, and bc/co ratios.," *Atmospheric Chemistry & Physics*, vol. 10, no. 1, 2010.

[51] T. C. Bond, S. J. Doherty, D. Fahey, P. Forster, T. Berntsen, B. DeAngelo, M. Flanner, S. Ghan, B. Kärcher, D. Koch, *et al.*, "Bounding the role of black carbon in the climate system: A scientific assessment," *Journal of Geophysical Research: Atmospheres*, vol. 118, no. 11, pp. 5380–5552, 2013.

[52] M. I. Mishchenko and J. M. Dlugach, "Adhesion of mineral and soot aerosols can strongly affect their scattering and absorption properties," *Optics Letters*, vol. 37, no. 4, pp. 704–706, 2012.

[53] M. I. Mishchenko, L. Liu, and D. W. Mackowski, "T-matrix modeling of linear depolarization by morphologically complex soot and soot-containing aerosols," *Journal of Quantitative Spectroscopy and Radiative Transfer*, vol. 123, pp. 135–144, 2013.

[54] B. Scarnato, S. China, K. Nielsen, and C. Mazzoleni, "Perturbations of the optical properties of mineral dust particles by mixing with black carbon: a numerical simulation study," *Atmospheric Chemistry and Physics*, vol. 15, no. 12, pp. 6913–6928, 2015.

[55] S. Mishra, S. Tripathi, S. G. Aggarwal, and A. Arola, "Optical properties of accumulation mode, polluted mineral dust: effects of particle shape, hematite content and semi-external mixing with carbonaceous species," *Tellus B: Chemical and Physical Meteorology*, vol. 64, no. 1, p. 18536, 2012.

[56] P.-W. Zhai, Y. Hu, J. Chowdhary, C. R. Trepte, P. L. Lucker, and D. B. Josset, "A vector radiative transfer model for coupled atmosphere and ocean systems with a rough interface," *Journal of Quantitative Spectroscopy and Radiative Transfer*, vol. 111, no. 7, pp. 1025–1040, 2010.

[57] P.-W. Zhai, Y. Hu, C. R. Trepte, and P. L. Lucker, "A vector radiative transfer model for coupled atmosphere and ocean systems based on successive order of scattering method," *Optics Express*, vol. 17, no. 4, pp. 2057–2079, 2009.

[58] C. D. Mobley, *Light and Water: Radiative Transfer in Natural Waters*. Academic press, 1994.

[59] F. Fell and J. Fischer, "Numerical simulation of the light field in the atmosphere–ocean system using the matrix-operator method," *Journal of Quantitative Spectroscopy and Radiative Transfer*, vol. 69, no. 3, pp. 351–388, 2001.

[60] K. I. Gjerstad, J. J. Stamnes, B. Hamre, J. K. Lotsberg, B. Yan, and K. Stamnes, "Monte carlo and discrete-ordinate simulations of irradiances in the coupled atmosphere-ocean system," *Applied Optics*, vol. 42, no. 15, pp. 2609–2622, 2003.

[61] V. Rozanov, M. Buchwitz, K.-U. Eichmann, R. De Beek, and J. Burrows, "Sciatran-a new radiative transfer model for geophysical applications in the 240–2400 nm spectral region: The pseudo-spherical version," *Advances in Space Research*, vol. 29, no. 11, pp. 1831–1835, 2002.

[62] V. Rozanov, A. Rozanov, A. Kokhanovsky, and J. Burrows, "Radiative transfer through terrestrial atmosphere and ocean: software package sciatran," *Journal of Quantitative Spectroscopy and Radiative Transfer*, vol. 133, pp. 13–71, 2014.

[63] C. Cox and W. Munk, "Measurement of the roughness of the sea surface from photographs of the sun?s glitter," *JOSA*, vol. 44, no. 11, pp. 838–850, 1954.

[64] C. Mobley, "How well does hydrolight simulate wind-blown sea surfaces?," tech. rep., Hydrolight Technical Note 1, http://www. sequoiasci. com/products/hl-radiative. cmsx, 2002.

[65] H. R. Gordon, "Normalized water-leaving radiance: revisiting the influence of surface roughness," *Applied Optics*, vol. 44, no. 2, pp. 241–248, 2005.

[66] M. Darecki, D. Stramski, and M. Sokólski, "Measurements of high-frequency light fluctuations induced by sea surface waves with an underwater porcupine radiometer system," *Journal of Geophysical Research: Oceans*, vol. 116, no. C7, 2011.

[67] P. F. Schippnick, "Imaging of a bottom object through a wavy air-water interface," in *SPIE Proc*, vol. 925, pp. 371–382, 1988.

[68] P. Walsh and L. Legendre, "Photosynthesis of natural phytoplankton under high frequency light fluctuations simulating those induced by sea surface waves," *Lim-*

nology and Oceanography, vol. 28, no. 4, pp. 688–697, 1983.

[69] B. Queguiner and L. Legendre, "Phytoplankton photosynthetic adaptation to high frequency light fluctuations simulating those induced by sea surface waves," *Marine Biology*, vol. 90, no. 4, pp. 483–491, 1986.

[70] R. E. Walker, *Marine Light Field Statistics*, vol. 21. Wiley-Interscience, 1994.

[71] J. Ronald, V. Zaneveld, E. Boss, and P. A. Hwang, "The influence of coherent waves on the remotely sensed reflectance," *Optics Express*, vol. 9, no. 6, pp. 260–266, 2001.

[72] K. Stamnes and J. J. Stamnes, *Radiative transfer in coupled environmental systems: an introduction to forward and inverse modeling*. John Wiley & Sons, 2016.

[73] J. Chowdhary, "Multiple scattering of polarized light in atmosphere-ocean systems: Application to sensitivity analyses of aerosol polarimetry," 1999.

[74] Z. Xu and D. K. Yue, "Monte carlo radiative transfer simulation for the near-ocean-surface high-resolution downwelling irradiance statistics," *Optical Engineering*, vol. 53, no. 5, pp. 051408–051408, 2014.

[75] H. R. Gordon, "Ship perturbation of irradiance measurements at sea. 1: Monte carlo simulations," *Applied Optics*, vol. 24, no. 23, pp. 4172–4182, 1985.

[76] J. T. O. Kirk, "Monte carlo procedure for simulating the penetration of light into natural waters," *Technical Paper-Commonwealth Scientific and Industrial Research Organization*, 1981.

[77] J. Kirk, "Monte carlo study of the nature of the underwater light field in, and the relationships between optical properties of, turbid yellow waters," *Marine and Freshwater Research*, vol. 32, no. 4, pp. 517–532, 1981.

[78] Y. You, P.-W. Zhai, G. W. Kattawar, and P. Yang, "Polarized radiance fields under a dynamic ocean surface: a three-dimensional radiative transfer solution," *Applied Optics*, vol. 48, no. 16, pp. 3019–3029, 2009.

[79] J. D. Jackson, *Classical Electrodynamics*. John Wiley & Sons, 2007.

[80] G. Mie, "Articles on the optical characteristics of turbid tubes, especially colloidal metal solutions," *Ann. Phys*, vol. 25, no. 3, pp. 377–445, 1908.

[81] C. F. Bohren and D. R. Huffman, *Absorption and Scattering of Light by Small Particles*. John Wiley & Sons, 2008.

[82] B. R. Johnson, "Invariant imbedding t matrix approach to electromagnetic scattering," *Applied Optics*, vol. 27, no. 23, pp. 4861–4873, 1988.

[83] L. Bi, P. Yang, G. W. Kattawar, Y. Hu, and B. A. Baum, "Scattering and absorption of light by ice particles: solution by a new physical-geometric optics hybrid method," *Journal of Quantitative Spectroscopy and Radiative Transfer*, vol. 112, no. 9, pp. 1492–1508, 2011.

[84] C. Liu, R. L. Panetta, and P. Yang, "The effective equivalence of geometric irregularity and surface roughness in determining particle single-scattering properties," *Optics Express*, vol. 22, no. 19, pp. 23620–23627, 2014.

[85] S. G. Ackleson, W. M. Balch, and P. M. Holligan, "Response of water-leaving radiance to particulate calcite and chlorophyll a concentrations: A model for gulf of maine coccolithophore blooms," *Journal of Geophysical Research: Oceans*, vol. 99, no. C4, pp. 7483–7499, 1994.

[86] H. Bader, "The hyperbolic distribution of particle sizes," *Journal of Geophysical Research*, vol. 75, no. 15, pp. 2822–2830, 1970.

[87] D. Stramski, E. Boss, D. Bogucki, and K. J. Voss, "The role of seawater constituents in light backscattering in the ocean," *Progress in Oceanography*, vol. 61, no. 1, pp. 27–56, 2004.

[88] A. Morel and A. Bricaud, "Inherent optical properties of algal cells including picoplankton: theoretical and experimental results," *Can. Bull. Fish. Aquat. Sci*, vol. 214, pp. 521–559, 1986.

[89] D. Stramski, A. Bricaud, and A. Morel, "Modeling the inherent optical properties of the ocean based on the detailed composition of the planktonic community," *Applied Optics*, vol. 40, no. 18, pp. 2929–2945, 2001.

[90] A. Morel and Y.-H. Ahn, "Optics of heterotrophic nanoflagellates and ciliates: A tentative assessment of their scattering role in oceanic waters compared to those of bacterial and algal cells," *Journal of Marine Research*, vol. 49, no. 1, pp. 177–202, 1991.

[91] T. J. Petzold, "Volume scattering functions for selected ocean waters," tech. rep., Scripps Institution of Oceanography La Jolla Ca Visibility Lab, 1972.

[92] M. Pósfai, R. Simonics, J. Li, P. V. Hobbs, and P. R. Buseck, "Individual aerosol particles from biomass burning in southern africa: 1. compositions and size distributions of carbonaceous particles," *Journal of Geophysical Research: Atmospheres*, vol. 108, no. D13, 2003.

[93] R. Zhang, A. F. Khalizov, J. Pagels, D. Zhang, H. Xue, and P. H. McMurry, "Variability in morphology, hygroscopicity, and optical properties of soot aerosols during atmospheric processing," *Proceedings of the National Academy of Sciences*, vol. 105, no. 30, pp. 10291–10296, 2008.

[94] M. Kahnert and A. Devasthale, "Black carbon fractal morphology and short-wave radiative impact: a modelling study," *Atmospheric Chemistry and Physics*, vol. 11, no. 22, pp. 11745–11759, 2011.

[95] B. Scarnato, S. Vahidinia, D. Richard, and T. Kirchstetter, "Effects of internal mixing and aggregate morphology on optical properties of black carbon using a discrete dipole approximation model," *Atmospheric Chemistry and Physics*, vol. 13, no. 10, pp. 5089–5101, 2013.

[96] E. Mikhailov, S. Vlasenko, and A. Kiselev, "Optics and structure of carbonaceous soot aggregates," *Optics of Nanostructured Materials*, pp. 413–466, 2001.

[97] D. Mackowski and M. Mishchenko, "A multiple sphere t-matrix fortran code for use on parallel computer clusters," *Journal of Quantitative Spectroscopy and Radiative Transfer*, vol. 112, no. 13, pp. 2182–2192, 2011.

[98] C. Liu, R. L. Panetta, P. Yang, A. Macke, and A. J. Baran, "Modeling the scattering properties of mineral aerosols using concave fractal polyhedra," *Applied Optics*, vol. 52, no. 4, pp. 640–652, 2013.

[99] K. Kandler, N. Benker, U. Bundke, E. Cuevas, M. Ebert, P. Knippertz, S. Rodríguez, L. Schütz, and S. Weinbruch, "Chemical composition and complex refractive index of saharan mineral dust at izana, tenerife (spain) derived by electron microscopy," *Atmospheric Environment*, vol. 41, no. 37, pp. 8058–8074, 2007.

[100] E. A. Reid, J. S. Reid, M. M. Meier, M. R. Dunlap, S. S. Cliff, A. Broumas, K. Perry, and H. Maring, "Characterization of african dust transported to puerto rico by individual particle and size segregated bulk analysis," *Journal of Geophysical Research: Atmospheres*, vol. 108, no. D19, 2003.

[101] K. Okada, J. Heintzenberg, K. Kai, and Y. Qin, "Shape of atmospheric mineral particles collected in three chinese arid-regions," *Geophysical Research Letters*, vol. 28, no. 16, pp. 3123–3126, 2001.

[102] R. A. Zaveri, W. J. Shaw, D. J. Cziczo, B. Schmid, R. Ferrare, M. L. Alexander, R. Alvarez, W. P. Arnott, D. B. Atkinson, S. Baidar, *et al.*, "Overview of the 2010 carbonaceous aerosols and radiative effects study (cares)," *Atmospheric Chemistry and Physics*, 2012.

[103] R. Honrath, R. C. Owen, M. Val Martin, J. Reid, K. Lapina, P. Fialho, M. P. Dziobak, J. Kleissl, and D. Westphal, "Regional and hemispheric impacts of anthropogenic and biomass burning emissions on summertime co and o3 in the north atlantic lower free troposphere," *Journal of Geophysical Research: Atmospheres*, vol. 109, no. D24, 2004.

[104] K. Dzepina, C. Mazzoleni, P. Fialho, S. China, B. Zhang, R. Owen, D. Helmig, J. Hueber, S. Kumar, J. Perlinger, *et al.*, "Molecular characterization of free tropospheric aerosol collected at the pico mountain observatory: a case study with a long-range transported biomass burning plume," *Atmospheric Chemistry and Physics*, vol. 15, no. 9, pp. 5047–5068, 2015.

[105] T. Cheng, Y. Wu, X. Gu, and H. Chen, "Effects of mixing states on the multiple-scattering properties of soot aerosols," *Optics Express*, vol. 23, no. 8, pp. 10808–10821, 2015.

[106] B. R. Johnson, "Invariant imbedding t matrix approach to electromagnetic scattering," *Applied Optics*, vol. 27, no. 23, pp. 4861–4873, 1988.

[107] M. I. Mishchenko and L. D. Travis, "Satellite retrieval of aerosol properties over the ocean using polarization as well as intensity of reflected sunlight," *Journal of Geophysical Research: Atmospheres*, vol. 102, no. D14, pp. 16989–17013, 1997.

[108] H. Chang and T. Charalampopoulos, "Determination of the wavelength dependence of refractive indices of flame soot," in *Proceedings of the Royal Society of London A: Mathematical, Physical and Engineering Sciences*, vol. 430, pp. 577–591, The Royal Society, 1990.

[109] R. Wagner, T. Ajtai, K. Kandler, K. Lieke, C. Linke, T. Müller, M. Schnaiter, and M. Vragel, "Complex refractive indices of saharan dust samples at visible and near uv wavelengths: a laboratory study," *Atmospheric Chemistry and Physics*, vol. 12, no. 5, pp. 2491–2512, 2012.

[110] H. Volten, O. Munoz, E. Rol, J. d. Haan, W. Vassen, J. Hovenier, K. Muinonen, and T. Nousiainen, "Scattering matrices of mineral aerosol particles at 441.6 nm and 632.8 nm," *Journal of Geophysical Research: Atmospheres*, vol. 106, no. D15, pp. 17375–17401, 2001.

[111] H. Volten, O. Muñoz, J. Hovenier, and L. Waters, "An update of the amsterdam light scattering database," *Journal of Quantitative Spectroscopy and Radiative Transfer*, vol. 100, no. 1, pp. 437–443, 2006.

[112] X. Huang, P. Yang, G. Kattawar, and K.-N. Liou, "Effect of mineral dust aerosol aspect ratio on polarized reflectance," *Journal of Quantitative Spectroscopy and Radiative Transfer*, vol. 151, pp. 97–109, 2015.

[113] T. Elfouhaily, B. Chapron, K. Katsaros, and D. Vandemark, "A unified directional spectrum for long and short wind-driven waves," *Journal of Geophysical Research: Oceans*, vol. 102, no. C7, pp. 15781–15796, 1997.

[114] M. S. Longuet-Higgins, "Observations of the directional spectrum of sea waves using the motions of a floating buoy," *Ocean Wave Spectra*, pp. 111–136, 1961.

[115] J. Tessendorf, "Simulating ocean water. simulating nature: realistic and interactive techniques course notes," SIGGRAPH, 1999.

[116] C. D. Mobley, "Polarized reflectance and transmittance properties of windblown sea surfaces," *Applied Optics*, vol. 54, no. 15, pp. 4828–4849, 2015.

[117] P.-W. Zhai, G. W. Kattawar, and P. Yang, "Impulse response solution to the three-dimensional vector radiative transfer equation in atmosphere-ocean systems. i. monte carlo method," *Applied Optics*, vol. 47, no. 8, pp. 1037–1047, 2008.